INTERROGATING THE ORIGIN AND BEHAVIOR OF MAGNETIC RESONANCE

DIFFUSION TENSOR SCALAR PARAMETERS

IN THE MYOCARDIUM

by

Osama Mahmoud Abdullah

A dissertation submitted to the faculty of
The University of Utah
in partial fulfillment of the requirements for the degree of

Doctor of Philosophy

Department of Bioengineering

The University of Utah

May 2016

The University of Utah Graduate School

STATEMENT OF DISSERTATION APPROVAL

The dissertation of   **Osama Mahmoud Abdullah**

has been approved by the following supervisory committee members:

Edward W. Hsu	, Chair	**3/10/2016** Date Approved
Edward Victor Rebok Di Bella	, Member	**3/9/2016** Date Approved
Robert S. MacLeod	, Member	**3/9/2016** Date Approved
Frank Sachse	, Member	**3/9/2016** Date Approved
Kurt H. Albertine	, Member	**3/9/2016** Date Approved

and by   **Patrick A. Tresco**   , Chair/Dean of

the Department/College/School of   **Bioengineering**

and by David B. Kieda, Dean of The Graduate School.

ABSTRACT

Myocardial microstructure plays an important role in sustaining the orchestrated beating motion of the heart. Several microstructural components, including myocytes and auxiliary cells, extracellular space, and blood vessels provide the infrastructure for normal heart function, including excitation propagation, myocyte contraction, delivery of oxygen and nutrients, and removing byproduct wastes. Cardiac diseases cause deleterious changes to some or all of these microstructural components in the detrimental process of cardiac remodeling. Since heart failure is among the leading causes of death in the world, new and novel tools to noninvasively characterize heart microstructure are needed for monitoring and staging of cardiac disease. In this regards, diffusion magnetic resonance imaging (MRI) provides a promising framework to probe and quantify tissue microstructure without the need for exogenous contrast agent. As diffusion in 3-dimensional space is characterized by the diffusion tensor, MR diffusion tensor imaging (DTI) is being used to noninvasively measure anisotropic diffusion, and thus the magnitude and spatial orientation of microstructural organization of tissues, including the heart. However, even though *in vivo* cardiac DTI has become more clinically available, to date the origin and behavior of different microstructural components on the measured DTI signal remain to be explicitly specified. The presented studies in this work demonstrate that DTI can be used as a noninvasive and contrast-free imaging modality to characterize myocyte size and density, extracellular collagen content, and the directional

magnitude of blood flow. The identified applications are expected to provide metrics to enable physicians to detect, quantify, and stage different microstructural components during progression of cardiac disease.

To my parents, daughter and wife.

TABLE OF CONTENTS

LIST OF TABLES

LIST OF FIGURES

ACKNOWLEDGEMENTS

As any person who is fortunate enough to have wonderful parents, my parents gave their finest to raise their family during peace and war. My father's mission for me was to complete the highest academic degree, PhD, and here I am writing these words in honoring his long-time dream. My mother's love, strength, and intellect could not come at better times during the ordeals we went through in the chaotic Middle East. No words of appreciation can fulfill a fraction of a fraction of what my parents deserve.

Next I have to acknowledge my previous mentor, Dr. Shadi Othamn, who did not quit on me when the University of Illinois at Chicago (UIC) rejected my Masters application. He made the case that despite not having a prestigious GPA or GRE scores; I should be given a chance. Without that chance, I would not be able to fulfill my father's dream today.

Finally, I would like to acknowledge my PhD advisor, Dr. Edward W Hsu, not only as a boss, but as a wise man, a friend, and a mentor. During the past 9 years working with Dr. Hsu, I learned to think differently, I learned to look deeper, and search smarter. Rather than thinking about what I can do now, I learned to go after what is needed to solve a problem, even if it means going after the unchartered or the undiscovered. I enjoyed every single hour with Dr. Hsu, especially the tough moments when I had to defend my ideas. Now that my PhD training is coming to an end, I feel more confident, wiser, and somewhat more patient to life's struggles.

CHAPTER 1

INTRODUCTION

1.1 Overview

The highly coordinated functional behaviors of the heart are mediated by the distinctive organizations of its microstructural constituents. Elongated myocytes are stacked together, forming the myocardial fiber structure [1], [2], which is supported by a predominantly collagen-rich extracellular matrix (ECM) that forms secondary sheet structures [3], [4]. Myocardial torsion [13]–[17] and shear [18] during ventricular contraction have been directly attributed to the fiber and sheet structures, respectively. These structures, in turn, are often subject to alterations at both microscopic (e.g., fibrosis and fiber disarray) and macroscopic (fiber structural remodeling) scales in response to diseases like hypertrophic cardiomyopathy or changes in the cardiac environment such as elevated ventricular afterloads from hypertension [19]–[23]. Although these seminal studies have been instrumental in the current understanding of the structures and structure-function relationships of the heart, the utility of myocardial structural information in detecting, staging and monitoring under therapy of heart diseases and potentially recovery heavily depends on the ability to evaluate the structures in a subject-specific, noninvasive, and longitudinal manner, which is precluded by conventional histological examinations. Therefore, noninvasive imaging tools to characterize

myocardial structural parameters in disease and during normal development are critically needed.

Diffusion tensor imaging (DTI) [5] has emerged as the method of choice for noninvasive quantifications of myocardial structures. Diffusion, which is characterized by the Brownian motion of water molecules, in the presence of applied magnetic field gradient results in attenuation of the MRI signal that closely follows the tissue's microenvironment. The principal direction of diffusion anisotropy (i.e., the DTI primary eigenvector) has been directly correlated to the myocardial fiber orientation [24]–[26], and used to characterize the fiber structure of hearts in humans [27], [28], small [24], [29], [30], and large animals [31]. Besides alterations in the myocardial fiber orientation that are thought to be part of the compensatory responses [32], changes in the scalar DTI quantities, such as fractional anisotropy (FA), and the mean diffusivity reflecting the underlying microstructural remodeling have been observed in ischemia, post infarction, hypertrophic cardiomyopathy and heart failure [20], [30], [33]–[39]. Although the feasibility has long been demonstrated [27], [40], [41], recent advances in both gradient hardware and imaging technologies have made *in vivo* cardiac DTI more widely used [39], [41]–[47].

Cardiac DTI has been utilized to evaluate the structural remodeling associated with cardiac pathologies of both ischemic and nonischemic origins. Studies of ischemic injury have reported a reduction in the degree of diffusion anisotropy coupled with an increase of water diffusivity in the infarct zone [33], [35], [36], [48]. Additionally, DTI has been utilized in assessing nonischemic cardiac disease, such as dyssynchronous HF [49], hypertrophic cardiomyopathy [50], and dilated cardiomyopathy [51]. Besides

changes in the fiber orientation, the diseased myocardium (e.g., hypertrophy or dilated cardiomyopathy) is generally found to have decreased diffusion anisotropy [50], [51] and increased water diffusivity [51]. Although the latter changes suggest that microscopic environment for water diffusion has become less restrictive, and can be associated with myocardial fibrosis, the exact relationships between myocardial fibrosis and the DTI parameters remain yet to be determined.

Since heterogeneity of the microenvironment is the norm and not the exception in tissues, including the heart, the origin and behavior of the observed DTI changes during cardiac remodeling remain poorly understood. In this regards compartmental exchange models provide a promising framework to approximate the behavior of the diffusion MRI signal arising from a heterogeneous microscopic environment [52], [53], which is to be expected of, for example, the fibrotic myocardium. In the so-called fast-exchange situation, water spins spend much shorter time in the compartments than the temporal-length scale of their molecular dynamics. Then the MRI parameters (e.g., relaxation rate and diffusion constants) of the aggregate system behave like the fractional volume-weighted sum of the same parameters of the individual compartments. Conversely under the slow-exchange limit, the overall MRI signal is simply the proportional superposition of the signals from the individual compartments, as if the latter are completely independent. Bi-compartmental slow exchange models have been used to describe the MRI diffusion signal, including DTI, observed in the myocardium [11], [12]. Therefore, utilizing compartmental exchange models to model clinically relevant myocardial structures offers a promising framework to demonstrate the clinical utility of cardiac DTI.

Diffuse myocardial fibrosis is one of the key structural biomarkers for staging and

treatment planning of the failing heart [54]–[56]. Myocardial fibrosis has been classified into reparative or reactive [57]. In myocardial infarction (MI), fibrotic scar forms as macroscopic patches of collagen following myocyte necrosis to protect the myocardium from rupturing, and is thus called reparative fibrosis. On the other hand, collagen that develops in the remote zone to infarcts or in nonischemic cardiac disease (such as dilated cardiomyopathy or cardiac hypertrophy) manifests as microscopic collagen depositions in the interstitial space and is termed reactive or diffuse fibrosis. Diffuse fibrosis is known to increase ventricular stiffness that can lead to pump dysfunction [57], [58], and has been suggested to play a bigger role in structural remodeling in ischemic disease than the fibrotic scarring itself [59]. Tissue biopsy and histology remain the primary methods for quantifying structural remodeling in HF for staging and treatment planning of the disease [54], [56]. However, the invasive and laborious nature of the histological procedures presents a practical limitation on the number of sites and time points that can be performed. Other MRI techniques have already been used to characterize myocardial fibrosis in diseased hearts. MRI-based spin-lattice (T1) mapping has been proposed to infer myocardial collagen content via quantifying the T1 difference between pre- and post-contrast administration in the myocardium [60]. However, since many heart failure patients also suffer from kidney disease, there has been some concern on the use of gadopentate dimeglumine agents in patients with renal failure [61]. Hence, it is desirable to explore alternative contrast-free techniques to complement or replace T1-mapping for detecting and quantifying diffused fibrosis.

Translating studies of cardiac DTI to the *in vivo* domain generally encounters additional challenges due to cardiac bulk motion and capillary blood flow effects.

Promising techniques have already been developed to tackle the bulk motion problem [41], [43], [46], but microcirculation effects in cardiac DTI have not been fully characterized. The diffusion signal can be described as the statistical average of phase dispersions associated with spin displacements. For isotropic systems with Gaussian-distributed Brownian motion, the signal is an exponentially decaying function of the spin motility and the encoding diffusion sensitivity (aka, b-value). The same behavior also applies to ordered tissues, except the rate of signal decay depends also on the relative direction of the encoding gradient. In heterogeneous systems that contain spin populations with different motilities, depending on the rate of compartmental exchange, the signal is modeled as either a single exponential function with weighted decay constant or superposition of separate exponential functions [12], [53], [62]. Since blood flow in capillaries also results in translational dispersion of water molecules, theories such as the intravoxel incoherent motion (IVIM) have been proposed for characterizing microcirculation using similar diffusion-weighted imaging methodology [63], [64]. A key assumption in IVIM theory is that the capillary network consists of identical but randomly oriented straight segments, with blood changing segments rapidly while transiting through the network. In tissues, the MR signal is usually modeled as a bi-exponential function to separate the slower extravascular diffusion from the faster flow-mediated component, whose decay constant is referred to as the pseudo diffusion coefficient (D^*). Because of the assumption of random capillary orientation, it is unclear whether the classical IVIM theory can be directly applied to the myocardium, where the capillary network is both organized and oriented mostly parallel to the myofibers [12], [65]–[67]. Thus, unlike DWI and DTI in ordered tissues, the relationship between IVIM

and microcirculation-mediated diffusion signal and organized capillary networks is not completely understood.

Another clinically relevant component to better characterize myocardial remodeling is myocyte size and density. During fetal development, myocyte division (hyperplasia) is the primary mechanism for cardiac growth, whereas myocyte growth (hypertrophy) becomes the main mechanism for cardiac adaptation, for example, in response to increased systemic or pulmonary resistance [58], [68]–[71]. The preterm ovine model [72] offers unique opportunity to study cardiac adaptation in normal development (e.g., myocyte growth) and in disease (e.g., pulmonary hypertension) [73]. Although costly and laborious, the fetal ovine model is frequently used in investigations of cardiovascular and lung diseases because it recapitulates human conditions with fetuses of similar size to human as well as tolerating chronic instrumentation and experimental interventions [70], [74]. Therefore, the fetal lamb hearts at different gestational ages provide an ideal model to establish the utility of DTI to characterize myocyte size and density changes, provided that histological validation is provided.

Taken together, this dissertation aims to establish and validate the role of cardiac DTI in characterizing clinically relevant myocardial structures, including diffuse fibrosis, microcirculation flow speed and volume, and myocyte size and density.

Chapter 2 summarizes the latest advances in mapping myocardial microstructure with DTI technology. It starts with a brief history of alternative methods to characterize myocardial microstructure, followed by an overview of the main concepts of diffusion MRI, and provides a literature review of cardiac DTI and its applications in animals and humans.

Chapter 3 evaluates cardiac modeling in excised heart specimens from end-stage heart failure (HF) patients. In this chapter the effects of increased myocardial fibrosis on cardiac DTI will be established, which is an important milestone because the degree of diffuse fibrosis has been used as a marker for staging and planning of HF treatment [54], [56]. Further, the effect of diffuse fibrosis will be directly incorporated into the DTI signal equation using compartmental exchange models.

In Chapter 4, a novel theoretical framework will be introduced to describe the DTI signal equation in the presence of coherent spin motion due to organized capillary flow. The theory will be subsequently validated both numerically and experimentally, with myocardial blood flow verified via independent arterial spin labeling MRI. This chapter will provide a critically lacking theory for the effects of organized microcirculation effects, which is an important step toward the eventual use of cardiac DTI clinically.

In Chapter 5, the effect of myocyte increase in size and density on the DTI signal will be characterized in an animal model of fetal myocardial development. The chapter will complement previous chapters by describing the additional effect of increased myocyte size and density in myocardial tissue on the DTI signal.

Chapter 6 will provide an overall summary of the findings and propose specific studies to build on the cumulative knowledge learned from the different studies in this thesis.

1.2 References

[1]   D. D. Streeter, H. M. Spotnitz, D. P. Patel, J. Ross, and E. H. Sonnenblick, "Fiber orientation in the canine left ventricle during diastole and systole," *Circ. Res.*, vol. 24, no. 3, pp. 339–47, Mar. 1969.

[2] M. A. Ross, D. D. Streeter Jr, and others, "Nonuniform subendocardial fiber orientation in the normal macaque left ventricle," *Eur. J. Cardiol.*, vol. 3, no. 3, p. 229, 1975.

[3] P. M. Nielsen, I. J. Le Grice, B. H. Smaill, and P. J. Hunter, "Mathematical model of geometry and fibrous structure of the heart," *Am. J. Physiol.*, vol. 260, no. 4 Pt 2, pp. H1365–78, Apr. 1991.

[4] I. J. Legrice, P. J. Hunter, and B. H. Smaill, "Laminar structure of the heart: a mathematical model," *Am. J. Physiol.*, vol. 272, no. 5 Pt 2, pp. H2466–76, May 1997.

[5] P. J. Basser, J. Mattiello, and D. LeBihan, "MR diffusion tensor spectroscopy and imaging," *Biophys. J.*, vol. 66, no. 1, pp. 259–67, Jan. 1994.

[6] W. C. Cole, A. D. Leblanc, and S. G. Jhingran, "The origin of biexponential T2 relaxation in muscle water," *Magn. Reson. Med.*, vol. 29, no. 1, pp. 19–24, Jan. 1993.

[7] K. D. Harkins, A. N. Dula, and M. D. Does, "Effect of intercompartmental water exchange on the apparent myelin water fraction in multiexponential T2 measurements of rat spinal cord," *Magn. Reson. Med.*, vol. 67, no. 3, pp. 793–800, Mar. 2012.

[8] D. a. Yablonskiy and A. L. Sukstanskii, "Theoretical models of the diffusion weighted MR signal," *NMR Biomed.*, vol. 23, no. 7, pp. 661–681, 2010.

[9] Y. Assaf, R. Z. Freidlin, G. K. Rohde, and P. J. Basser, "New modeling and experimental framework to characterize hindered and restricted water diffusion in brain white matter," *Magn. Reson. Med.*, vol. 52, no. 5, pp. 965–78, Nov. 2004.

[10] D. C. Alexander, "A general framework for experiment design in diffusion MRI and its application in measuring direct tissue-microstructure features," *Magn. Reson. Med.*, vol. 60, no. 2, pp. 439–48, Aug. 2008.

[11] J. R. Forder, J. D. Bui, D. L. Buckley, and S. J. Blackband, "MR imaging measurement of compartmental water diffusion in perfused heart slices," *Am J Physiol Hear. Circ Physiol.*, vol. 281, pp. H1280–H1285, 2001.

[12] E. W. Hsu, D. L. Buckley, J. D. Bui, S. J. Blackband, and J. R. Forder, "Two-component diffusion tensor MRI of isolated perfused hearts," *Magn. Reson. Med.*, vol. 45, no. 6, pp. 1039–45, Jun. 2001.

[13] N. H. L. Kuijpers, E. Hermeling, P. H. M. Bovendeerd, T. Delhaas, and F. W. Prinzen, "Modeling cardiac electromechanics and mechanoelectrical coupling in

dyssynchronous and failing hearts: insight from adaptive computer models," *J. Cardiovasc. Transl. Res.*, vol. 5, no. 2, pp. 159–69, Apr. 2012.

[14] T. Arts, P. Bovendeerd, T. Delhaas, and F. Prinzen, "Modeling the relation between cardiac pump function and myofiber mechanics," *J. Biomech.*, vol. 36, no. 5, pp. 731–736, May 2003.

[15] P. H. M. Bovendeerd, T. Arts, J. M. Huyghe, D. H. van Campen, and R. S. Reneman, "Dependence of local left ventricular wall mechanics on myocardial fiber orientation: a model study," *J. Biomech.*, vol. 25, no. 10, pp. 1129–40, Oct. 1992.

[16] L. K. Waldman, D. Nosan, F. Villarreal, and J. W. Covell, "Relation between transmural deformation and local myofiber direction in canine left ventricle," *Circ. Res.*, vol. 63, no. 3, pp. 550–562, Sep. 1988.

[17] A. A. Young and B. R. Cowan, "Evaluation of left ventricular torsion by cardiovascular magnetic resonance," *J. Cardiovasc. Magn. Reson.*, vol. 14, p. 49, Jan. 2012.

[18] T. Arts, K. D. Costa, J. W. Covell, and A. D. McCulloch, "Relating myocardial laminar architecture to shear strain and muscle fiber orientation," *Am. J. Physiol. Heart Circ. Physiol.*, vol. 280, no. 5, pp. H2222–9, May 2001.

[19] P. F. Ferreira, P. J. Kilner, L.-A. McGill, S. Nielles-Vallespin, A. D. Scott, S. Y. Ho, K. P. McCarthy, M. M. Haba, T. F. Ismail, P. D. Gatehouse, R. de Silva, A. R. Lyon, S. K. Prasad, D. N. Firmin, and D. J. Pennell, "*In vivo* cardiovascular magnetic resonance diffusion tensor imaging shows evidence of abnormal myocardial laminar orientations and mobility in hypertrophic cardiomyopathy," *J. Cardiovasc. Magn. Reson.*, vol. 16, p. 87, Jan. 2014.

[20] O. M. Abdullah, S. G. Drakos, N. a. Diakos, O. Wever-Pinzon, A. G. Kfoury, J. Stehlik, C. H. Selzman, B. B. Reid, K. Brunisholz, D. R. Verma, C. Myrick, F. B. Sachse, D. Y. Li, and E. W. Hsu, "Characterization of diffuse fibrosis in the failing human heart via diffusion tensor imaging and quantitative histological validation," *NMR Biomed.*, vol. 27, no. 11, pp. 1378–86, Sep. 2014.

[21] M. A. J. Borgdorff, B. Bartelds, M. G. Dickinson, P. Steendijk, M. de Vroomen, and R. M. F. Berger, "Distinct loading conditions reveal various patterns of right ventricular adaptation," *Am. J. Physiol. Heart Circ. Physiol.*, vol. 305, no. 3, pp. H354–64, Aug. 2013.

[22] M. S. Visner, C. E. Arentzen, A. J. Crumbley, E. V Larson, M. J. O'Connor, and R. W. Anderson, "The effects of pressure-induced right ventricular hypertrophy on left ventricular diastolic properties and dynamic geometry in the conscious dog," *Circulation*, vol. 74, no. 2, pp. 410–9, Aug. 1986.

[23] S. L. Gaynor, H. S. Maniar, J. B. Bloch, P. Steendijk, and M. R. Moon, "Right atrial and ventricular adaptation to chronic right ventricular pressure overload," *Circulation*, vol. 112, no. 9 Suppl, pp. I212–8, Aug. 2005.

[24] A. Holmes, D. F. Scollan, and R. L. Winslow, "Direct histological validation of diffusion tensor MRI in formaldehyde-fixed myocardium," *Magn Reson Med*, vol. 44, no. 1, pp. 157–61, Jul. 2000.

[25] D. F. Scollan, A. Holmes, R. Winslow, and J. Forder, "Histological validation of myocardial microstructure obtained from diffusion tensor magnetic resonance imaging," *Am J Physiol Hear. Circ Physiol*, vol. 275, no. 6 Pt 2, pp. H2308–18, Dec. 1998.

[26] E. W. Hsu, A. L. Muzikant, S. A. Matulevicius, R. C. Penland, and C. S. Henriquez, "Magnetic resonance myocardial fiber-orientation mapping with direct histological correlation," *Am J Physiol Hear. Circ Physiol*, vol. 274, no. 5 Pt 2, pp. H1627–34, May 1998.

[27] T. G. Reese, R. M. Weisskoff, R. N. Smith, B. R. Rosen, R. E. Dinsmore, and V. J. Wedeen, "Imaging myocardial fiber architecture *in vivo* with magnetic resonance," *Magn Reson Med*, vol. 34, no. 6, pp. 786–91, Dec. 1995.

[28] D. Rohmer, A. Sitek, and G. T. Gullberg, "Reconstruction and visualization of fiber and laminar structure in the normal human heart from *ex vivo* diffusion tensor magnetic resonance imaging (DTMRI) data," *Invest. Radiol.*, vol. 42, no. 11, pp. 777–89, Nov. 2007.

[29] Y. Jiang, K. Pandya, O. Smithies, and E. W. Hsu, "Three-dimensional diffusion tensor microscopy of fixed mouse hearts," *Magn Reson Med*, vol. 52, no. 3, pp. 453–60, Sep. 2004.

[30] J. Chen, S.-K. Song, W. Liu, M. McLean, J. S. Allen, J. Tan, S. a Wickline, and X. Yu, "Remodeling of cardiac fiber structure after infarction in rats quantified with diffusion tensor MRI," *Am J Physiol Hear. Circ Physiol*, vol. 285, no. 3, pp. H946–54, Sep. 2003.

[31] L. Zhang, J. Allen, L. Hu, S. D. Caruthers, S. a Wickline, and J. Chen, "Cardiomyocyte architectural plasticity in fetal, neonatal, and adult pig hearts delineated with diffusion tensor MRI," *Am. J. Physiol. Heart Circ. Physiol.*, vol. 304, no. 2, pp. H246–52, Jan. 2013.

[32] C. M. Ripplinger, W. Li, J. Hadley, J. Chen, F. Rothenberg, R. Lombardi, S. A. Wickline, A. J. Marian, and I. R. Efimov, "Enhanced transmural fiber rotation and connexin 43 heterogeneity are associated with an increased upper limit of vulnerability in a transgenic rabbit model of human hypertrophic

cardiomyopathy," *Circ. Res.*, vol. 101, no. 10, pp. 1049–57, Nov. 2007.

[33]   J. Chen, S.-K. Song, W. Liu, M. McLean, J. S. Allen, J. Tan, S. a Wickline, and X. Yu, "Remodeling of cardiac fiber structure after infarction in rats quantified with diffusion tensor MRI," *Am. J. Physiol. Heart Circ. Physiol.*, vol. 285, no. 3, pp. H946–54, Sep. 2003.

[34]   M.-T. Wu, W.-Y. I. Tseng, M.-Y. M. Su, C.-P. Liu, K.-R. Chiou, V. J. Wedeen, T. G. Reese, and C.-F. Yang, "Diffusion tensor magnetic resonance imaging mapping the fiber architecture remodeling in human myocardium after infarction: correlation with viability and wall motion," *Circulation*, vol. 114, no. 10, pp. 1036–45, Sep. 2006.

[35]   M.-T. Wu, M.-Y. M. Su, Y.-L. Huang, K.-R. Chiou, P. Yang, H.-B. Pan, T. G. Reese, V. J. Wedeen, and W.-Y. I. Tseng, "Sequential changes of myocardial microstructure in patients postmyocardial infarction by diffusion-tensor cardiac MR: correlation with left ventricular structure and function," *Circ Cardiovasc Imaging*, vol. 2, no. 1, pp. 32–40, Jan. 2009.

[36]   E. X. Wu, Y. Wu, J. M. Nicholls, J. Wang, S. Liao, S. Zhu, C.-P. Lau, and H.-F. Tse, "MR diffusion tensor imaging study of postinfarct myocardium structural remodeling in a porcine model," *Magn Reson Med*, vol. 58, no. 4, pp. 687–95, Oct. 2007.

[37]   S. Winklhofer, C. T. Stoeck, N. Berger, M. Thali, R. Manka, S. Kozerke, H. Alkadhi, and P. Stolzmann, "Post-mortem cardiac diffusion tensor imaging: detection of myocardial infarction and remodeling of myofiber architecture," *Eur. Radiol.*, vol. 24, no. 11, pp. 2810–2818, 2014.

[38]   G. L. Kung, O. M. Ajijola, R. Tung, M. Vaseghi, J. K. Gahm, W. Zhou, A. Mahajan, A. Garfinkel, K. Shivkumar, and D. B. Ennis, "Microstructural Remodeling in the Porcine Infarct Border Zone Measured by Diffusion Tensor and Late Gadolinium Enhancement MRI," *Circulation*, vol. 126, no. 21 Supplement, p. A14246, 2012.

[39]   C. T. Stoeck, A. Kalinowska, C. von Deuster, J. Harmer, R. W. Chan, M. Niemann, R. Manka, D. Atkinson, D. E. Sosnovik, C. Mekkaoui, and S. Kozerke, "Dual-phase cardiac diffusion tensor imaging with strain correction," *PLoS One*, vol. 9, no. 9, p. e107159, Jan. 2014.

[40]   W. I. Tseng, T. G. Reese, R. M. Weisskoff, and V. J. Wedeen, "Cardiac Diffusion Tensor MRI *In vivo* Without Strain Correction," *Magn. Reson. Med.*, vol. 42, pp. 393–403, 1999.

[41]   J. Dou, T. G. Reese, W.-Y. I. Tseng, and V. J. Wedeen, "Cardiac diffusion MRI without motion effects," *Magn Reson Med*, vol. 48, no. 1, pp. 105–14, Jul. 2002.

[42] W. I. Tseng, T. G. Reese, R. M. Weisskoff, and V. J. Wedeen, "Cardiac diffusion tensor MRI *in vivo* without strain correction," *Magn Reson Med*, vol. 403, no. May, pp. 393–403, 1999.

[43] U. Gamper, P. Boesiger, and S. Kozerke, "Diffusion imaging of the *in vivo* heart using spin echoes-considerations on bulk motion sensitivity," *Magn Reson Med*, vol. 57, no. 2, pp. 331–7, Feb. 2007.

[44] S. Nielles-Vallespin, C. Mekkaoui, P. Gatehouse, T. G. Reese, J. Keegan, P. F. Ferreira, S. Collins, P. Speier, T. Feiweier, R. de Silva, M. P. Jackowski, D. J. Pennell, D. E. Sosnovik, and D. Firmin, "*In vivo* diffusion tensor MRI of the human heart: Reproducibility of breath-hold and navigator-based approaches," *Magn Reson Med*, vol. 70, no. 2, pp. 454–465, Sep. 2012.

[45] L.-A. McGill, T. F. Ismail, S. Nielles-Vallespin, P. Ferreira, A. D. Scott, M. Roughton, P. J. Kilner, S. Y. Ho, K. P. McCarthy, P. D. Gatehouse, R. de Silva, P. Speier, T. Feiweier, C. Mekkaoui, D. E. Sosnovik, S. K. Prasad, D. N. Firmin, and D. J. Pennell, "Reproducibility of *in vivo* diffusion tensor cardiovascular magnetic resonance in hypertrophic cardiomyopathy," *J. Cardiovasc. Magn. Reson.*, vol. 14, no. 1, p. 86, Dec. 2012.

[46] C. Welsh, E. DiBella, and E. Hsu, "Higher-Order Motion-Compensation for *In vivo* Cardiac Diffusion Tensor Imaging in Rats," *IEEE Trans. Med. Imaging*, vol. 34, no. 9, pp. 1843–53, Mar. 2015.

[47] O. Bernus, A. Radjenovic, M. L. Trew, I. J. Legrice, G. B. Sands, D. R. Magee, B. H. Smaill, and S. H. Gilbert, "Comparison of diffusion tensor imaging by cardiovascular magnetic resonance and gadolinium enhanced 3D image intensity approaches to investigation of structural anisotropy in explanted rat hearts," *JCMR*, vol. 17, no. 31, pp. 1–27, 2015.

[48] M. Wu, W.-Y. I. Tseng, M. M. Su, C. Liu, K.-R. Chiou, V. J. Wedeen, T. G. Reese, and C.-F. Yang, "Diffusion tensor magnetic resonance imaging mapping the fiber architecture remodeling in human myocardium after infarction: correlation with viability and wall motion," *Circulation*, vol. 114, no. 10, pp. 1036–45, Sep. 2006.

[49] P. A. Helm, L. Younes, M. F. Beg, D. B. Ennis, C. Leclercq, O. P. Faris, E. McVeigh, D. Kass, M. I. Miller, and R. L. Winslow, "Evidence of structural remodeling in the dyssynchronous failing heart," *Circ. Res.*, vol. 98, no. 1, pp. 125–32, Jan. 2006.

[50] W.-Y. I. Tseng, J. Dou, T. G. Reese, and V. J. Wedeen, "Imaging myocardial fiber disarray and intramural strain hypokinesis in hypertrophic cardiomyopathy with MRI," *J. Magn. Reson. Imaging*, vol. 23, no. 1, pp. 1–8, Jan. 2006.

[51] W. Li, M. Lu, S. Banerjee, J. Zhong, A. Ye, J. Molter, and X. Yu, "*Ex vivo* diffusion tensor MRI reflects microscopic structural remodeling associated with aging and disease progression in normal and cardiomyopathic Syrian hamsters," *NMR Biomed.*, vol. 22, no. 8, pp. 819–25, Oct. 2009.

[52] H. M. McConnell, "Reaction Rates by Nuclear Magnetic Resonance," *J. Chem. Phys.*, vol. 28, no. 3, p. 430, 1958.

[53] J. Kärger, "NMR self-diffusion studies in heterogeneous systems," *Adv. Colloid Interface Sci.*, vol. 23, no. 0, pp. 129–148, Aug. 1985.

[54] J. Diez, "Losartan-Dependent Regression of Myocardial Fibrosis Is Associated With Reduction of Left Ventricular Chamber Stiffness in Hypertensive Patients," *Circulation*, vol. 105, no. 21, pp. 2512–2517, Apr. 2002.

[55] S. G. Drakos, A. G. Kfoury, E. H. Hammond, B. B. Reid, M. P. Revelo, B. Y. Rasmusson, K. J. Whitehead, M. E. Salama, C. H. Selzman, J. Stehlik, S. E. Clayson, M. R. Bristow, D. G. Renlund, and D. Y. Li, "Impact of mechanical unloading on microvasculature and associated central remodeling features of the failing human heart," *J. Am. Coll. Cardiol.*, vol. 56, no. 5, pp. 382–91, Jul. 2010.

[56] S. G. Drakos, A. G. Kfoury, J. Stehlik, C. H. Selzman, B. B. Reid, J. V Terrovitis, J. N. Nanas, and D. Y. Li, "Bridge to recovery: understanding the disconnect between clinical and biological outcomes," *Circulation*, vol. 126, no. 2, pp. 230–41, Jul. 2012.

[57] C. Jellis, J. Martin, J. Narula, and T. H. Marwick, "Assessment of nonischemic myocardial fibrosis," *J. Am. Coll. Cardiol.*, vol. 56, no. 2, pp. 89–97, Jul. 2010.

[58] K. T. Weber and C. G. Brilla, "Pathological hypertrophy and cardiac interstitium. Fibrosis and renin- angiotensin-aldosterone system," *Circulation*, vol. 83, no. 6, pp. 1849–1865, Jun. 1991.

[59] C. a. Beltrami, N. Finato, M. Rocco, G. a. Feruglio, C. Puricelli, E. Cigola, F. Quaini, E. H. Sonnenblick, G. Olivetti, and P. Anversa, "Structural basis of end-stage failure in ischemic cardiomyopathy in humans," *Circulation*, vol. 89, no. 1, pp. 151–163, Jan. 1994.

[60] D. Messroghli, S. Nordmeyer, T. Dietrich, O. Dirsch, E. Kaschina, K. Savvatis, D. O H-Ici, C. Klein, F. Berger, and T. Kuehne, "Assessment of Diffuse Myocardial Fibrosis in Rats Using Small Animal Look-Locker Inversion Recovery (SALLI) T1 Mapping," *Circ Cardiovasc Imaging*, vol. 4, no. 6, pp. 636–40, Sep. 2011.

[61] P. Marckmann, L. Skov, K. Rossen, A. Dupont, M. B. Damholt, J. G. Heaf, and H. S. Thomsen, "Nephrogenic systemic fibrosis: suspected causative role of

gadodiamide used for contrast-enhanced magnetic resonance imaging," *J. Am. Soc. Nephrol.*, vol. 17, no. 9, pp. 2359–62, Sep. 2006.

[62] T. Niendorf, R. M. Dijkhuizen, D. G. Norris, M. van Lookeren Campagne, and K. Nicolay, "Biexponential diffusion attenuation in various states of brain tissue: implications for diffusion-weighted imaging," *Magn. Reson. Med.*, vol. 36, no. 6, pp. 847–57, Dec. 1996.

[63] D. Le Bihan, E. Breton, D. Lallemand, P. Grenier, E. Cabani, and L. Jeantet, "MR imaging of intravoxel incoherent motions: application to diffusion and perfusion in neurologic disorders," *Radiology*, vol. 161, pp. 401–407, 1986.

[64] D. Le Bihan, E. Breton, D. Lallemand, M.-L. Aubin, J. Vignaud, and M. Laval-Jeantet, "Separation of diffusion and perfusion in intra voxel incoherent motion MR imaging," *Radiology*, vol. 168, no. 2, pp. 497–505, 1988.

[65] D. Poole and O. Mathieu-Costello, "Analysis of capillary and subendocardium geometry in rat subepicardium," *Am J Physiol Hear. Circ Physiol*, vol. 259, pp. 204–210, 1990.

[66] A. Vignaud, I. Rodriguez, D. B. Ennis, R. DeSilva, P. Kellman, J. Taylor, E. Bennett, and H. Wen, "Detection of myocardial capillary orientation with intravascular iron-oxide nanoparticles in spin-echo MRI," *Magn Reson Med*, vol. 55, no. 4, pp. 725–30, Apr. 2006.

[67] N. Kaneko, R. Matsuda, M. Toda, and K. Shimamoto, "Three-dimensional reconstruction of the human capillary network and the intramyocardial micronecrosis," *Am. J. Physiol. Heart Circ. Physiol.*, vol. 300, no. 3, pp. H754–61, Mar. 2011.

[68] D. Sedmera and R. P. Thompson, "Myocyte proliferation in the developing heart," *Dev. Dyn.*, vol. 240, no. 6, pp. 1322–34, Jun. 2011.

[69] D. Wulfsohn, J. R. Nyengaard, and Y. Tang, "Postnatal growth of cardiomyocytes in the left ventricle of the rat," *Anat. Rec. A. Discov. Mol. Cell. Evol. Biol.*, vol. 277, no. 1, pp. 236–47, Mar. 2004.

[70] S. S. Jonker, L. Zhang, S. Louey, G. D. Giraud, K. L. Thornburg, and J. J. Faber, "Myocyte enlargement, differentiation, and proliferation kinetics in the fetal sheep heart," *J. Appl. Physiol.*, vol. 102, no. 3, pp. 1130–42, Mar. 2007.

[71] J. H. Burrell, A. M. Boyn, V. Kumarasamy, A. Hsieh, S. I. Head, and E. R. Lumbers, "Growth and maturation of cardiac myocytes in fetal sheep in the second half of gestation," *Anat. Rec. A. Discov. Mol. Cell. Evol. Biol.*, vol. 274, no. 2, pp. 952–61, Oct. 2003.

[72]   K. Albertine, G. Jones, B. C. Starcher, J. F. Bohnsack, P. L. Davis, S.-C. Cho, D. P. Carlton, and R. D. Bland, "Chronic Lung Injury in Preterm Lambs," *Am. J. Respir. Crit. Care Med.*, vol. 159, no. 3, pp. 945–958, Mar. 1999.

[73]   K. H. Albertine, "Utility of Large-Animal Models of BPD: Chronically Ventilated Preterm Lambs," *Am. J. Physiol. - Lung Cell. Mol. Physiol.*, vol. 308, no. 10, pp. L983–L1001, May 2015.

[74]   K. H. Albertine, "Progress in understanding the pathogenesis of BPD using the baboon and sheep models," *Semin. Perinatol.*, vol. 37, no. 2, pp. 60–68, 2013.

CHAPTER 2

BACKGROUND[1]

2.1 Introduction

The intricate organization of the cardiac microstructure is a key determinant in the remarkably orchestrated atrial and ventricular activities. For example, each cardiac myocyte conducts an electrical impulse, contracts at the appropriate moment, at the right speed, and to the necessary extent [1]. The arrangement of the ventricular myocytes is involved in coordinating systolic contraction, in such ways that the efficiencies of blood ejection and fiber strain distribution are maximized [2]. Because electrical impulses propagate faster parallel to the main axis of cardiomyocytes than perpendicular to them [3], mapping myofiber orientation is an essential element for understanding the structural-functional relationship not only in the normal heart, but also in disease conditions.

Over time, several conceptual and theoretical models have been proposed for different aspects of the heart incorporating progressively sophisticated interpretations of fiber structures made available by advancing technologies [4] (and references therein). Examples in cardiac biomechanics included constitutive modeling of tissue as an elastic

material [5] and holistic understanding of the heart as a pump [1,6,7]. Experimental observations, like mechanical testing of myocardial tissue have shown that mechanical properties are dependent of tissue microstructure, in particular, fiber orientation, lamination (i.e., sheet-like formation of fibers) and the associated arrangement of the extracellular matrix. To reach physiologically relevant results from the application of these models, both, information on tissue geometry and anisotropic tissue properties are necessary [8]. Similar requirements are related to modeling of cardiac tissue electrophysiology [9], including simulation of electrical propagation. It is well established that electrical conductivities of cardiac tissues are anisotropic [3,10] and that those are determined by tissue microstructure, in particular, the local orientation [11] and apparent laminar structure of cardiac fibers [12]. In general, anisotropic description of tissue properties is a crucial component for electro-mechanical modeling of the heart [13]. Electro-mechanical applications require the integrative modeling of electrical activation, force development, and mechanical deformation based on anisotropic tissue properties. Likewise, anisotropic cardiac tissue properties have been used to produce comprehensive models seeking to provide explanations for the basic mechanisms for ventricular contraction, expansion, and torsion [14], or to explain the nature of myocardial fiber arrangement [15,16].

By quantifying the effects on the translational motility of water molecules exerted by the microscopic environment, magnetic resonance diffusion tensor imaging (MR-DTI, or DTI for short) [17] has emerged as a unique, noninvasive and nondestructive alternative to histology for characterizing myocardial tissue microstructure. DTI yields information on the diffusion anisotropy, in terms of both its direction and magnitude,

which can be used to elucidate the nature of the organization, geometry and content of the tissue. In this chapter, we will provide the basics of DTI theory, and summarize the latest progress that has been reported in relating the radiological findings provided by DTI to the known structural changes in cardiac disease, such ischemic or non-ischemic heart failure.

2.2 Earlier Observations of Cardiac Fiber Structure

Structural observations have been associated with fundamental changes in our understanding of the heart as an organ from the early days of the study of anatomy and physiology. An early example came about in 1664, when Niels Stensen published comparative observations between dissections of cardiac and skeletal muscle tissues, both which resembled each other by their fibrous appearance, thus allowing the identification of the heart as a muscle [18]. As more detailed observations became documented, the fundamental tool used to identify transmural variations of myocardial tissue orientation i.e., gross dissection of excised hearts (Lower et al. [19]), became insufficient for microstructural analysis and was aided by microscopes [20,21]. Ever since, analysis of cardiac microstructure in terms of fiber organization is often linked to the available technology.

Histological sections provided quantifiable investigations that allowed modeling of the heart, so that fiber orientation could be modeled and predicted by a mathematical formula, and to explain quantifiable differences between man and other species [11,22–24]. Specifically, Streeter and others observed that the sub-epicardial layer contains myofibers pointing "downward" toward the apex. The sub-endocardial layer contains myofibers pointing "upwards" toward the base of the heart. And the mid-wall fibers run

circumferentially parallel to the heart equator. This unique fiber orientation patterns provided the basis to coin the term "double helical fiber structure" of the heart [22]. The sub-endocardial layer was assigned a positive helix angle, which is referred to as the right handed fibers (RHF). The sub-epicardial layer was assigned a negative helix angle, and referred to as the left handed fibers (LHF). And the mid-wall layer was referred to as the circumferential fibers (CF), because the fibers in this layer mostly run parallel to the cardiac short axis.

Cardiac modeling and the development of structure-function theories continues to be an active area of research today [4], and the adoption of a comprehensive heart model is still controversial [1,6,7,16]. The introduction of digital image processing permitted more comprehensive analysis of histology, which sometimes included the use of volumetric statistics [25–28]. Likewise, more sophisticated optical methods like electron microscopy were later used to observe intermediate structures like myocardial sheets [12], and more recently, subcellular organization with the use of confocal microscopy [29].

The advent of radiological imaging has allowed noninvasive and nondestructive quantification of the myocardial fiber structure, which is highly desirable for preserving valuable samples or for evaluating the tissue *in vivo*. Specific techniques include X-ray diffraction [30,31], contrast-enhanced computer tomography [32] and MRI. The latter, stands alone in terms of soft tissue sensitivity and safety considerations, and can provide fiber orientation information via either susceptibility mapping [33] or diffusion tensor imaging (DTI) [34–38]. Recent technological advances like *in vivo* DTI [39–42] hold the potential to not only improve the general understanding of cardiac structure and function,

but also to provide subject-specific modeling of normal and diseased hearts.

2.3 Basics of Diffusion MRI

Diffusion is the random displacement of water molecules due to their thermal energy, also referred to as Brownian motion. It is important to distinguish diffusion from other transport mechanisms such as coherent blood flow in vessels. In a statistical sense, the average displacement along a given axis in space, $\langle r \rangle$, of diffusing water molecules is related to the diffusion coefficient, D (in mm²/s), via the Einstein's equation:

$$\langle r \rangle = \sqrt{2D\Delta} \qquad (2.1)$$

where Δ is the diffusion time. The diffusion coefficient D is typically slower in biological tissues compared to free water due to the obstructions imposed by tissue microstructure (e.g., cell membranes, fibers, etc.). The effect of diffusion on the magnetic resonance signal has been observed and quantified well before the invention of the MRI scanner [43,44]. Stejskal and Tanner proposed the pulsed-field-gradient (PFG) preparation to measure diffusion [45]. In the PFG preparation shown in Fig. 2.1, suppose a unit MRI signal (called "spin") at an initial position r_1 experiences a short diffusion-weighting gradient pulse, and the same spin randomly moves to location r_2 at some duration Δ (referred to as diffusion time) later when it experiences a second gradient pulse of equal amplitude but opposite polarity to the first. The net phase ϕ_{net} imparted on the spin will be proportional to its relative displacement $(r_2 - r_1)$ given by:

$$\phi_{net} = -\gamma \, G \cdot (r_2 - r_1) \, \delta \qquad (2.2)$$

where γ is the gyromagnetic ratio for the spin (hydrogen for most DTI applications), G and δ are the amplitude and widths of the diffusion encoding gradient pulses,
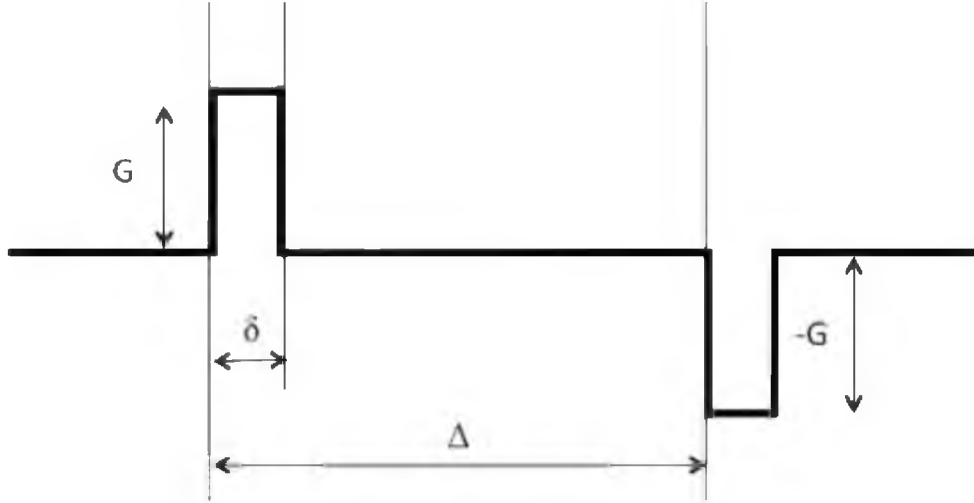
Figure 2.1. Pulsed field gradient preparation as proposed by Stejskal and Tanner [45].

respectively.

Note that the direction of G dictates the axis in which diffusion motion is measured – for example, G_x will encode water displacements in the x direction only. The Brownian translational motion of spins due to diffusion is a random process that is subject to the conditional probability density function P specified by a normal distribution with a standard deviation indicated by Eq. (2.1). The detected MRI signal after PFG preparation can be obtained by calculating the expected value of the phase dispersion for an ensemble of spins over the probability density function according to:

$$I = I_0 \int exp(i\phi_{net})P(r_2|r_1)d\phi \tag{2.3}$$

where I_0 is the diffusion-independent image intensity. The solution of the above equation for isotropic case can be expressed as [45]:

$$I = exp\left(-\gamma^2 G^2 \delta^2 \left(\Delta - \frac{\delta}{3}\right)D\right) \tag{2.4}$$

Equation (2.4) is often rewritten as

$$I = I_0 \exp(-bD) \tag{5}$$

with $b = \gamma^2 G^2 \delta^2 \left(\Delta - \frac{\delta}{3} \right)$.

Equation (2.5) conveniently separates the exponent into an intrinsic tissue property term, D, and a single parameter, the so-called diffusion-weighting b factor (typically expressed in units of s/mm^2), that combines all the MRI prescription variables. Equation (2.5) states that the effect of diffusion manifests as attenuation of the image intensity, which behaves inverse-exponentially with respect to both the diffusivity and the applied diffusion encoding gradient parameters.

2.4 MRI of Anisotropic Diffusion

Diffusion in an anisotropic medium will manifest in directionally dependent Brownian motion. Axons, ligaments, and muscle fibers are all example of anisotropic tissues, which impose a preferential direction for diffusing water molecules, where, one would intuitively expect that water diffusion will be more free and faster along the direction of the fibers but is more hindered and slower across the fibers. The orientation-dependent behavior gives rise to the anisotropic diffusion property probed in DTI. In a PFG preparation, when the diffusion encoding gradient is applied parallel to the fibers, the image intensity I in Eq. (2.5) will contain higher diffusion contribution than in the case when the encoding gradient is applied perpendicular to the fibers. Higher diffusion contribution in certain direction translates to higher attenuation in signal intensity. Figure 2.2 illustrates the anisotropic diffusion behavior in a perfused guinea pig heart. Figure 2.2a is an anatomical image without diffusion weighting, while Fig. 2.2b and 2.2c are diffusion-weighted images showing different contrasts due to the different diffusion
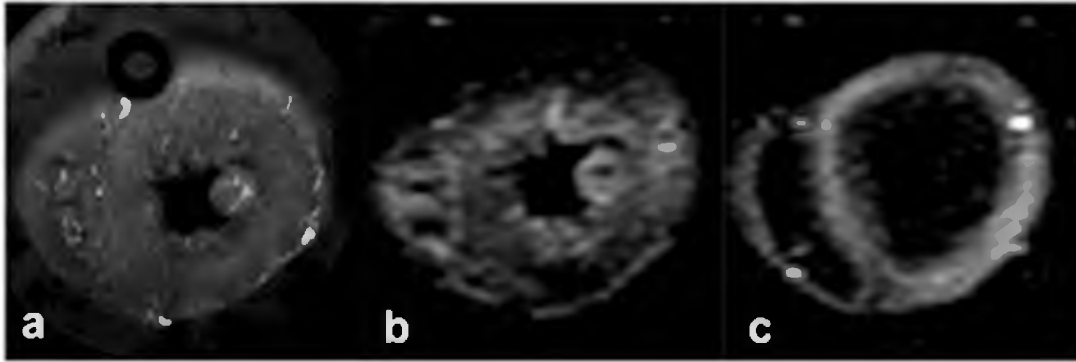
Figure 2.2. Anisotropic diffusion contrast in a perfused guinea pig heart. (a) anatomical gradient-echo image without diffusion weighting. Diffusion-weighted image (b = 500 s/mm^2) with diffusion encoding gradient applied in left-right direction (b), and in-out of page (c).

encoding direction in each case.

Anisotropic diffusion in 3D space cannot be fully characterized by a single diffusion coefficient. Instead, a tensor, appropriately called diffusion tensor, is required [17]. The MRI signal of spins diffusing in an anisotropic medium can be explained by considering the special case where the principal axes of diffusion of certain anisotropic tissue have diffusivities D_1, D_2, and D_3 along the three orthogonal principal directions (in descending order), and that diffusion is encoded along the same direction as the principal diffusivities via the diffusion encoding gradients $G(t)$. If the encoding gradients have identical timings and only differ in their directions, then $G(t)$ can be written as:

$$G(t) = \begin{bmatrix} G_1(t) \\ G_2(t) \\ G_3(t) \end{bmatrix} = u \cdot \|G(t)\| = \begin{bmatrix} u_1 \\ u_2 \\ u_3 \end{bmatrix} \cdot \|G(t)\| \qquad (2.7)$$

where u is a unit vector defining the direction of the encoding gradients (which coincides with principal diffusion axis). Following the notation of Eq. (2.4), the signal intensity satisfies

$$I = I_0 \exp\left(-b\boldsymbol{u}^T \cdot \begin{bmatrix} D_1 & 0 & 0 \\ 0 & D_2 & 0 \\ 0 & 0 & D_3 \end{bmatrix} \cdot \boldsymbol{u}\right) = I_0 \exp(-b\boldsymbol{u}^T \cdot D_\Lambda \cdot \boldsymbol{u}) \tag{2.7}$$

where the effective diffusivity can be defined as: $D_{eff} = \boldsymbol{u}^T \cdot D_\Lambda \cdot \boldsymbol{u}$.

Now let us generalize the special case introduced in Eq. (2.6) and (2.7) when the diffusion encoding gradients direction $\boldsymbol{g}$ does not coincide with the principal diffusion axis, the former can be translated to the principal diffusion axis via a rotation matrix $\boldsymbol{R}$, such that: $\boldsymbol{u} = \boldsymbol{Rg}$. Then, Eq. (2.7) becomes:

$$I = I_0 \exp(-b\, \boldsymbol{g}^T \boldsymbol{R}^T \cdot D_\Lambda \cdot \boldsymbol{R}\, \boldsymbol{g}) = I_0 \exp(-b\, \boldsymbol{g}^T \cdot \boldsymbol{D} \cdot \boldsymbol{g}) \tag{2.8}$$

where $\boldsymbol{D} = \boldsymbol{R}^T \cdot D_\Lambda \cdot \boldsymbol{R}$ corresponds to the diffusion tensor. The diffusion tensor is a symmetric, 2nd rank tensor, containing 6 independent elements, 3 describing the magnitude and another 3 describing the principal direction of diffusion.

Although Eq. (2.8) provides a convenient and intuitive link between the MRI signal and the principal diffusion directions, it does not take into account the effect of the co-called gradient cross terms [17]. A more general expression for the diffusion tensor formalism can be written as:

$$I = I_0 exp\left(-\sum_{i=x,y,z}\sum_{j=x,y,z} b_{ij}D_{ij}\right) \tag{2.9}$$

where x, y, z represent the laboratory frame of reference. In Eq. (2.9), the diffusion tensor can be written in a matrix form as:

$$\boldsymbol{D} = \begin{bmatrix} D_{xx} & D_{xy} & D_{xz} \\ D_{xy} & D_{yy} & D_{yz} \\ D_{xz} & D_{yz} & D_{zz} \end{bmatrix} \tag{2.10}$$

And b_{ij} is the b-matrix [17] which can be calculated according to:

$$b = \gamma^2 \int_0^{TE} \left[\left(\int_0^t G(t')dt' \right)^T \left(\int_0^t G(t')dt' \right) \right] dt \qquad (2.11)$$

and G is an arbitrary time-varying diffusion-weighting vector of any orientation:

$$G(t) = \left[G_x(t), \; G_y(t), \; G_z(t) \right] \qquad (2.12)$$

Regardless on whether Eq. (2.8) or (2.9) is used, the typical DTI experiment consists of acquiring series of diffusion-weighted MRI scans with diffusion encoding gradients encoded along at least six non-collinear directions. Estimation of the diffusion tensor is usually performed on pixel-by-pixel basis, via appropriate curve fitting of the observed signals to the signal attenuation equation. The estimated diffusion tensor in Eq. (2.10) bears little use for inferring the tissue microstructure, since the relevant information is embedded in the tensor elements. Hence, the concept of "diffusion ellipsoid" has been proposed [17] to simplify the interpretation of the diffusion tensor. The diffusion ellipsoid is a 3-dimensional representation of the displacement profile covered in space by diffusing molecules during the diffusion time Δ [46]. The principal axes of the diffusion ellipsoid can be calculated by performing eigenvalue decomposition of Eq. (2.10) where the diffusion tensor gets converted into a product between a diagonal matrix of its eigenvalues $(D_1, D_2, \text{ and } D_3)$ and transformation (or rotation) matrix consisting of its eigenvectors $(e_1, e_2, \text{ and } e_3)$. The eigenvalues and the eigenvectors of the diffusion tensor correspond to the diffusivities as observed along the principal axes of diffusion ellipsoid and the orientations of its axes, respectively. The central premise of DTI is that the direction in which water diffusion is the fastest, which is the eigenvector of the largest diffusion tensor eigenvalue, coincides with the local tissue fiber orientation. To make the derived eigenvalues from the diffusion tensor more intuitive, the diffusion

tensor eigenvalues are commonly used to compute the mean diffusivity (MD) and fractional anisotropy (FA) index, given by:

$$MD = (D_1 + D_2 + D_3)/3 \qquad (2.13)$$

$$FA = \sqrt{\frac{3}{2}} \sqrt{\frac{(D_1 - MD)^2 + (D_2 - MD)^2 + (D_3 - MD)^2}{D_1^2 + D_2^2 + D_3^2}} \qquad (2.14)$$

where D_1, D_2, D_3 represent the eigenvalues of the DT matrix (in descending order). Mathematically, the MD is proportional to the average diffusion in the 3 principal axes. FA measures the fraction of the diffusion tensor that can be ascribed to anisotropic diffusion [46]. FA varies between 0 (isotropic diffusion) and 1 (infinite anisotropy). Lower FA values can be found in isotropic media (e.g., gray matter in the brain), whereas progressively higher FA reflects higher diffusion anisotropy (e.g., brain white matter). In practice, MD and FA have the feature of being rotationally invariant, i.e., do not depend on the orientations of the diffusion principal axes. This renders FA and MD as a convenient quantitative metrics that capture the overall magnitude of diffusion and the degree of diffusion anisotropy, respectively. Figure 2.3 shows MD and FA pixel maps of a healthy human heart specimen.

2.5 DTI Assessment of Myocardial Structure

The anisotropy and orientation of cardiomyocytes make the heart an excellent candidate for diffusion MRI techniques. Indeed, the first report documenting cardiac fiber mapping using DTI was published soon after DTI was introduced by Basser et al. [17]. In 1994, Garrido et al. [34] reported the detection of the known myocardial helical pattern in perfused rat heart by DTI, demonstrating the potential for utilizing DTI as a nondestructive technique to characterize the 3-dimensional myocardial fiber architecture.
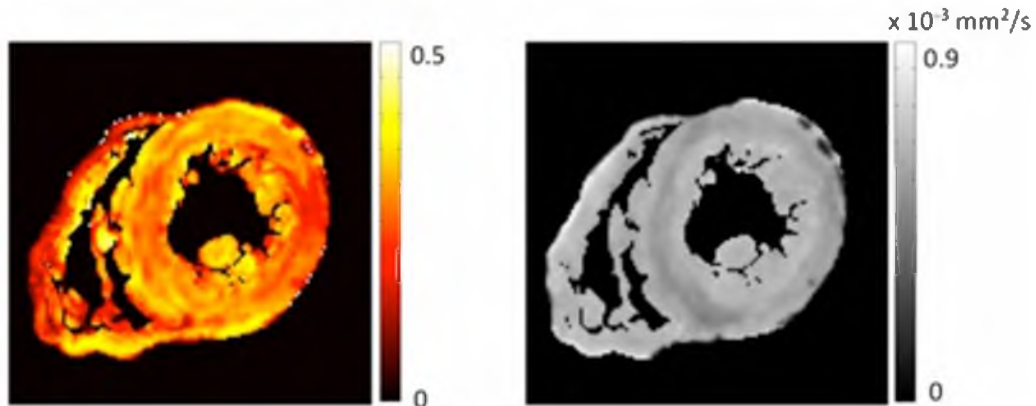
Figure 2.3. Pixel maps of Fractional Anisotropy (left) and Mean Diffusivity (right) obtained from a healthy human heart specimen.

2.6 Validation of DTI for Myocardial Fiber Orientation Mapping

As stated above, the main premise in DTI mapping of myocardial fiber structure is that the direction of fastest observed water diffusion (i.e., the primary eigenvector of the diffusion tensor) coincides with local fiber orientation. Histological correlation studies performed in freshly excised [36], perfused [37], and formalin fixed [38] myocardium provided strong support for the premise. Hsu et al. [36] correlated local fiber angle measurements obtained from DTI and histology, on a pixel-by-pixel basis, in a freshly excised specimen from the right ventricle of dog heart as shown in Fig. 2.4. Expanding on Hsu's study, Scollan et al. [37] used a perfused rabbit heart model to quantify and correlate DTI fiber orientation mapping with histology. Not only Scollan's study reaffirmed the findings by Hsu – that primary eigenvector obtained from DTI correlates closely with histological measures in the left ventricle, but they also demonstrated this correlation when the heart was perfused at physiologic conditions. Holmes et al. subsequently correlated the principal eigenvector obtained from DTI to histology in fixed rabbit hearts and reported less than 4° difference between fiber angles
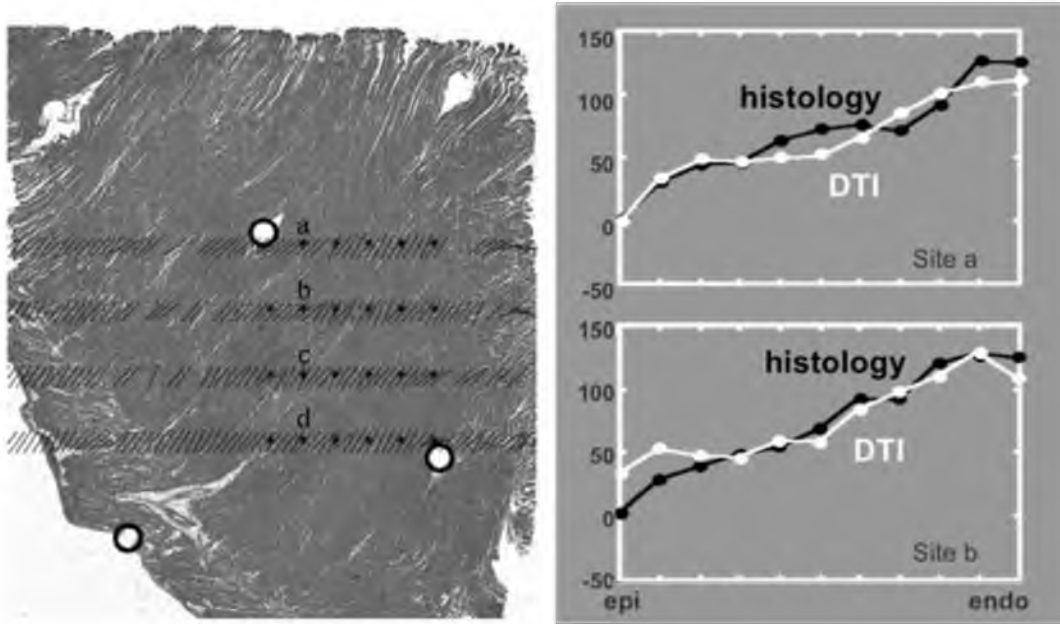
Figure 2.4. Validating DTI fiber mapping against histology. Fiber orientation obtained from DTI and histology show excellent agreement across the myocardial wall. Figure modified from Hsu et al. [36]; with permission.

measured from DTI and histology. The latter two studies suggest that neither physiologic perfusion nor tissue fixation adversely impacted the accuracy of fiber orientation mapping using DTI.

2.7 Sheet Structure Mapping via DTI

In 1995, LeGrice et al. [12] proposed that the ventricular myocardium is further organized into laminar substructures, referred to as sheets, or "sheetlets" as they do not form continuous structure traversing the whole heart [47]. The sheetlet planes are approximately 4-5 cardiomyocyte thick, with the myocytes in each sheet tightly coupled with a collagen network, while the adjacent sheets loosely connected to allow for slippage [12, 48]. However, because the initial study was performed on fixed myocardium which was susceptible to artifacts (e.g., shrinkage) related to the

preparation, the existence of laminar structure (or sheets) has been debated by some researchers [1]. Nevertheless, several cardiac DTI reports have linked the tertiary (smallest) eigenvector of the DTI matrix to the normal of the sheet plane [37,47–49]. Scollan et al. [37] suggested that the secondary and tertiary eigenvector of the diffusion tensor form a systematic pattern similar to the sheet structure proposed by Le Grice [12]. Scollan suggested that the sheet planes lay horizontally in the LV mid-wall and become more vertically oriented at the epicardium and endocardium. Tseng et al. [48] utilized optical images of inked prints obtained directly from the cut face of bovine heart specimens. The authors claimed that their inking method allows for DTI fiber mapping and the cleavage orientations in fresh specimens to be acquired under identical conditions, which minimizes the possibility of alterations of the tissue integrity between modalities (optical vs. DTI).

Together, although the supporting evidence is not as direct and unequivocal as the case of fiber orientation, results of cardiac DTI studies to date are consistent with the notion that the secondary and tertiary diffusion tensor eigenvectors respectively correspond to the orientation and the normal to the myocardial sheets.

2.8 DTI as a Function of the Cardiac Cycle

It is accepted that blood is ejected by the heart mainly via the contraction of its cardiomyocytes. However, the increase in cardiomyocyte diameter during contraction accounts for only 20% of the observed systolic wall thickening [12], which suggests that the dynamically changing hierarchical organization of the myocardium also plays an important role. DTI can provide unique insights on the states of the fiber and sheet rearrangement during contraction. Although different groups attempted to conduct DTI at

different points in the cardiac cycle [40, 50, 51], probably the most comprehensive investigation of myofiber rearrangement dynamics using DTI so far was the report by Hales et al. [47]. The authors imaged the same perfused heart (of a normal rat) at relaxed and contracted states. As shown in Fig. 2.5, the authors reported higher right-handed fibers percentage (in the endocardial wall) and lower left-handed fibers percentage (in the epicardial wall) in contracture state. They also suggested that the sheet angles follow a similar pattern of that demonstrated by Scollan [37] – in which the sheet planes at relaxed state lays parallel to the equatorial axis in the mid-wall, and become vertically orientated at the epi- and endocardial walls. Further, they also showed that the sheet angles rearrangement follows an accordion-like behavior in contracture state, in which the sheet planes become more vertically orientated (especially in the mid-wall) at contracture as shown in Fig. 2.5b. This study elegantly proposed a mechanism in which an accordion-like rearrangement of sheets combined with inter-sheet slippage can contribute to ventricular deformation, including centripetal wall-thickening (i.e., toward the center of the LV cavity) and baso-apical shortening.

2.9 Cardiac DTI in the Mammalian Species

To date, DTI has been used to characterize the fiber structure of normal hearts in several small and large animal species, including mouse, rat, rabbit, sheep, dog, in addition to human [34,51–54]. Despite differences in mammalian hearts, the general myocardial fiber architecture detected by DTI displays high degree of general similarity among different species, albeit there also exist important differences.
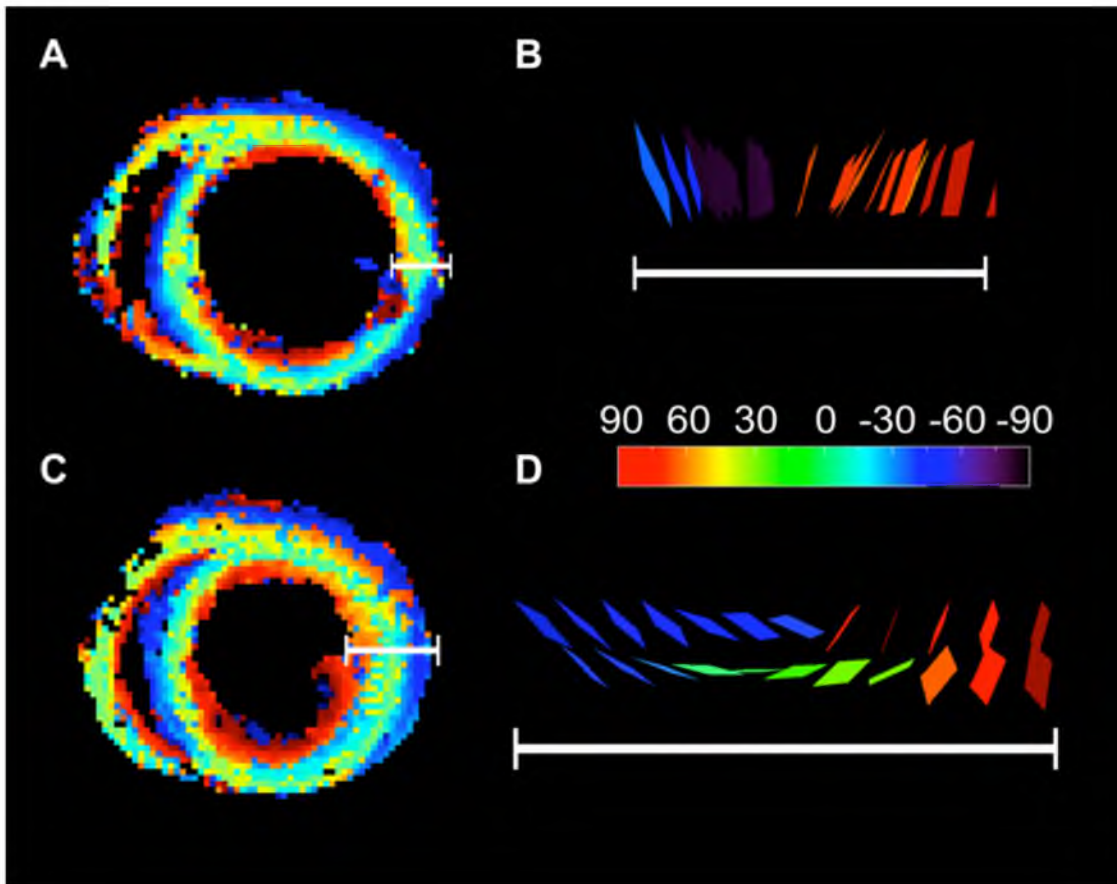
Figure 2.5. Helix angle maps of relaxed (A) and contracted states (C). Helix angles are represented by the colorbar. Color-coded rectangles on the right represent profiles of sheet arrangement in the transmural direction (taken from the white-bars) in relaxed (B) and contracted states (D). The sheet angles in B and D were calculated as the planes perpendicular to the smallest eigenvector obtained from the diffusion tensor. Obtained from Hales et al. [47]; with permission.

Healy et al. [55] compared the helix angle between mouse, rabbit and sheep. As shown in Fig. 2.6, although all three species showed the well-known counterclockwise rotation of the fiber helix angle in the LV, the range of endocardial to epicardial helix angle was significantly different among the species. The structural differences exist among hearts at least from animals of different sizes, suggesting caution is needed when extrapolating myocardial structures from one species to another in, for example, myocardial functional modeling studies.
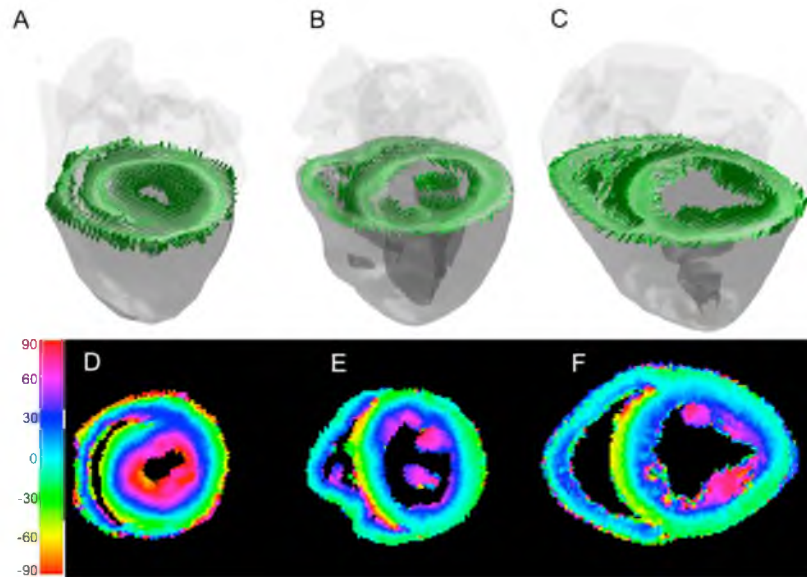
Figure 2.6. Myocardial fiber orientation in mouse (A,D), rabbit (B, E), and sheep (C,F). Top row shows cylindrical rods rendering of the fiber structure, while the bottom row show the color-coded helix angle map on pixel-by-pixel basis in short axis configuration. The colorbar on the left reports angles in degrees. Despite similarities of helix angle across species, significant differences exist in the range of fiber rotation from endocardium to epicardium. Figure obtained from Healy et al. [55]; with permission.

2.10 Applications in Cardiac Pathology

DTI has also been utilized to study cardiac pathologies in humans and animals for ischemic and non-ischemic cardiac disease, both *in vivo* and *ex vivo* [56–63]. The main parameters that have been reported are the scalar DTI parameters (especially FA and MD), and myocardial fiber orientation (helix and sheet angles).

For ischemic disease in animal models and humans, nearly all studies reported a decrease in FA and increase in MD in the infarcted myocardium compared to remote, unaffected normal regions of the same heart or to healthy control group [57, 59–62]. One infarcted mouse heart study reported the opposite trend in the infarct zone (i.e., lower MD and higher FA in infarct zone depending on heart extraction time post myocardial

infarction) [64]. The known helical pattern in the infarct and remote zones retains its general behavior (i.e., endocardium has positive right-handed helix fiber angles, denoted as RHF, and the epicardium has negative left-handed helix fiber angles, denoted as LHF). Most studies reported higher fiber angular deviation in the infarct compared to remote zone or in normal subjects. The fiber angular deviation was defined as the standard deviation of the helix angles in selected ROIs and used as a metric for the local fiber disarray. For example, a rat infarct model by Chen et al. [56] reported higher angular deviation in the infarcted myocardium and correlated the measurements from DTI with histology. Chen's finding was supported by Wu et al. [59] who reported in an infarcted porcine model higher angular deviation and lower helix angle range (defined as sub-endocardial minus sub-epicardial helix angle) in the infarct zone. Another study by Wu et al. [61] of infarcted porcine model reported lower RHF and higher LHF in the infarct and remote zones, which the authors referred to as "left-handed shift of fibers around the infarct zone".

In vivo DTI in human patients with acute myocardial infarction [58] and a follow up study on chronic infarct [60] was performed on the same subjects. In these human studies, the RHF percentage was decreased while the LHF increased in the infarct zone. Interestingly, these studies also reported that the opposite trend occur in the remote zone (i.e., increase in RHF and reduction in LHF in remote zone) [58], which is contrary to the porcine heart infarct study (in the remote zone) [61]. The authors hypothesized that compensatory responses affected the RHF and LHF in the remote and infarct zones such that the overall (LHF+RHF)/CF (where CF refers to mid-wall circumferential fibers percentage) would remain constant [58]. Collectively, a major finding [58,60,61] is that

the sub-endocardial RHF is implicated in the remodeling and healing process in the infarcted heart, and this notion was supported by non-DTI studies (e.g., [65]). Recently, Mekkaoui et al. [62] expanded on the conventional region-of-interest-based analyses by utilizing statistical approach to characterize the 3D helical fiber architecture in the full left ventricle. Mekkaoui utilized tractography-based helix angle classification and introduced the tractography coherence index, and applied this approach to study normal human, normal rat, and normal and infarcted sheep hearts [62]. Since this approach eliminated the subjectivity of selecting ROIs in heart, and treated the heart fiber structure as a continuum, to date this study seems to be the most robust study for fiber angle analysis in the heart. In the infarcted sheep myocardium, Mekkaoui [62] confirmed some of the finding reported in the previous ischemic human studies [59, 61], in which the LHF decreased in the remote zone, and he also showed that remodeling in the remote zone implicate all layers (endocardium, epicardium, and mid-wall).

DTI has also been applied to study cardiac remodeling in the non-ischemic heart disease, such as the dyssynchronous heart failure [57], and in hypertrophic cardiomyopathy [63]. Helm et al. [57] used a canine heart model of dyssynchronous heart failure and performed 3D DTI acquisition on the excised specimens. In diseased hearts, they reported regional reduction in wall thickness (septal, anterior, and posterior), but not in the lateral wall. They showed that the regional differences in the wall thickness were associated with rearrangement of sheet angles, whereas the septal wall became more vertically oriented compared to the lateral wall. The authors hypothesized that vertically oriented sheet angles could explain the reduction of wall thickness in the septal wall. Because electrical propagation in myocytes favors the direction along the main fibers axis

[3], the authors speculated that vertically-oriented sheet angles may be responsible for hindering the transmural electrical propagation, which may explain the observed dyssynchrony in certain segments of the diseased hearts.

In a study of hypertrophic cardiomyopathy by Tseng et al. [63], the authors performed *in vivo* DTI and strain imaging on human patients. They reported reduced fractional anisotropy and increased fiber disarray, which interestingly correlated with reduction in functional parameters (e.g., fiber and cross fiber strains). The authors then concluded that myofiber disarray in hypertrophic cardiomyopathy is correlated with abnormalities of both passive and active myocardial function [63].

2.11 Applications in Small Animals

Mapping the 3D myocardial fiber architecture can be performed routinely and in a relatively short time, at least compared to reconstructing a 3D volume from 2D histological dissection. However, compared to many other MRI techniques, DTI is inherently challenging due to the prolonged scan time and its low SNR (from diffusion encoding via signal attenuation). In the small animals (e.g. mouse), the challenges are exacerbated by the small imaging voxel size necessary to provide the anatomical details and, in the case of *in vivo* imaging, constraints imposed by the specific physiology (e.g., high heart rate) of the animals. Nonetheless, state-of-the-art dedicated small animal MRI scanners equipped with high performance gradient sets are capable of producing high-quality DTI fiber maps in several hours. Figure 2.7 shows 3D heart reconstruction from a mouse (right) and a rat (left), with the two images demonstrating one of the many possibilities to visualize the fiber structure in the heart. The simplest way to visualize the fiber orientation is by using the definition of the helix angle proposed by Streeter [11].
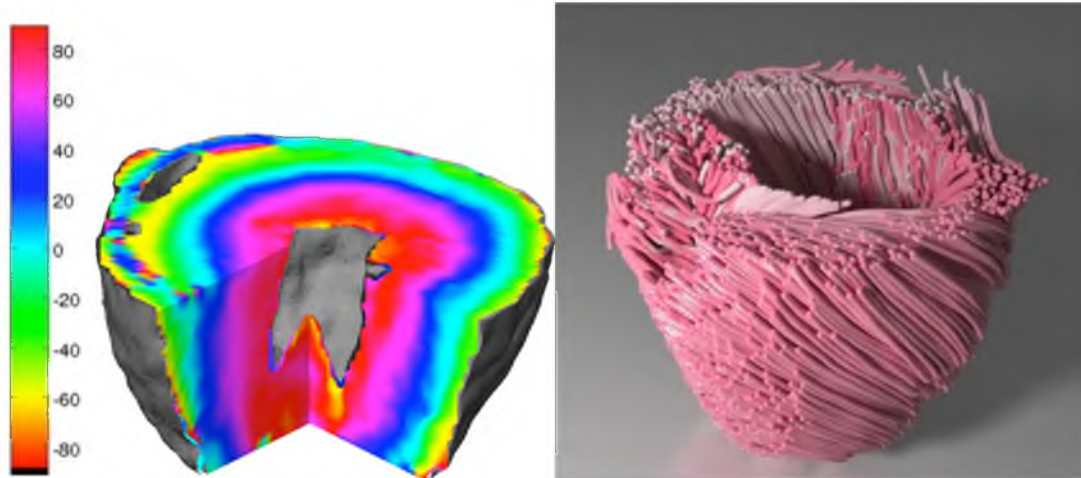
Figure 2.7. Left: color-coded helix angle map in *mouse* heart (resolution 100 *μm* isotropic, 12 diffusion gradient directions, scan time 9 hours). The colorbar on the left represent the helix angle value for each imaging voxel (in degrees). Right: Myocardial fiber mapping using DTI-tractography in a *rat* heart (resolution 150 *μm* isotropic, 12 diffusion gradient directions, scan time 16 hours.) Image on right is courtesy of Dr. Grant Gullberg from Berkeley National Lab.

The helix angle can be obtained from each imaging voxel by projecting the principal eigenvector of the diffusion tensor onto the tangential plane and then taking the angle between this projection and the horizontal (or equatorial) axis. Each angle can be assigned a different false color depending on its value as shown in the colorbar in Fig. 2.7. An alternative way to visualize fiber structure is by generating "tractography" [66] streamlines connecting principal eigenvectors of neighboring voxels as shown in the right panel of Fig. 2.7.

2.12 Technical Consideration for *In Vivo* DTI in Small Animals

Despite challenges arising from the beating motion of the heart and the sensitivity of diffusion-encoding to strain-memory effect [36, 68], *in vivo* cardiac DTI has been shown feasible, at least in humans [36, 40–42, 61, 68]. Moreover, although additional challenges exist, the feasibility of *in vivo* cardiac DTI in the mouse has been

demonstrated by recent reports, where diffusivity and fiber orientation information is used to characterize cardiac remodeling associated with ischemia and hypertrophy [69, 79]. Besides constraints imposed by scan time, resolution and SNR common to all DTI experiments, *in vivo* cardiac DTI in general face few additional challenges stem from the unique physiology of the heart. First, compared to other organs, the heart undergoes large and relatively periodic beating motion, which can cause pronounced ghosting and streaking artifacts along the phase encoding axis of an MR image. Although these motion artifacts can be greatly reduced by employing gated acquisitions (e.g., dual cardiac and ventilation-gated MRI), the heightened sensitivity of diffusion MRI to motion leaves very little room for uncorrected instrument imperfections, such as errors in gradients calibration or uncompensated eddy current effects. Second, to reduce the effects of bulk motion while providing sufficient degree of diffusion encoding, *in vivo* cardiac DTI is often performed using narrow diffusion encoding pulses across not one but two cardiac cycles using stimulated echo-based pulse sequences [35].

The contraction and expansion of the myocardium between the diffusion encoding gradient pulses can lead to erroneous estimates of diffusion induced by strain-memory effects [36, 68, 71], since tissue strain alters the relative displacements and phases of spins from which diffusion is encoded. Depending on the nature of the strain, if uncorrected, the effect can be either over- or under-estimation of the diffusion measurements. Because cardiac strain can be separately quantified via, for example, phase-contrast methods, one solution is to subtract its effects and produce corrected fiber orientation measurements from *in vivo* cardiac DTI data [67]. A second solution, based on the fact that the strain effects are dependent on the average strain across the cardiac

cycle, is to obtain strain-free *in vivo* cardiac DTI measurements by selecting the right timing delay in the cardiac-gated acquisition where the average strain is already zero [70].

Instead of working with myocardial strain, an alternative approach is to employ bipolar diffusion encoding gradient pulses, where spin phases are not left un-refocused across the cardiac cycle, which has been shown effective in minimizing the contribution of strain in *in vivo* cardiac DTI measurements [40, 41]. The main drawback of the approach is the reduced diffusion-weighting b-value that can be achieved using shortened diffusion times. Obviously the practical utility of bipolar gradient pulses depends on whether the required hardware, specifically whether high-performance gradients (in terms of both amplitude and slew rate), exists. Recently, advanced gradient hardware, capable of up to 300 mT/m for human brain imaging and 1500 mT/m in mouse systems as of the current writing, has been introduced. The latter has been credited for the feasibility of *in vivo* cardiac DTI in mice, where the fast heart rate of the animal (300—600 bpm) makes it all but impossible to conduct DTI without extremely large and narrow diffusion encoding pulses. Because the feasibility hinges on the availability of high-performance gradient systems relative to the animal heart rate, and that the performance of a gradient system in turn depends greatly on its size, the feasibility of *in vivo* cardiac DTI in other-size small animals (e.g., rats) remains to be demonstrated.

Besides strain, another physiologic source that can complicate *in vivo* cardiac DTI is perfusion. Perfusion (in this case blood flow in the capillary bed) has long been known for causing additional spin phase dispersion and leading to overestimated diffusion coefficients via the so called intravoxel incoherent motion effect [71] in highly

vascularized organs such as the liver [72]. Because the capillary flow is faster than the diffusion of water, the flow-mediated perfusion effects can be eliminated from diffusion measurements by employing sufficiently high (b > 200 s/mm^2) diffusion weighting. The perfusion dependence of diffusion MRI has been theorized [73,74] and recently empirically demonstrated *in vivo* [75] and for the perfused heart [76].

Combined, it is clear that the specific physiologies of the beating heart add technical challenges that need to be addressed for performing *in vivo* cardiac DTI. Technological advances have made most the known issues tractable, but there remains room for improvement. Until then, caution is warranted in interpreting *in vivo* cardiac DTI results.

2.13 Conclusion

Cardiac DTI has gained momentum in recent years. Advances in gradient hardware and motion compensation strategies allowed the acquisition of high quality DTI data in fixed and live, beating hearts. Not only cardiac DTI yields important information about the state of the cardiac microstructure, for example, via the fractional anisotropy or mean diffusivity indexes, but also reveals the dynamically changing hierarchical organization of the myocardium as manifested in the fiber and sheet angles. Cardiac DTI can potentially complement other well-established MRI techniques to monitor cardiac disease, such as late-gadolinium enhancement [77] to detect heart infarct, or T1 mapping to detect diffuse fibrosis [78] in the non-ischemic heart failure.

2.14 References

[1]   Anderson RH, Ho SY, Sanchez-Quintana D, Redmann K, Lunkenheimer PP. Heuristic problems in defining the three-dimensional arrangement of the ventricular myocytes. The Anatomical Record. 2006 Jun;288A(6):579–86.

[2]   Rijcken J, Bovendeerd PH, Schoofs a J, Van Campen DH, Arts T. Optimization of cardiac fiber orientation for homogeneous fiber strain during ejection. Annals of Biomedical Engineering. 1999;27(3):289–97.

[3]   Roberts DE, Hersh LT, Scher a. M. Influence of cardiac fiber orientation on wavefront voltage, conduction velocity, and tissue resistivity in the dog. Circulation Research. 1979 May 1;44(5):701–12.

[4]   Gilbert SH, Benson AP, Li P, Holden A V. Regional localisation of left ventricular sheet structure: integration with current models of cardiac fibre, sheet and band structure. European Journal of Cardio-Thoracic Surgery. 2007 Aug;32(2):231–49.

[5]   Guccione JM, Costat KD, Mccullocht AD. Finite ventricular element stress analysis of left mechanics in the beating dog heart. 1995;28(10).

[6]   Lunkenheimer PP, Redmann K, Kling N, Jiang X, Rothaus K, Cryer CW, et al. Three-dimensional architecture of the left ventricular myocardium. The anatomical record. Part A, Discoveries in molecular, cellular, and evolutionary biology. 2006 Jun;288(6):565–78.

[7]   Torrent-Guasp F, Ballester M, Buckberg GD, Carreras F, Flotats A, Carrió I, et al. Spatial orientation of the ventricular muscle band: physiologic contribution and surgical implications. The Journal of thoracic and cardiovascular surgery. 2001 Aug;122(2):389–92.

[8]   McCulloch AD. Cardiac biomechanics. In: Bronzino J, editor. The Biomedical Engineering Handbook. 2nd Editio. Boca Raton: CRC Press; 2000. p. 28–46.

[9]   Clayton RH, Bernus O, Cherry EM, Dierckx H, Fenton FH, Mirabella L, et al. Models of cardiac tissue electrophysiology: progress, challenges and open questions. Progress in Biophysics and Molecular Biology. Elsevier Ltd; 2011;104(1-3):22–48.

[10]   Clerc L. Directional differences of impulse spread in trabecular muscle from mammalian heart. J Physiol. 1976;255:335–46.

[11]   Streeter DD, Spotnitz HM, Patel DP, Ross J, Sonnenblick EH. Fiber orientation in the canine left ventricle during diastole and systole. Circulation research. 1969 Mar;24(3):339–47.

[12]   LeGrice IJ, Smaill BH, Chai LZ, Edgar SG, Gavin JB, Hunter PJ. Laminar structure of the heart: ventricular myocyte arrangement and connective tissue architecture in the dog. The American journal of physiology. 1995 Aug;269(2 Pt 2):H571–82.

[13]   Sachse FB. Computational cardiology: modeling of anatomy, electrophysiology, and mechanics. 1st ed. Goos G, Hartmanis J, van Leeuwen J, editors. New York, US:

Springer; 2004. p. 322.

[14]   Hunter PJ, McCulloch AD, Ter Keurs HE. Modelling the mechanical properties of cardiac muscle. Progress in biophysics and molecular biology. 1998 Jan;69:289–331.

[15]   Schmitt B, Fedarava K, Falkenberg J, Rothaus K, Bodhey NK, Reischauer C, et al. Three-dimensional alignment of the aggregated myocytes in the normal and hypertrophic murine heart. 2009;921–7.

[16]   Buckberg GD. Architecture must document functional evidence to explain the living rhythm. European journal of cardio-thoracic surgery : official journal of the European Association for Cardio-thoracic Surgery. 2005 Feb;27(2):202–9.

[17]   Basser PJ, Mattiello J, LeBihan D. MRI diffusion tensor spectroscopy and imaging. Biophysical Journal. 1994 Jan;66(1):259–67.

[18]   Tubbs RS, Gianaris N, Shoja MM, Loukas M, Cohen Gadol AA. "The heart is simply a muscle" and first description of the tetralogy of "fallot". early contributions to cardiac anatomy and pathology by bishop and anatomist niels stensen (1638-1686). International journal of cardiology. 2012 Feb 9;154(3):312–5.

[19]   Lower R. Tractus de corde. London: Translation by K. Franklin, Oxford University Press, 1932.; 1669.

[20]   Gibson A. Report cix. on the primitive muscle tissue of the human heart. British medical journal. 1909 Jan 16;1(2507):148.4–150.

[21]   Schäfer EA. A method of recording changes of volume by means of photography and its application to the plethysmographic record of the normal frog heart. J Physiol. 1884 Sep;5(3):[127]–129, 194–1.

[22]   Streeter DD, Hanna WT. Engineering mechanics for successive states in canine left ventricular myocardium. Circulation Research. 1973 Dec;33(6):656–64.

[23]   Armour JA, Randall WC. Structural basis for cardiac function. The American journal of physiology. 1970 Jun;218(6):1517–23.

[24]   Freeman GL, LeWinter MM, Engler RL, Covell JW. Relationship between myocardial fiber direction and segment shortening in the midwall of the canine left ventricle. Circulation research. 1985 Jan;56(1):31–9.

[25]   Tezuka F, Hart W, Lange PE, Nürnberg JH. Muscle fiber orientation in the development and regression of right ventricular hypertrophy in pigs. Pathology International. Wiley Online Library; 1990;40(6):402–7.

[26]   McLean M, Prothero J. Myofiber orientation in the weanling mouse heart. The

American journal of anatomy. 1991 Dec;192(4):425–41.

[27]   Pearlman ES, Weber KT, Janicki JS. Quantitative histology of the hypertrophied human heart. Federation proceedings. 1981 May 15;40(7):2042–7.

[28]   Pearlman ES, Weber KT, Janicki JS, Pietra GG, Fishman AP. Muscle fiber orientation and connective tissue content in the hypertrophied human heart. Laboratory investigation; a journal of technical methods and pathology. 1982 Feb;46(2):158–64.

[29]   Lasher R a, Hitchcock RW, Sachse FB. Towards modeling of cardiac micro-structure with catheter-based confocal microscopy : a novel approach for dye delivery and tissue characterization. IEEE transactions on medical imaging. 2009 Aug;28(8):1156–64.

[30]   Sowerby AJ, Harries J, Diakun GP, Towns-Andrews E, Bordas J, Stier A. X-ray diffraction studies of whole rat heart during anoxic perfusion. Biochemical and biophysical research communications. 1994 Aug 15;202(3):1244–51.

[31]   Yagi N, Shimizu J, Mohri S, Araki J, Nakamura K, Okuyama H, et al. X-ray diffraction from a left ventricular wall of rat heart. Biophysical journal. 2004 Apr;86(4):2286–94.

[32]   Aslanidi O V, Nikolaidou T, Zhao J, Smaill BH, Gilbert SH, Holden A V, et al. Application of micro-computed tomography with iodine staining to cardiac imaging, segmentation, and computational model development. IEEE transactions on medical imaging. 2013 Jan;32(1):8–17.

[33]   Vignaud A, Rodriguez I, Ennis DB, DeSilva R, Kellman P, Taylor J, et al. Detection of myocardial capillary orientation with intravascular iron-oxide nanoparticles in spin-echo MRI. Magn Reson Med. 2006 Apr;55(4):725–30.

[34]   Garrido L, Wedeen VJ, Kwong KK, Spencer UM, Kantor HL. Anisotropy of water diffusion in the myocardium of the rat. Circulation Research. 1994 May 1;74(5):789–93.

[35]   Reese TG, Weisskoff RM, Smith RN, Rosen BR, Dinsmore RE, Wedeen VJ. Imaging myocardial fiber architecture *in vivo* with magnetic resonance. Magn Reson Med. 1995 Dec;34(6):786–91.

[36]   Hsu EW, Muzikant AL, Matulevicius SA, Penland RC, Henriquez CS. Magnetic resonance myocardial fiber-orientation mapping with direct histological correlation. Am J Physiol Heart Circ Physiol. 1998 May;274(5 Pt 2):H1627–34.

[37]   Scollan DF, Holmes A, Winslow R, Forder J, Gilbert SH, Benoist D, et al. Histological validation of myocardial microstructure obtained from diffusion tensor magnetic resonance imaging. Am J Physiol Heart Circ Physiol. 1998 Dec;275(6 Pt

2):H2308–H2318.

[38]   Holmes A, Scollan DF, Winslow RL. Direct histological validation of diffusion tensor MRI in formaldehyde-fixed myocardium. Magn Reson Med. 2000 Jul;44(1):157–61.

[39]   Dou J, Reese TG, Tseng W-YI, Wedeen VJ. Cardiac diffusion MRI without motion effects. Magn Reson Med. 2002 Jul;48(1):105–14.

[40]   Gamper U, Boesiger P, Kozerke S. Diffusion imaging of the *in vivo* heart using spin echoes-considerations on bulk motion sensitivity. Magn Reson Med. 2007 Feb;57(2):331–7.

[41]   Nielles-Vallespin S, Mekkaoui C, Gatehouse P, Reese TG, Keegan J, Ferreira PF, et al. *In vivo* diffusion tensor MRI of the human heart: reproducibility of breath-hold and navigator-based approaches. Magn Reson Med. in press.

[42]   McGill L-A, Ismail TF, Nielles-Vallespin S, Ferreira P, Scott AD, Roughton M, et al. Reproducibility of *in vivo* diffusion tensor cardiovascular magnetic resonance in hypertrophic cardiomyopathy. Journal of Cardiovascular Magnetic Resonance. 2012 Dec 24;14(1):86.

[43]   Hahn E. Spin echoes. Physical Review. 1950;80(4):580–94.

[44]   Carr H, Purcell E. Effects of diffusion on free precession in nuclear magnetic resonance experiments. Physical Review. 1954;94(3):630–8.

[45]   Stejskal EO, Tanner JE. Spin diffusion measurements: spin echoes in the presence of a time-dependent field gradient. J Chemical Physics. 1965;42(1):288.

[46]   Le Bihan D, Mangin JF, Poupon C, Clark C a, Pappata S, Molko N, et al. Diffusion tensor imaging: concepts and applications. Journal of Magnetic Resonance Imaging. 2001 Apr;13(4):534–46.

[47]   Hales PW, Schneider JE, Burton R a B, Wright BJ, Bollensdorff C, Kohl P. Histo-anatomical structure of the living isolated rat heart in two contraction states assessed by diffusion tensor MRI. Progress in Biophysics and Molecular Biology. Elsevier Ltd; 2012;110(2-3):319–30.

[48]   Tseng W-YI, Wedeen VJ, Reese TG, Smith RN, Halpern EF. Diffusion tensor MRI of myocardial fibers and sheets: correspondence with visible cut-face texture. Journal of Magnetic Resonance Imaging. 2003 Jan;17(1):31–42.

[49]   Chen J, Liu W, Zhang H, Lacy L, Yang X, Song S-K, et al. Regional ventricular wall thickening reflects changes in cardiac fiber and sheet structure during contraction: quantification with diffusion tensor MRI. Am J Physiol Heart Circ Physiol. 2005 Nov;289(5):H1898–907.

[50]   Mekkaoui C, Nielles-vallespin S, Gatehouse PD, Jackowski MP, Firmin DN, Sosnovik DE. Diffusion MRI tractography of the human heart *in vivo* at end-diastole and end-systole. In Proceedings of the 15th Annual SCMR Scientific Sessions, Orlando, FL, USA. BioMed Central Ltd; 2012;14(Suppl 1):O49.

[51]   Jiang Y, Pandya K, Smithies O, Hsu EW. Three-dimensional diffusion tensor microscopy of fixed mouse hearts. Magn Reson Med. 2004 Sep;52(3):453–60.

[52]   Dou J, Xia L, Zhang Y, Shou G, Wei Q, Liu F, et al. Mechanical analysis of congestive heart failure caused by bundle branch block based on an electromechanical canine heart model. Physics in Medicine and Biology. 2009 Jan 21;54(2):353–71.

[53]   Jiang Y, Guccione JM, Ratcliffe MB, Hsu EW. Transmural heterogeneity of diffusion anisotropy in the sheep myocardium characterized by MR diffusion tensor imaging. Am J Physiol Heart Circ Physiol. 2007 Oct;293(4):H2377–84.

[54]   Rohmer D, Sitek A, Gullberg GT. Reconstruction and visualization of fiber and laminar structure in the normal human heart from *ex vivo* diffusion tensor magnetic resonance imaging. Investigative Radiology. 2007;42(11):777–89.

[55]   Healy LJ, Jiang Y, Hsu EW. Quantitative comparison of myocardial fiber structure between mice, rabbit, and sheep using diffusion tensor cardiovascular magnetic resonance. Journal of Cardiovascular Magnetic Resonance. 2011 Jan;13:74.

[56]   Chen J, Song S-K, Liu W, McLean M, Allen JS, Tan J, et al. Remodeling of cardiac fiber structure after infarction in rats quantified with diffusion tensor MRI. Am J Physiol Heart Circ Physiol. 2003 Sep;285(3):H946–54.

[57]   Helm PA, Younes L, Beg MF, Ennis DB, Leclercq C, Faris OP, et al. Evidence of structural remodeling in the dyssynchronous failing heart. Circulation Research. 2006 Jan 6;98(1):125–32.

[58]   Wu M, Tseng W-YI, Su MM, Liu C, Chiou K-R, Wedeen VJ, et al. Diffusion tensor magnetic resonance imaging mapping the fiber architecture remodeling in human myocardium after infarction: correlation with viability and wall motion. Circulation. 2006 Sep 5;114(10):1036–45.

[59]   Wu Y, Tse H-F, Wu EX. Diffusion tensor MRI study of myocardium structural remodeling after infarction in porcine model. IEEE Engineering in Medicine and Biology Society. 2006. p. 1069–72.

[60]   Wu M-T, Su M-YM, Huang Y-L, Chiou K-R, Yang P, Pan H-B, et al. Sequential changes of myocardial microstructure in patients postmyocardial infarction by diffusion-tensor cardiac MR: correlation with left ventricular structure and function. Circulation Cardiovascular Imaging. 2009 Jan;2(1):32–40.

[61]   Wu EX, Wu Y, Nicholls JM, Wang J, Liao S, Zhu S, et al. MR diffusion tensor imaging study of postinfarct myocardium structural remodeling in a porcine model. Magn Reson Med. 2007 Oct;58(4):687–95.

[62]   Mekkaoui C, Huang S, Chen HH, Dai G, Reese TG, Kostis WJ, et al. Fiber architecture in remodeled myocardium revealed with a quantitative diffusion CMR tractography framework and histological validation. Journal of Cardiovascular Magnetic Resonance. Journal of Cardiovascular Magnetic Resonance; 2012 Jan;14(1):70.

[63]   Tseng W-YI, Dou J, Reese TG, Wedeen VJ. Imaging myocardial fiber disarray and intramural strain hypokinesis in hypertrophic cardiomyopathy with MRI. Journal of Magnetic Resonance Imaging. 2006 Jan;23(1):1–8.

[64]   Strijkers GJ, Bouts A, Blankesteijn WM, Peeters THJM, Vilanova A, Van Prooijen MC, et al. Diffusion tensor imaging of left ventricular remodeling in response to myocardial infarction in the mouse. NMR in Biomedicine. 2009 Feb;22(2):182–90.

[65]   Natali AJ, Wilson LA, Peckham M, Turner DL, Harrison SM, White E. Different regional effects of voluntary exercise on the mechanical and electrical properties of rat ventricular myocytes. The Journal of Physiology. 2002 May 3;541(3):863–75.

[66]   Sosnovik DE, Wang R, Dai G, Reese TG, Wedeen VJ. Diffusion MR tractography of the heart. Journal of cardiovascular magnetic resonance. 2009 Jan;11:47.

[67]   Reese T, Wedeen V, Weisskoff R. Measuring diffusion in the presence of material strain. Journal of Magnetic Resonance. 1996 Sep;112(3):253–8.

[68]   Huang S, Mekkaoui C, Chen HH, Wang R, Ngoy S, Liao R, et al. Serial diffusion tensor MRI and tractography of the mouse heart *in vivo*: impact of ischemia on myocardial microstructure. From 2011 SCMR/Euro CMR Joint Scientific Sessions Nice, France. 2011. p. O28.

[69]   Huang S, Polasek M, Chen H, Wang R, Ngoy S, Liao R, et al. Molecular and microstructural changes accompanying left ventricular hypertrophy revealed with *in vivo* diffusion tensor MRI (dti) and molecular imaging of the mouse heart. In Proceedings of the 19th Annual Meeting of ISMRM. 2011.

[70]   Tseng WI, Reese TG, Weisskoff RM, Wedeen VJ. Cardiac diffusion tensor MRI *in vivo* without strain correction. Magn Reson Med. 1999;403(May):393–403.

[71]   Le Bihan D, Breton E, Lallemand D, Aubin M-L, Vignaud J, Laval-Jeantet M. Separation of diffusion and perfusion in intravoxel incoherent motion MR imaging. Radiology. 1988;168(2):497–505.

[72]   Luciani A, Vignaud A, Cavet M, Van Nhieu JT, Mallat A, Ruel L, et al. Liver

cirrhosis : intravoxel incoherent motion MR imaging — pilot study. Radiology. 2008;249(3):891–9.

[73]   Le Bihan D, Breton E, Lallemand D, Aubin M-L, Vignaud J, Laval-Jeantet M. Separation of diffusion and perfusion in intra voxel incoherent motion MR imaging. Radiology. 1988;168:497–505.

[74]   Le Bihan D, Turner R. The capillary network: a link between ivim and classical perfusion. Magn Reson Med. 1992 Sep;27(1):171–8.

[75]   Callot V, Bennett E, Decking UKM, Balaban RS, Wen H. *In vivo* study of microcirculation in canine myocardium using the ivim method. Magn Reson Med. 2003 Sep;50(3):531–40.

[76]   Abdullah O, Gomez AD, Merchant S, Stedham O, Heidinger M, Poelzing S, et al. Effects of perfusion on cardiac MR diffusion measurements. Proceedings of the 21st Annual Meeting of ISMRM. Salt Lake City; 2012.

[77]   Kim RJJ, Fieno DSS, Parrish TBB, Harris K, Chen E, Simonetti O, et al. Relationship of MRI delayed contrast enhancement to irreversible injury, infarct age, and contractile function. Circulation. 1999;1992–2002.

[78]   Messroghli D, Nordmeyer S, Dietrich T, Dirsch O, Kaschina E, Savvatis K, et al. Assessment of diffuse myocardial fibrosis in rats using small animal look-locker inversion recovery (salli) t1 mapping. Circulation Cardiovascular Imaging. 2011 Sep 14;4(6):636–40.

CHAPTER 3

CHARACTERIZATION OF DIFFUSE FIBROSIS IN THE FAILING

HUMAN HEART VIA DIFFUSION TENSOR IMAGING AND

QUANTITATIVE HISTOLOGICAL VALIDATION [1]

3.1 Abstract

Non-invasive imaging techniques are highly desirable as an alternative to conventional biopsy for characterizing remodeling of tissues associated with disease progression, including end-stage heart failure. Cardiac diffusion tensor imaging (DTI) has become an established method for characterizing myocardial microstructure. However, the relationships between diffuse myocardial fibrosis, which is a key biomarker for staging and treatment planning of the failing heart, and measured DTI parameters have yet to be systematically investigated. In this study, DTI was performed on left ventricular specimens collected from patients with chronic end-stage heart failure due to idiopathic dilated cardiomyopathy (n=14) and from normal donors (n=5). Scalar DTI parameters, including fractional anisotropy (FA), mean (MD), primary (D_1), secondary (D_2), and

tertiary (D_3) diffusivities, were correlated to collagen content measured by digital microscopy. Compared to hearts from normal subjects, the FA in failing hearts decreased by 22%, whereas the MD, D_2 and D_3 increased by 12%, 14%, and 24%, respectively ($P <$ 0.01). No significant change was detected for D_1 between the two groups. Furthermore, significant correlation was observed between the DTI scalar indices and quantitative histological measurements of collagen (i.e., fibrosis). Pearson's correlation coefficient (r) between collagen content and either FA, MD, D_2, and D_3 was -0.51, 0.59, 0.56 and 0.62 ($P <$ 0.05), respectively. The correlation between D_1 and collagen content was not significant ($r = 0.46$, $P = 0.05$). Computational modeling analysis indicated that the behaviors of the DTI parameters as a function of the degree of fibrosis were well explained by compartmental exchange between myocardial and collagenous tissues. Combined, these findings suggest that scalar DTI parameters can be used as metrics for noninvasive quantification of diffuse fibrosis in failing hearts.

3.2 Introduction

End stage heart failure (HF) is a major public health problem with high mortality, morbidity and cost to the healthcare systems in the US and Europe [1], [2]. The disease is characterized by adverse changes in cardiac structure and function as a result of mechanical, neurohormonal, and cardiorenal factors [3]. One of the main factors leading to HF is the development of pathological myocardial fibrosis. Abnormally high collagen content adversely impacts the mechanical [4] and electrical [5] behaviors of the myocardium, and has been linked to increased risk of ventricular and atrial tachyarrhythmias and sudden cardiac death [6].

Myocardial fibrosis has been classified into reparative or reactive [7]. In

myocardial infarction (MI), fibrotic scar forms as macroscopic patches of collagen following myocytes necrosis to protect the myocardium from rupturing, and is thus called reparative fibrosis. On the other hand, collagen that develops in the remote zone to infarcts or in non-ischemic cardiac disease (such as dilated cardiomyopathy or cardiac hypertrophy) manifests as microscopic collagen depositions in the interstitial space and is termed reactive or diffuse fibrosis. Diffuse fibrosis is known to increase ventricular stiffness and leads to pump dysfunction [7], [8], and has been suggested to play a more detrimental role in structural remodeling in ischemic disease than the fibrotic scarring [9]. To date, tissue biopsy and histology remain the goldstandard method for quantifying structural remodeling in HF for staging and treatment planning of the disease [10], [11]. However, the invasive and laborious nature of the histological procedures presents a practical limitation on the number of sites and time points that can be practically performed. Hence, non-invasive imaging techniques for quantifying myocardial diffuse fibrosis are highly desirable.

Magnetic resonance diffusion tensor imaging (MR-DTI, or DTI for short), which captures the dependence of tissue water diffusion on the molecular environment [12], has emerged as an established, non-invasive alternative to histology for characterizing myocardial tissue microstructure. Technically, DTI yields a second-rank, symmetric matrix that describes both the direction and magnitude of the diffusion anisotropy, which can in turn be used to infer the underlying tissue organization, geometry and content. For example, the direction in which diffusion is the fastest (i.e., the eigenvector of the largest diffusion tensor eigenvalue) has been found to coincide with the local fiber orientation in freshly excised [13], perfused [14], and formalin-fixed [15] myocardium. Moreover, the

eigenvector of the second diffusion tensor eigenvalue has been associated with the orientation of myocardial sheet structure [16]. So far, DTI has been used to characterize the structures of normal hearts in a variety of small and large animal models [17]–[21], in addition to humans [22].

Diffusion tensor imaging has also been utilized to evaluate the structural remodeling associated with cardiac pathologies of both ischemic and non-ischemic origins. Studies of ischemic injury have reported a reduction in the degree of diffusion anisotropy coupled with an increase of water diffusivity in the infarct zone [23]–[26]. Additionally, DTI has been utilized in assessing nonischemic cardiac disease, such as dyssynchronous HF [27], hypertrophic cardiomyopathy [28], and dilated cardiomyopathy [29]. Besides changes in the fiber orientation, the diseased myocardium (e.g., hypertrophy or dilated cardiomyopathy) is generally found to have decreased diffusion anisotropy [28], [29] and increased water diffusivity [29]. Although the latter changes suggest that microscopic environment for water diffusion has become less restrictive, and can be associated with myocardial fibrosis, the exact relationships between myocardial fibrosis and the DTI parameters remain yet to be determined.

Beyond the empirical observations, to better understand the origin and predict the behavior of the relationship, it is also useful to explore the biophysical basis of dependence of the measured DTI indices on myocardial collagen content. Compartmental exchange models have been used to approximate the behavior of the MRI signal arising from a heterogeneous microscopic environment [30], [31], which is to be expected of the fibrotic myocardium. In the so-called fast-exchange situation, water spins spend much shorter time in the compartments than the temporal-length scale of their molecular

dynamics. Then the MRI parameters (e.g., relaxation rate and diffusion constants) of the aggregate system behave like the fractional volume-weighted sum of the same parameters of the individual compartments. Conversely, under the slow-exchange limit, the overall MRI signal is simply the proportional superposition of the signals from the individual compartments, as if the latter are completely independent. Bi-compartmental slow exchange models have been used to describe the MRI diffusion signal, including DTI, observed in the myocardium [32], [33]. Although it is unclear whether the behavior of the fibrotic myocardium is better described by the fast or slow-exchange model, either mechanism provides a possible starting point to explain the role in which diffuse fibrosis contributes to the MRI signal of the diseased myocardium.

Taken together, the present study aims to quantify the relationship between the DTI parameters and diffuse fibrosis, and to explore the biophysical explanations of the relationships. While fiber orientation remodeling associated with heart diseases has been examined in previous studies [27], [28], the current work focuses on the scalar DTI parameters. To reduce measurement subjectivity, histological examination of the myocardium is performed using state-of-the-art, whole-field digital microscopy for comprehensive endocardium-to-epicardium evaluation, followed by quantitative image analysis [34]. Findings of the current study are expected to be important for assessing the utility of DTI, and to pave the way for the technique to be used in eventual *in vivo* studies on HF patients.

3.3 Methods

3.3.1 Study Population and Specimen Collection

The study was approved by the Institutional Review Board at the University of Utah. The study group comprised 14 patients with chronic end-stage HF due to idiopathic dilated cardiomyopathy who required implantation of a left ventricular assist device (LVAD) for either bridge to heart transplantation or destination therapy in 2010. All patients met the medical policy guideline of the New York Heart Association (NYHA) class IIIb/IV for HF. The control group consisted of five donors whose hearts were determined to be functionally and structurally normal but were not suitable for transplantation due to non-cardiac reasons. Heart specimens were collected at the time of LVAD implantation by excising approximately a 1 x 1 x 1 cm^3 transmural plug from the left ventricular apex. The normal hearts were collected as intact specimens. All specimens were fixed in 10% buffered formalin for at least 24 h prior to further examination. Demographic, clinical, echocardiographic, hemodynamic and laboratory data were collected 48-72 h prior to surgery and tissue collection. The collected information from patients with end-stage HF and from normal donors is shown in Table 3.1. HF in the diseased group was confirmed by the left ventricle ejection fraction, which was almost four times lower than that of the normal group. All subjects with HF had non-ischemic cardiomyopathies and are expected to have predominantly diffuse fibrosis.

3.3.2 MRI Acquisition and Analysis

MRI experiments were conducted on a Bruker 7.0 T horizontal bore MRI scanner (Bruker Biospin, Ettlinegn, Germany) interfaced with 12.0 cm-diameter actively shielded gradient insert (BGA12S) capable of producing magnetic field gradients of up to 600

Table 3.1 - Baseline characteristics of the 14 patients with chronic HF due to idiopathic dilated cardiomyopathy, and 5 normal donors.

Parameter	HF Patients (N=14)	Normal Donor (N=5)
Age, years	52 ± 14.8	21 ± 3.6
Male gender	84%	60%
HF etiology		
IDC	100%	n/a
ICMP	0%	n/a
NYHA class		
II	6%	n/a
III	47%	n/a
IV	47%	n/a
LVEF, %	16 ± 6.1	62 ± 6
LVEDD, cm	6.8 ± 0.99	4.1 ± 0.41
LVESD, cm	6.2 ± 1.0	2.7 ± 0.32
RAP, mm Hg	12 ± 5.9	7 ± 3.1
PASP, mmHg	49 ±13.5	-
MPAP, mm Hg	34 ± 9.9	-
PCWP, mm Hg	22 ± 10.0	7.2 ± 1.6
PVR, Woods units	4.1 ± 3.2	-
CI, LPM/m^2	1.8 ± 0.7	3.5 ± 0.5

mT/m. Each heart specimens was placed in a sealed container filled with susceptibility matching fluid (Fomblin, Solvay Solexis, NJ, USA). A combination of a linear volume coil (72 mm ID) for signal transmission and a quadrature surface coil (25 mm diameter) for signal reception were used to acquire the DTI datasets.

DTI acquisition was performed using a standard multi-slice diffusion-weighted spin echo sequence with the following imaging parameters: TR/TE 2000/30 ms; matrix size, 64 x 64; in-plane resolution, 1.5 mm; four transverse slices; thickness, 1.0 mm. Diffusion was encoded along a set of 12 optimized gradient directions [35], using a pair of trapezoidal gradient pulses [rise time, 0.25 ms; duration (δ), 4.00 ms; separation (Δ), 10.00 ms] equivalent to a nominal b-value of 1500 s/mm^2. The average signal-to-noise

ratio for the non-diffusion-weighted image (B0) was 80. The total scan time for each specimen was approximately 28 min.

Post-processing computation was performed using custom-codes written in Matlab (Version R2010a, Mathworks, MA) as described previously [12]. Briefly, diffusion tensors were estimated on a pixel-by-pixel basis from the MR diffusion images and diagonalized to yield the 3 eigenvalues (D_1, D_2 and D_3, in sorted descending order and commonly referred to as primary, secondary, and tertiary diffusivities, respectively) and eigenvectors, which are equivalent to the speeds and principal axes of diffusion, respectively. The diffusion tensor eigenvalues were in turn used to obtain the mean diffusivity (MD) and fractional anisotropy (FA), which represent the magnitude of diffusion and degree of anisotropy, respectively, and are commonly used scalar indices for characterizing tissue microstructure [36]. MD and FA were reported as averages over the entire myocardial area on all 4 image slices for each specimen. The average area of the selected ROIs across all samples was 3.16 ± 0.32 cm^2 (n = 19, mean $\pm$ SEM). To determine the underlying source of observed changes in the MD or FA, averages of the principal diffusivity terms D_1, D_2, and D_3 were similarly obtained.

3.3.3 Histology: Whole-Field Digital Microscopy

For histology, the specimens were dehydrated in progressively higher concentrations of alcohol, cleared through xylene and embedded in paraffin. Each specimen was cut into 4 μm-thick sections and mounted on glass slides. It was then evaluated on a whole-field basis spanning the entire myocardial wall (epicardium to endocardium) using a ScanScope XT digital histopathology system equipped with the ImageScope 10.0 image analysis software (Aperio Technologies, CA) as described

previously [34]. Quantitative histological measurements to quantify diffuse fibrosis percentage in the heart specimen were conducted using Masson's trichrome stain for collagen content evaluation. The collagen content was automatically quantified by identifying, counting and expressing the number of blue-staining pixels as a percentage of the total tissue area [34]. Because of the relatively low spatial resolution of the DTI scans (1.5 mm), which was insufficient to directly visualize the interstitial content, the degree of diffuse fibrosis was approximated by the total collagen detected on the whole histological slide (endocardium to epicardium).

3.3.4 Statistical Analysis

Statistical analysis was performed using GraphPad Prism (Version 5.0a, GraphPad Software Inc., CA). Variables were reported as mean and standard error of the mean (SEM). All parameters measured in the current study, including both DTI and histological indices, were compared between the failing and normal control groups using two-tailed unpaired t-tests. A P-value less than 0.05 was considered to be statistically significant. Correlation between DTI and histological indices was determined by evaluating the Pearson's correlation coefficients (r) for all pairings of MRI and histology parameters.

3.3.5 Computational Compartmental Analysis

Computational simulations were performed as a means to explain the behavior of the DTI experiment in the myocardium with varying amount of fibrosis. Monte Carlo simulations of DTI parameters that would have been measured in standard DTI experiments were conducted assuming that the diffusion signal originated from either fast

or slow compartmental exchange between myocardial and collagenous tissues. As a first approximation, the myocardium was assumed to consist of the normal myocardial and collagen (i.e., non-fibrous and fibrous) compartments, with the former lumping together myocytes and supporting cells, and normal interstitial and vascular spaces in a single compartment. For fast-exchange, the MRI signal intensity I_j^{fast} for the jth diffusion encoding gradient direction g_j was modeled after a two-compartment MR diffusion equation [37] adapted for DTI,

$$I_j^{fast} = exp(-b\, \boldsymbol{g}_j^T \cdot \left[(1 - f')\, \boldsymbol{D}_{myo} + f'\boldsymbol{D}_{col}\right] \cdot \boldsymbol{g}_j\,),\qquad(3.1)$$

where $\mathbf{D}_{myo}$ and $\mathbf{D}_{col}$ denoted the diffusion tensors for the myocardial and collagen compartments, respectively, and b is the scalar diffusion encoding sensitivity. Similarly, the slow-exchange signal equation followed one given previously [33],

$$I_j^{slow} = (1 - f')\, exp\left(-b\boldsymbol{g}_j^T \cdot \boldsymbol{D}_{myo} \cdot \boldsymbol{g}_j\,\right) + f'\, exp\left(-b\boldsymbol{g}_j^T \cdot \boldsymbol{D}_{col} \cdot \boldsymbol{g}_j\,\right).\qquad(3.2)$$

In both Eq. (3.1) and (3.2), the adjusted fractional volume f', given as

$$f' = \frac{f - f_0}{1 - f_0},\qquad(3.3)$$

was used instead of the nominal fractional volume f for the collagen compartment size in order to account for the small but non-negligible level of collagen content f_0 intrinsically found in the normal myocardium.

The mean principal diffusivities determined for the experimental control group in the current study (or D_1, D_2 and D_3 of 0.88, 0.64 and 0.51 $\times 10^{-3}$ mm^2/s, respectively) were used to construct the diagonal $\mathbf{D}_{myo}$. The mean collagen content for the same group (7%) was used as f_0. Because DTI parameters for the collagenous compartment were not directly measured in the current study, diffusion properties previously reported [38], [39]

for collagenous tissues (or 1.2 $\times 10^{-3}$ mm^2/s each D_1, D_2 and D_3) were used for the diagonal $\mathbf{D}_{col}$. As a result of the rather low anisotropy of diffusion in collagenous tissues, with FA reported in the 0.05-0.12 range [39], [40], $\mathbf{D}_{col}$ was assumed to be isotropic.

To avoid the directional dependence of measurement accuracy inherent in each set of encoding gradient directions [35], the diagonal $\mathbf{D}_{myo}$ was randomly rotated in 3D space and used in Eqs. [1] and [2] to estimate the diffusion signal intensities under simulated but same experimental conditions (e.g., diffusion-encoding directions and b-value) employed in the current study.

Moreover, for evaluating the impact of image noise, Gaussian noise comparable to that found in the experimental data (i.e., SNR of 80) was added to the signal intensities, which were then used to compute the scalar DTI parameters, including D_1, D_2, D_3, and FA, of the fibrotic myocardium. In this fashion, DTI parameters under fast and slow compartmental exchange were separately obtained 1000 times and averaged for each level of collagen content (i.e., f) over the range seen in the current study (4% to 32%).

To compare the simulation results to experimental data, the slopes of the simulated DTI profiles (D_1, D_2, D_3, and FA) as a function of collagen content were obtained, and compared to the slope of the linear regression line obtained from the experimental data.

Slopes were normalized to units of percentage change per unit of collagen fraction percentage, with the average collagen percentage of the control group taken as the baseline.

3.4 Results

3.4.1 DTI

The quantified and ROI-averaged values of the DTI parameters for the normal control and HF groups are detailed in Table 3.2. Consistent with the qualitative observations, the FA in HF specimens was on average 22% lower than normal specimens (0.21 ± 0.01 vs. 0.27 ± 0.02). In contrast, MD of the HF specimens was 12% higher than normal samples (0.76 ± 0.02 vs. 0.68 ± 0.01 $\times 10^{-3}$ mm^2/s). MR images and DTI-derived FA and MD maps obtained from a-representative normal and HF myocardial samples are shown in Fig. 3.1. Qualitatively, compared to the normal control, lower FA and higher diffusivities were observed in the failing myocardium. Together, the trends of MD and FA suggest that water motility is both higher and less anisotropic in HF than normal myocardial tissues.

Table 3.2. DTI and quantitative collagen measurements obtained from control and failing hearts. FA (fractional anisotropy), MD (mean diffusivity), D_1 (primary diffusivity), D_2 (secondary diffusivity), and D_3 (tertiary diffusivity). DTI and collagen measurements were obtained from ROIs covering the whole imaged tissue area.

	FA	MD 10^{-3} mm^2/s	D_1 10^{-3} mm^2/s	D_2 10^{-3} mm^2/s	D_3 10^{-3} mm^2/s	Collagen (%)
Control (n=5)	0.27±0.02	0.68±0.01	0.88±0.02	0.64±0.01	0.51±0.02	7.1±1.1
Failing (n=14)	0.21±0.01	0.76±0.02	0.93±0.02	0.73±0.02	0.63±0.02	19.4±2.0
P	<0.01	<0.01	0.13	<0.01	<0.01	<0.01
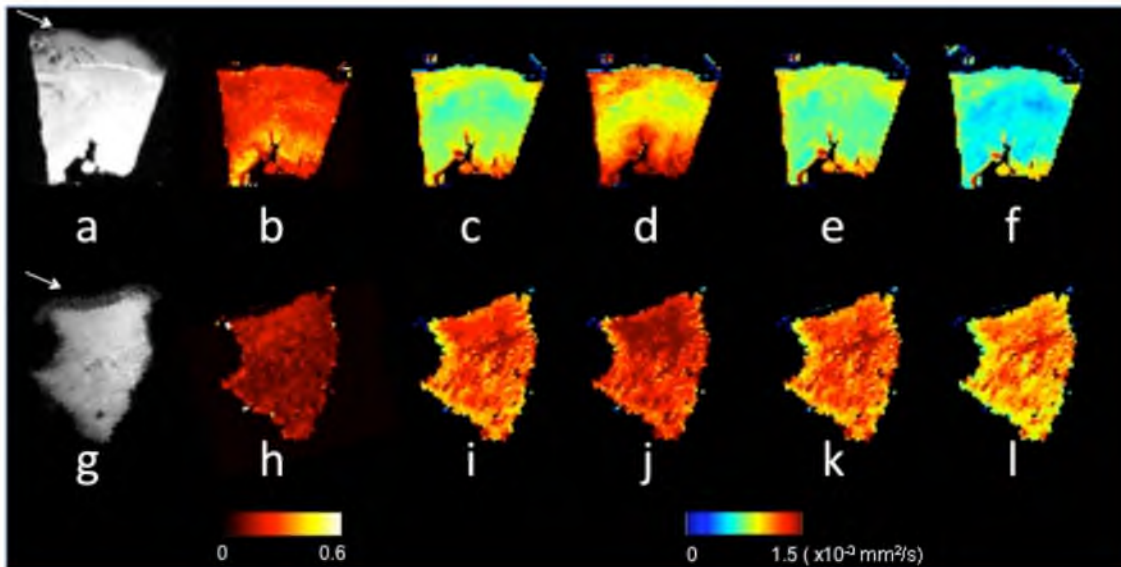
Figure 3.1. Representative DTI scalar maps from control and failing heart cores. The top panel shows a MR image without diffusion weighting (B0), FA, MD, D_1, D_2, and D_3 maps for normal (a-f), whereas the lower panel shows the failing core (g-l). A transverse view is shown, with the endocardium located at the top. The pericardial fat visible in the B0 image (white arrows in a and g) was segmented out in the DTI processing step. The DTI parameters are shown in falsecolor according to the colorbars, and all diffusivities had the same color scaling with units of 10^{-3} mm^2/s.

3.4.2 Collagen Evaluation and DTI-Histology Correlation

Representative trichrome sections from control and HF myocardial samples are shown in Fig. 3.2. Compared to the control specimen (Fig. 3.2a), the HF slide (Fig. 3.2b) contains conspicuously higher content of the blue-staining interstitial collagen. Quantitative collagen content measurements are summarized in Table 3.2. The total collagen content, used as the metric of fibrosis, is nearly 3 times higher in HF than in normal myocardium (19.4 ± 2.0 versus 7.1 ± 1.1 percent area). The level of collagen intrinsic in the normal myocardium is in agreement with the ~4-5% reported by a previous study [34]. The relationships between different DTI parameters and the total collagen content are shown as scatter plots in Fig. 3.3. Qualitatively, from the scatter of the data points around the fitted lines, there appears to be more variability in D_1 and FA,

a   b
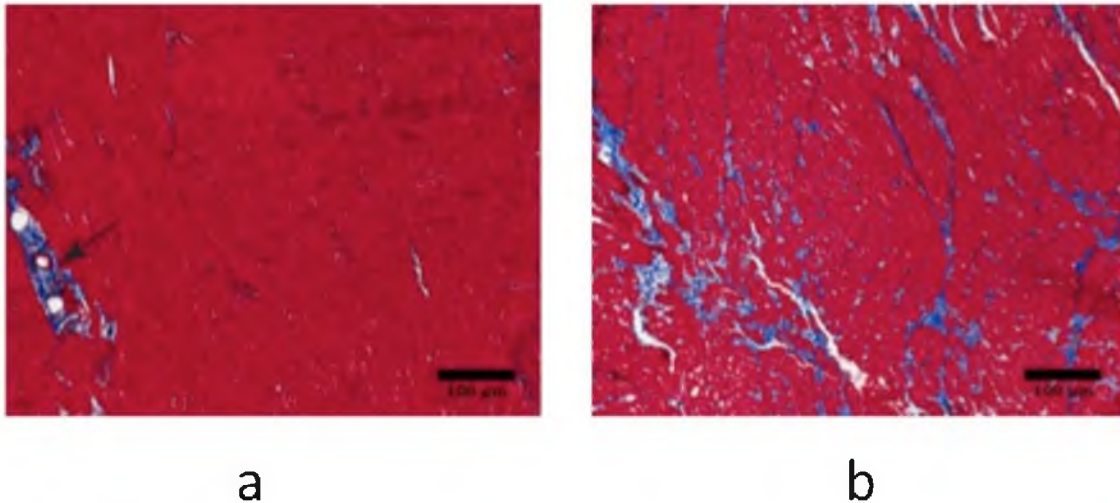
Figure 3.2. Histological evaluation of control and failing heart cores. Masson's trichrome histological images of collagen content (20x magnification, collagen stains in blue) from a representative control (a) and failing (b) heart cores. The black arrow in (a) points to perivascular collagen, which was included as part of the total collagen calculation reported in this study.

compared to D_2 and D_3. The observation is consistent with the Pearson's correlation coefficients between individual DTI parameters and total collagen content, which are listed in Table 3.3. Among the pairings examined, significant correlations were found between the collagen content (or fibrosis) and FA ($r = -0.51$), MD (0.59), D_2 (0.56), and D_3 (0.62). The correlation between D_1 and collagen was relatively weaker ($r = 0.46$), and was not significant ($P = 0.05$).

3.4.3 Computational Compartmental Analysis

Plots of the Monte Carlo simulated DTI scalar parameters (D_1, D_2, D_3, and FA) vs. collagen percentages are shown in Fig. 3.4. Overall, simulation results obtained using fast and slow exchange models were in close agreement with the experimental data regression line. Both exchange models indicate that all DTI diffusivities would increase, whereas the FA would decrease, as the percent collagen content is increased.
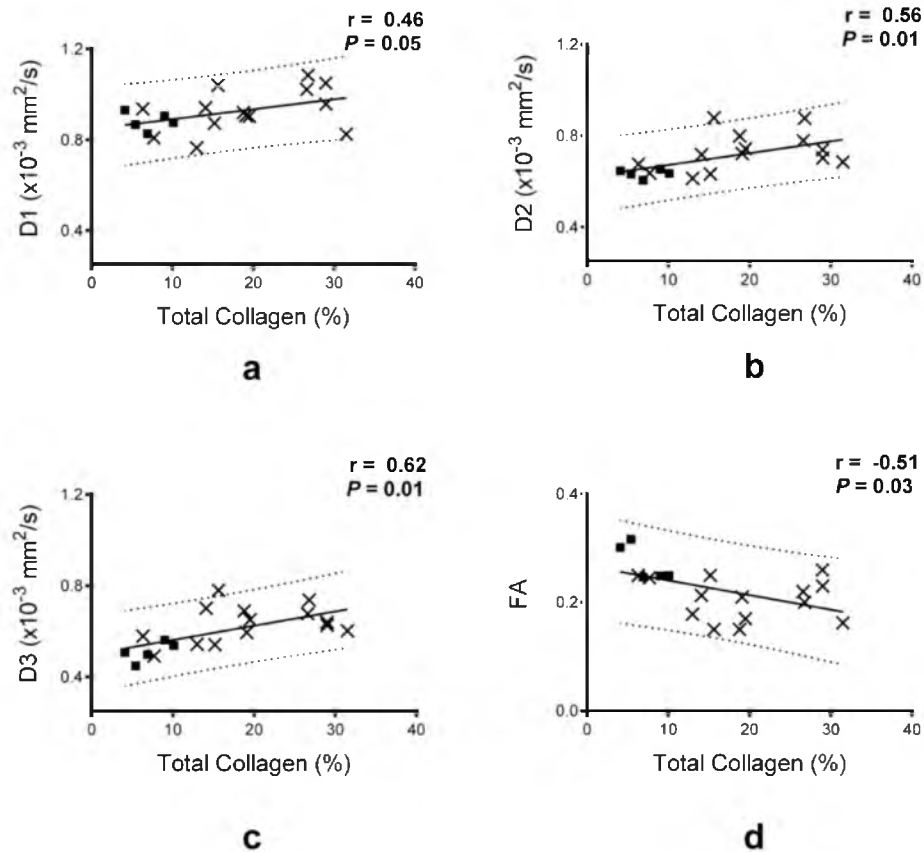
Figure 3.3 Quantitative correlation between DTI scalar parameters and collagen content. Scatter plots of FA, D_1, D_2 and D_3 as a function of collagen content are shown with the experimental data (displayed as x) and the linear regression fit (solid black line) and the 95% prediction interval (dashed lines). The linear regression coefficient (r) and its corresponding P value are reported with each plot.

Table 3.3 Pearson's correlation coefficient (r) and P-values between DTI scalar parameters and total collagen. FA (fractional anisotropy), MD (mean diffusivity), D_1 (primary diffusivity), D_2 (secondary diffusivity), D_3 (tertiary diffusivity).

	FA	MD	D_1	D_2	D_3
r-value	− 0.51	0.59	0.46	0.56	0.62
P-value	<0.05	<0.02	0.05	<0.02	<0.01
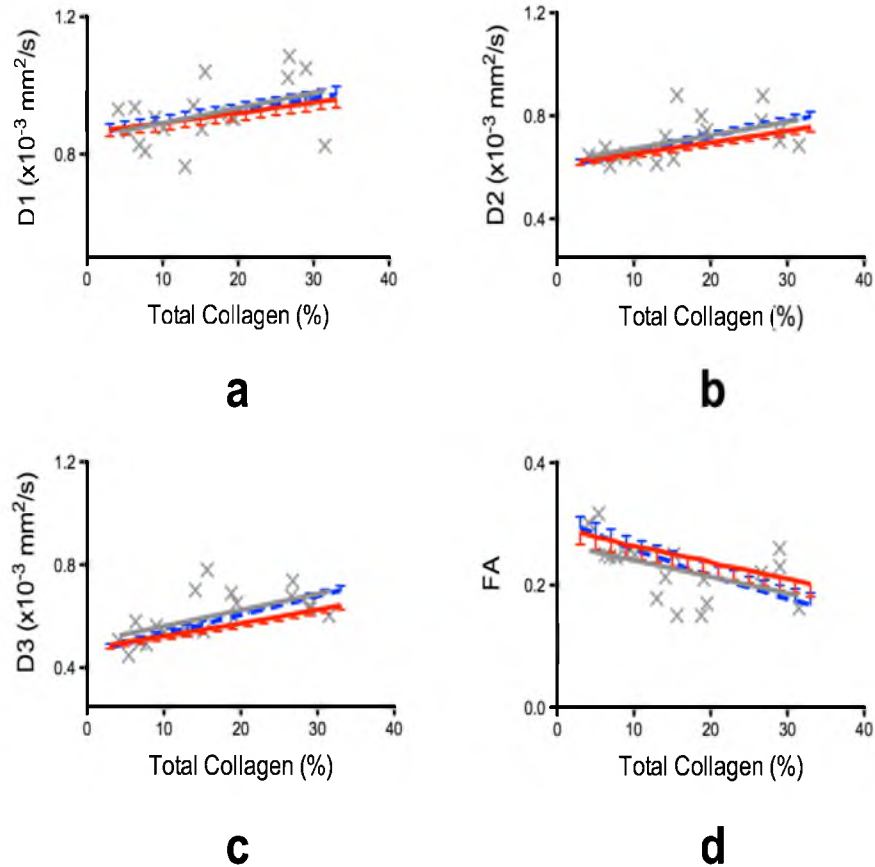
Figure 3.4. Monte Carlo computer simulation of DTI scalar parameters as function of collagen content (%). The standard DTI measurements were simulated when the underlying diffusion signal was assumed to originate from either fast (dotted blue line) or slow (solid red line) exchange between the two compartments. The experimental data and their regression fit line are overlaid on each plot in gray (x for individual measurements, and solid gray line for the linear regression fit). Little difference was seen between fast and slow exchange model predictions compared to the variability observed in the experimental data.

Moreover, simulations indicate that the rate of increase as function of collagen content in the secondary and tertiary diffusivities is at least twice as large as that of the primary diffusivity. Specifically, the average collagen content change seen in the current study (Table 3.2) between normal (baseline) and HF myocardium, 7% to 19%, would correspond to normalized slopes of 0.39, 0.87, and 1.3 for D_1, D_2, and D_3, respectively, and -1.13 for FA (unit of normalized slope is % change per unit of collagen fraction

percentage). In comparison, the corresponding quantities from experimental data are 0.51, 0.79, 1.15, and -1.08 for D_1, D_2, D_3, and FA, respectively. Considering the simplifying assumptions used in the exchange models, both the trends as well as the magnitudes of the simulated DTI parameter changes are in strong agreement with the experimental measurements.

3.5 Discussion

In this study, DTI was performed on left ventricular specimens obtained from patients with chronic end-stage HF due to idiopathic dilated cardiomyopathy at the time of left ventricular assist device implantation and from normal hearts. Results indicate that HF leads to both significant decrease in the degree of anisotropy (i.e., FA) and significant increase in the water diffusivity (MD, D_2, and D_3) of the myocardium.

The trends of the observed changes are consistent with previous DTI studies of myocardial diseases. For example, reduction in the FA and the increase in diffusivities have been reported in studies on myocardial ischemic injury [25], [26] and dilated cardiomyopathy [29]. Similarly, the FA has been observed to decrease in a DTI study of hypertrophic cardiomyopathy [28]. Histological measurements reveal that HF also leads to significant increase in myocardial collagen content (i.e., fibrosis), which is a hallmark of HF [10].

Histological validation of DTI fiber orientation mapping in the myocardium has been extensively reported in normal hearts [13]–[15] and, to a lesser extent, in diseased hearts [25], [29]. In contrast, few studies have correlated the DTI scalar parameters with histology, and when examined, the correlation was qualitative [29]. The present study is the first to demonstrate that scalar DTI parameters are directly correlated to histology, as

shown in Table 3.3 and Fig. 3.3. Whereas the FA reduction or MD increase associated with HF and their correlation to tissue fibrosis are expected, a noteworthy observation in the current study is that the secondary (D_2) and tertiary (D_3) DTI eigenvalues exhibit a higher correlation with the degree of fibrosis than the primary diffusivity D_1 ($r = 0.56$ and 0.62, respectively, compared to 0.46). These findings point out a potential role of the indices for characterizing myocardial pathology, and may provide clues to model the effect of fibrosis on the observed DTI signal in the myocardium.

Analysis of the numerical simulations reveals that the behavior of the scalar DTI parameters as a function of the collagen content, including the different sensitivities (i.e., magnitude of the slope) among the diffusivities and FA, can be readily explained by exchange between myocardial and collagen compartments. Moreover, the fact that little difference is seen between simulations using fast and slow exchange models suggests that the behaviors of the scalar DTI parameters largely depend on the mere presence of collagen, with little or no influence from the type of underlying mechanism of compartmental exchange. The practical implication of the finding is that the DTI scalar parameters, at least those obtained using similar acquisition protocols, can be used as direct indices of the tissue collagen content.

The key assumptions made in the numerical compartmental analysis were that the diffusion in the fibrous myocardial compartment is isotropic (i.e., FA = 0) and the intrinsic collagen fraction (f_0) in the normal myocardium in Eq. 3.1 is 7%. Although the first assumption is valid when collagen fibers in the compartment are oriented randomly, or when the collagen is organized but points in a random direction with respect to the myofibers, it would be invalid if the organized collagen follows the same orientation as

the myofibers. If the latter had been the case, the simulations would predict the FA of the HF myocardium as a function of collagen content under both fast and slow exchange models to have shallower slopes and deviate away from experimental data points. Consequently, the high degree of agreement between the simulation and empirical results indicate that the assumption of zero FA for the fibrous compartment used in the exchange analysis is valid. Second, the parameter sensitivity analysis suggests that the estimated diffusivities obtained from both exchange models are relatively insensitive to the choice of f_0.

Despite the large bulk motion of the heart during the cardiac cycle, *in vivo* cardiac DTI has been shown to be both feasible and reproducible in clinical patients [22], [23], [48–50]. Our study paves the way for *in vivo* clinical trials to evaluate the ability of DTI to assess diffuse fibrosis *in vivo*. Furthermore, DTI can complement other MRI techniques to characterize myocardial fibrosis in diseased hearts. For example, post-contrast T1 mapping has been used as a tool to quantify diffuse fibrosis [51]. However, there has been some concern about the use of gadopentate dimeglumine agents in patients with renal failure [52]. Hence, it is desirable to explore alternative mechanisms of MRI contrast, especially mechanisms that do not rely on exogenous contrast agents. In this regard, DTI may be an alternative or adjunct method to T1 mapping for the detection and quantification of diffuse fibrosis. Although the observed correlation between DTI and fibrosis is modest, the strength of correlation was similar to that reported in initial T1 mapping studies [51]. Recent advances in T1 mapping studies have incorporated modeling of the extracellular volume fraction via the relaxation difference between pre- and post-gadolinium contrast administration, which has been shown to improve the

quantification of diffuse fibrosis [53], [54].

In order to improve the accuracy of DTI for the quantification of diffuse fibrosis, other factors that may affect the DTI measurements must be taken into account, such as edema, fiber disarray and age effects. Edema was detected using T2 mapping in patients with dilated cardiomyopathy [55]. In a recent study of ischemic reperfusion injury in mice, edema was associated with reduced FA and increased MD [56]. Edema was not monitored directly in the current study, and care should be taken in future *in vivo* DTI studies to rule out the presence of edema. Fiber disarray is another factor that has been shown to reduce FA but not MD [30], and therefore must be accounted for when performing cardiac DTI. Finally, aging hearts have been shown to undergo remodeling processes that impact their mechanical and electrical properties [57]. Aging hearts have been shown to be slightly more fibrotic (with the mean fibrosis area being 5% in young hearts versus 11% in aging hearts) and stiffer when compared with younger hearts [57]. Thus, future studies validating DTI to measure diffuse fibrosis should also control for age in the studied population.

There are a few other caveats that need to be taken into account in interpreting the results of the current study. First, due to logistical constraints, the sample sizes of the study, 14 for HF and 5 for normal myocardial specimens, are relatively small, which may have prevented some of the observed differences (e.g., D_1) or correlations (D_1 vs. collagen content) from reaching statistical significance. However, the significant differences detected and the smaller variability shown by the DTI parameters (as indicated by the SEM values in Table 3.2) may actually point to a potential advantage of DTI – that the technique is useful for characterizing the heart microstructure. Finally, the

current study was conducted on fixed excised specimens, and the findings may or may not be the same as those observed from *in vivo* cardiac DTI. However, since both HF and control samples were fixed, regardless of the impact of fixation on the DTI parameters, the differences observed between the groups likely reflected the additional effects introduced by the disease. Moreover, the DTI observations were correlated to histological measurements, which in both the current and other studies were also performed on fixed samples and generally taken to be the gold standard.

In conclusion, the present study suggests that DTI scalar parameters can complement conventional histology and T1-mapping for quantifying diffuse fibrosis. Given the recent technical advances and increasing interest of *in vivo* cardiac DTI [45]–[48], these findings are timely and point to a potential role for DTI in evaluating the tissue collagen content in nonischemic diseased hearts.

3.6 References

1. Roger VL, Go AS, Lloyd-Jones DM, Adams RJ, Berry JD, Brown TM, Carnethon MR, Dai S, de Simone G, Ford ES, Fox CS, Fullerton HJ, Gillespie C, Greenlund KJ, Hailpern SM, Heit J a, Ho PM, Howard VJ, Kissela BM, Kittner SJ, Lackland DT, Lichtman JH, Lisabeth LD, Makuc DM, Marcus GM, Marelli A, Matchar DB, McDermott MM, Meigs JB, Moy CS, Mozaffarian D, Mussolino ME, Nichol G, Paynter NP, Rosamond WD, Sorlie PD, Stafford RS, Turan TN, Turner MB, Wong ND, Wylie-Rosett J. Heart disease and stroke statistics--2011 update: a report from the American Heart Association. *Circulation.* 2011;123(4):e18–209.

2. Dickstein K, Cohen-Solal A, Filippatos G, McMurray JJ V, Ponikowski P, Poole-Wilson PA, Strömberg A, van Veldhuisen DJ, Atar D, Hoes AW, Keren A, Mebazaa A, Nieminen M, Priori SG, Swedberg K, Vahanian A, Camm J, De Caterina R, Dean V, Funck-Brentano C, Hellemans I, Kristensen SD, McGregor K, Sechtem U, Silber S, Tendera M, Widimsky P, Zamorano JL, Auricchio A, Bax J, Böhm M, Corrà U, Della Bella P, Elliott PM, Follath F, Gheorghiade M, Hasin Y, Hernborg A, Jaarsma T, Komajda M, Kornowski R, Piepoli M, Prendergast B, Tavazzi L, Vachiery J-L, Verheugt FW a, Zannad F. ESC guidelines for the diagnosis and treatment of acute and chronic heart failure 2008. *Eur Heart J.* 2008;29(19):2388–442.

3. Mann DL, Bristow MR. Mechanisms and models in heart failure: the biomechanical model and beyond. *Circulation*. 2005;111(21):2837–49.

4. Tamaki S, Mano T, Sakata Y, Ohtani T, Takeda Y, Kamimura D, Omori Y, Tsukamoto Y, Ikeya Y, Kawai M, Kumanogoh A, Hagihara K, Ishii R, Higashimori M, Kaneko M, Hasuwa H, Miwa T, Yamamoto K, Komuro I. Interleukin-16 promotes cardiac fibrosis and myocardial stiffening in heart failure with preserved ejection fraction. *PLoS One*. 2013;8(7):e68893.

5. Ten Tusscher KHWJ, Panfilov A V. Influence of diffuse fibrosis on wave propagation in human ventricular tissue. *Europace*. 2007;9 Suppl 6:vi38–45.

6. Bohl S, Schulz-Menger J. Cardiovascular magnetic resonance imaging of non-ischaemic heart disease: established and emerging applications. *Heart Lung Circ. Australasian Society of Cardiac and Thoracic Surgeons and The Cardiac Society of Australia and New Zealand;* 2010;19(3):117–32.

7. Jellis C, Martin J, Narula J, Marwick TH. Assessment of nonischemic myocardial fibrosis. *J Am Coll Cardiol. Elsevier Inc.;* 2010;56(2):89–97.

8. Weber KT, Brilla CG. Pathological hypertrophy and cardiac interstitium. Fibrosis and renin- angiotensin-aldosterone system. *Circulation*. 1991;83(6):1849–65.

9. Beltrami C a., Finato N, Rocco M, Feruglio G a., Puricelli C, Cigola E, Quaini F, Sonnenblick EH, Olivetti G, Anversa P. Structural basis of end-stage failure in ischemic cardiomyopathy in humans. *Circulation*. 1994;89(1):151–63.

10. Drakos SG, Kfoury AG, Stehlik J, Selzman CH, Reid BB, Terrovitis J V, Nanas JN, Li DY. Bridge to recovery: understanding the disconnect between clinical and biological outcomes. *Circulation*. 2012;126(2):230–41.

11. Diez J. Losartan-Dependent Regression of Myocardial Fibrosis Is Associated With Reduction of Left Ventricular Chamber Stiffness in Hypertensive Patients. *Circulation*. 2002;105(21):2512–7.

12. Basser PJ, Mattiello J, LeBihan D. MR diffusion tensor spectroscopy and imaging. *Biophys J*. 1994;66(1):259–67.

13. Hsu EW, Muzikant AL, Matulevicius SA, Penland RC, Henriquez CS. Magnetic resonance myocardial fiber-orientation mapping with direct histological correlation. *Am J Physiol Hear Circ Physiol*. 1998;274(5 Pt 2):H1627–34.

14. Scollan DF, Holmes A, Winslow R, Forder J. Histological validation of myocardial microstructure obtained from diffusion tensor magnetic resonance imaging. *Am J Physiol Hear Circ Physiol*. 1998;275(6 Pt 2):H2308–18.

15. Holmes A, Scollan DF, Winslow RL. Direct histological validation of diffusion tensor MRI in formaldehyde-fixed myocardium. *Magn Reson Med.* 2000;44(1):157–61.

16. Tseng W-YI, Wedeen VJ, Reese TG, Smith RN, Halpern EF. Diffusion tensor MRI of myocardial fibers and sheets: correspondence with visible cut-face texture. *J Magn Reson Imaging.* 2003;17(1):31–42.

17. Jiang Y, Pandya K, Smithies O, Hsu EW. Three-dimensional diffusion tensor microscopy of fixed mouse hearts. *Magn Reson Med.* 2004;52(3):453–60.

18. Jiang Y, Guccione JM, Ratcliffe MB, Hsu EW. Transmural heterogeneity of diffusion anisotropy in the sheep myocardium characterized by MR diffusion tensor imaging. *Am J Physiol Hear Circ Physiol.* 2007;293(4):H2377–84.

19. Healy LJ, Jiang Y, Hsu EW. Quantitative comparison of myocardial fiber structure between mice, rabbit, and sheep using diffusion tensor cardiovascular magnetic resonance. *J Cardiovasc Magn Reson.* 2011;13:74.

20. Geerts L, Bovendeerd P, Nicolay K, Arts T. Characterization of the normal cardiac myofiber field in goat measured with MR-diffusion tensor imaging. *Am J Physiol Heart Circ Physiol.* 2002;283(1):H139–45.

21. Chen J, Liu W, Zhang H, Lacy L, Yang X, Song S-K, Wickline S a, Yu X. Regional ventricular wall thickening reflects changes in cardiac fiber and sheet structure during contraction: quantification with diffusion tensor MRI. *Am J Physiol Hear Circ Physiol.* 2005;289(5):H1898–907.

22. Reese TG, Weisskoff RM, Smith RN, Rosen BR, Dinsmore RE, Wedeen VJ. Imaging myocardial fiber architecture *in vivo* with magnetic resonance. *Magn Reson Med.* 1995;34(6):786–91.

23. Dou J, Reese TG, Tseng W-YI, Wedeen VJ. Cardiac diffusion MRI without motion effects. *Magn Reson Med.* 2002;48(1):105–14.

24. Wu M, Tseng W-YI, Su MM, Liu C, Chiou K-R, Wedeen VJ, Reese TG, Yang C-F. Diffusion tensor magnetic resonance imaging mapping the fiber architecture remodeling in human myocardium after infarction: correlation with viability and wall motion. *Circulation.* 2006;114(10):1036–45.

25. Wu M-T, Su M-YM, Huang Y-L, Chiou K-R, Yang P, Pan H-B, Reese TG, Wedeen VJ, Tseng W-YI. Sequential changes of myocardial microstructure in patients postmyocardial infarction by diffusion-tensor cardiac MR: correlation with left ventricular structure and function. *Circ Cardiovasc Imaging.* 2009;2(1):32–40.

26. Chen J, Song S-K, Liu W, McLean M, Allen JS, Tan J, Wickline S a, Yu X. Remodeling of cardiac fiber structure after infarction in rats quantified with diffusion tensor MRI. *Am J Physiol Hear Circ Physiol*. 2003;285(3):H946–54.

27. Wu Y, Wu EX. MR investigation of the coupling between myocardial fiber architecture and cardiac contraction. *Conf Proc IEEE Eng Med Biol Soc*. 2009;2009:4395–8.

28. Pop M, Ghugre NR, Ramanan V, Morikawa L, Stanisz G, Dick AJ, Wright G a. Quantification of fibrosis in infarcted swine hearts by *ex vivo* late gadolinium-enhancement and diffusion-weighted MRI methods. *Phys Med Biol*. 2013;58(15):5009–28.

29. Helm PA, Younes L, Beg MF, Ennis DB, Leclercq C, Faris OP, McVeigh E, Kass D, Miller MI, Winslow RL. Evidence of structural remodeling in the dyssynchronous failing heart. *Circ Res*. 2006;98(1):125–32.

30. Tseng W-YI, Dou J, Reese TG, Wedeen VJ. Imaging myocardial fiber disarray and intramural strain hypokinesis in hypertrophic cardiomyopathy with MRI. *J Magn Reson Imaging*. 2006;23(1):1–8.

31. Eggen MD, Swingen CM, Iaizzo PA. Analysis of fiber orientation in normal and failing human hearts using diffusion tensor MRI. EEE International Symposium on Biomedical Imaging: From Nano to Macro. *Ieee;* 2009. p. 642–5.

32. Li W, Lu M, Banerjee S, Zhong J, Ye A, Molter J, Yu X. *Ex vivo* diffusion tensor MRI reflects microscopic structural remodeling associated with aging and disease progression in normal and cardiomyopathic Syrian hamsters. *NMR Biomed*. 2009;22(8):819–25.

33. McConnell HM. Reaction Rates by Nuclear Magnetic Resonance. *J Chem Phys*. 1958;28(3):430.

34. Kärger J. NMR self-diffusion studies in heterogeneous systems. *Adv Colloid Interface Sci*. 1985;23(0):129–48.

35. Forder JR, Bui JD, Buckley DL, Blackband SJ. MR imaging measurement of compartmental water diffusion in perfused heart slices. *Am J Physiol Hear Circ Physiol*. 2001;281:H1280–5.

36. Hsu EW, Buckley DL, Bui JD, Blackband SJ, Forder JR. Two-component diffusion tensor MRI of isolated perfused hearts. *Magn Reson Med*. 2001;45(6):1039–45.

37. Drakos SG, Kfoury AG, Hammond EH, Reid BB, Revelo MP, Rasmusson BY, Whitehead KJ, Salama ME, Selzman CH, Stehlik J, Clayson SE, Bristow MR,

Renlund DG, Li DY. Impact of mechanical unloading on microvasculature and associated central remodeling features of the failing human heart. *J Am Coll Cardiol. Elsevier Inc.;* 2010;56(5):382–91.

38.   Kim TH, Zollinger L, Shi XF, Rose J, Jeong E-K. Diffusion tensor imaging of *ex vivo* cervical spinal cord specimens: the immediate and long-term effects of fixation on diffusivity. *Anat Rec.* 2009;292(2):234–41.

39.   Watson B, Hsu E. Effects of Formalin Fixation on Diffusion Tensor Imaging of Myocardial Tissues. Proceedings of the 20th Annual Meeting of ISMRM, Melbourne Australia. 2012. p. 1114.

40.   Unverferth D V., Fetters JK, Unverferth BJ, Leier C V., Magorien RD, Arn a. R, Baker PB. Human myocardial histologic characteristics in congestive heart failure. *Circulation.* 1983;68(6):1194–200.

41.   Papadakis NG, Xing D, Huang CL, Hall LD, Carpenter T a. A comparative study of acquisition schemes for diffusion tensor imaging using MRI. *J Magn Reson.* 1999;137(1):67–82.

42.   Le Bihan D, Mangin JF, Poupon C, Clark C a, Pappata S, Molko N, Chabriat H. Diffusion tensor imaging: concepts and applications. *J Magn Reson Imaging.* 2001;13(4):534–46.

43.   Niendorf T, Dijkhuizen RM, Norris DG, van Lookeren Campagne M, Nicolay K. Biexponential diffusion attenuation in various states of brain tissue: implications for diffusion-weighted imaging. *Magn Reson Med.* 1996;36(6):847–57.

44.   Henkelman RM, Stanisz GJ, Kim JK, Bronskill MJ. Anisotropy of NMR properties of tissues. *Magn Reson Med.* 1994;32(5):592–601.

45.   Hsu EW, Setton LA. Diffusion tensor microscopy of the intervertebral disc anulus fibrosus. *Magn Reson Med.* 1999;41(5):992–9.

46.   de Visser SK, Bowden JC, Wentrup-Byrne E, Rintoul L, Bostrom T, Pope JM, Momot KI. Anisotropy of collagen fibre alignment in bovine cartilage: comparison of polarised light microscopy and spatially resolved diffusion-tensor measurements. *Osteoarthritis Cartilage.* 2008;16(6):689–97.

47.   Wu EX, Wu Y, Nicholls JM, Wang J, Liao S, Zhu S, Lau C-P, Tse H-F. MR diffusion tensor imaging study of postinfarct myocardium structural remodeling in a porcine model. *Magn Reson Med.* 2007;58(4):687–95.

48.   Gamper U, Boesiger P, Kozerke S. Diffusion imaging of the *in vivo* heart using spin echoes-considerations on bulk motion sensitivity. *Magn Reson Med.* 2007;57(2):331–7.

49. McGill L-A, Ismail TF, Nielles-Vallespin S, Ferreira P, Scott AD, Roughton M, Kilner PJ, Ho SY, McCarthy KP, Gatehouse PD, de Silva R, Speier P, Feiweier T, Mekkaoui C, Sosnovik DE, Prasad SK, Firmin DN, Pennell DJ. Reproducibility of *in vivo* diffusion tensor cardiovascular magnetic resonance in hypertrophic cardiomyopathy. *J Cardiovasc Magn Reson.* 2012;14(1):86.

50. Nielles-Vallespin S, Mekkaoui C, Gatehouse P, Reese TG, Keegan J, Ferreira PF, Collins S, Speier P, Feiweier T, de Silva R, Jackowski MP, Pennell DJ, Sosnovik DE, Firmin D. *In vivo* diffusion tensor MRI of the human heart: Reproducibility of breath-hold and navigator-based approaches. *Magn Reson Med.* 2012;70(2):454–65.

51. Iles L, Pfluger H, Phrommintikul A, Cherayath J, Aksit P, Gupta SN, Kaye DM, Taylor AJ. Evaluation of diffuse myocardial fibrosis in heart failure with cardiac magnetic resonance contrast-enhanced T1 mapping. *J Am Coll Cardiol.* 2008;52(19):1574–80.

52. Marckmann P, Skov L, Rossen K, Dupont A, Damholt MB, Heaf JG, Thomsen HS. Nephrogenic systemic fibrosis: suspected causative role of gadodiamide used for contrast-enhanced magnetic resonance imaging. *J Am Soc Nephrol.* 2006;17(9):2359–62.

53. Messroghli D, Nordmeyer S, Dietrich T, Dirsch O, Kaschina E, Savvatis K, O H-Ici D, Klein C, Berger F, Kuehne T. Assessment of Diffuse Myocardial Fibrosis in Rats Using Small Animal Look-Locker Inversion Recovery (SALLI) T1 Mapping. *Circ Cardiovasc Imaging.* 2011;4(6):636–40.

54. Flett AS, Hayward MP, Ashworth MT, Hansen MS, Taylor AM, Elliott PM, McGregor C, Moon JC. Equilibrium contrast cardiovascular magnetic resonance for the measurement of diffuse myocardial fibrosis: preliminary validation in humans. *Circulation.* 2010;122(2):138–44.

55. Nishii T, Kono A, Shigeru M, Takamine S, Fujiwara S, Kyotani K, Aoyama N, Sugimura K. Cardiovascular magnetic resonance T2 mapping can detect myocardial edema in idiopathic dilated cardiomyopathy. *Int J Cardiovasc Imaging. Springer Netherlands;* 2014;1–8.

56. Sosnovik DE, Mekkaoui C, Huang S, Chen HH, Dai G, Stoeck CT, Ngoy S, Guan J, Wang R, Kostis WJ, Jackowski MP, Wedeen VJ, Kozerke S, Liao R. Microstructural Impact of Ischemia and Bone Marrow-Derived Cell Therapy Revealed with Diffusion Tensor MRI Tractography of the Heart *In vivo. Circulation.* 2014;129(17):1731–41.

57. Cooper LL, Odening KE, Hwang M-S, Chaves L, Schofield L, Taylor C a, Gemignani AS, Mitchell GF, Forder JR, Choi B-R, Koren G. Electromechanical

and structural alterations in the aging rabbit heart and aorta. *Am J Physiol Heart Circ Physiol*. 2012;302(8):H1625–35.

CHAPTER 4

ORIENTATION DEPENDENCE OF MICROCIRCULATION-INDUCED DIFFUSION

SIGNAL IN ANISOTROPIC TISSUES[1]

4.1 Abstract

The purpose of this work is to seek a better understanding of the effect of

organized capillary flow on the MR diffusion-weighted signal. A theoretical framework

was proposed to describe the diffusion-weighted MR signal, which was then validated

both numerically using a realistic model of capillary network and experimentally in an

animal model of isolated perfused heart preparation with myocardial blood flow verified

via direct arterial spin labeling measurements. Results shows that microcirculation in

organized tissues gave rise to an MR signal that could be described as a combination of

the bi-exponential behavior of conventional intravoxel incoherent motion (IVIM) theory

and DTI-like anisotropy of the vascular signal, with the flow-related pseudo diffusivity

represented as the linear algebraic product between the encoding directional unit vector

and an appropriate tensor entity. Very good agreement between theoretical predictions

and both numerical and experimental observations was found. In conclusion, these

findings suggest that the DTI formalism of anisotropic spin motion can be incorporated into the classical IVIM theory to describe the MR signal arising from diffusion and microcirculation in organized tissues.

4.2 Introduction

The MR signal in the presence of a magnetic field gradient is highly sensitive to the aggregate translational molecular motion of water, which in turn is heavily influenced by the microstructure or microcirculation of the tissue [1], [2]. For example, cell swelling in acute brain ischemia causes hyperintensity in diffusion-weighted imaging (DWI) [3]. The same diffusion contrast exhibits anisotropy in ordered tissues such as brain white matter and myocardium, which can be characterized via diffusion tensor imaging (DTI) [4]. Further, for highly vascularized tissues, diffusion-like contrast induced by microcirculation has been used as a means to characterize perfusion [5], [6].

In general, the diffusion signal can be described as the statistical average of phase dispersion associated with spin displacements. For isotropic systems with Gaussian-distributed Brownian motion, the signal is an exponentially decaying function of the spin motility and the encoding b-value. The same behavior also applies to ordered tissues, except the rate of signal decay depends also on the relative direction of the encoding gradient. In heterogeneous systems that contain spin populations with different motility, depending on the rate of compartmental exchange, the signal is modeled as either a single exponential function with weighted decay constant or superposition of separate exponential functions, in the so-called fast or slow-exchange approximations, respectively [7]–[9].

Since blood flow in capillaries also results in translational dispersion of water

molecules, theories such as the intravoxel incoherent motion (IVIM) have been proposed for characterizing microcirculation using similar diffusion-weighted imaging methodology [5], [6]. A key assumption in IVIM theory is that the capillary network consists of identical but randomly oriented straight segments, with blood changing segments rapidly while transiting through the network. In tissues, the MR signal is usually modeled as a bi-exponential function to separate the slower extravascular diffusion from the faster flow-mediated component, whose decay constant is referred to as the pseudo diffusion coefficient (D^*). Because of the assumption of random capillary orientation, it is unclear whether the classical IVIM theory can be directly applied to ordered tissues such as the myocardium where the capillary network is both organized and oriented mostly parallel to the myofibers [9]–[12]. A study using IVIM to explain diffusion signals from hearts *in vivo* reported different vascular compartment sizes for different encoding directions with respect to the myofiber orientation [13].

Theories that incorporate partially coherent microcirculation, namely intravoxel partially coherent motion (IVPCM), have been proposed and used to characterize flow and diffusion in the skeletal muscle [14]. The IVPCM model also predicted that organized flow would manifest as different observed vascular volume fraction (VF) along different encoding directions, while D^* would remain isotropic. These predictions are somewhat counterintuitive, because VF is a scalar parameter reflecting the physical compartmental sizes, which should be independent of the means of observation. Moreover, since D^* reflects the spin translational dispersion, an anisotropic D^* is more likely when the underlying spin motion is nonrandom. Clearly, unlike DWI and DTI in ordered tissues, the relationship between IVIM and microcirculation-mediated diffusion

signal and organized capillary networks is not completely understood.

The overall aim of the current work is to seek a better understanding of the microcirculation-induced MR signal in organized tissues. In the ensuing sections, a theoretical framework is proposed to describe the MR signal, which is then validated both numerically using a realistic model of capillary network and experimentally using an animal isolated perfused heart preparation [15] with myocardial blood flow verified via direct arterial spin labeling (ASL) measurements [16]. For consistency, whenever possible the notation and convention of classical IVIM theory are followed in the theoretical formulation and analysis of the observed MR signal.

4.3 Theory

4.3.1 Effects of Flow in Single and Multiple Tubes

The effects of constant-velocity flow in single straight tubes on the MR signal has long been characterized [17]–[19]. For "plug" flow, e.g., when red blood cells are transiting through capillaries [20], the fluid moves with uniform velocity and generates a constant phase shift. Writing as a modulation factor F, the phase shift arising from flow with average velocity $\mathbf{v_0}$, subject to an encoding gradient $\mathbf{g}(t)$ with first moment $\mathbf{m_1} = \int_0^{TE} t\mathbf{g}(t)\, dt$, is given by

$$F_{single-plug} = \exp(-i\,\gamma\,\mathbf{m_1} \cdot \mathbf{v_0}). \tag{4.1}$$

In contrast, flow of a fluid without red blood cells in a similar tube is laminar [64], characterized by an inverted parabolic radial velocity profile. The heterogeneous flow creates phase dispersion that results in attenuation of the signal modulation,

$$F_{single-laminar} = \text{sinc}(\gamma\,\mathbf{m_1} \cdot \mathbf{v_0}) \exp(-i\,\gamma\,\mathbf{m_1} \cdot \mathbf{v_0}). \tag{4.2}$$

Effects of flow in a system of tubes with heterogeneous velocity, in both speed v and orientation φ, can be estimated by the superposition of the contributions of individual single tubes described above [19]. In general, for a system whose vessels are described by the probability density function $P(v, \varphi)$, the net effects for plug and laminar flows can be obtained by their respective expected values:

$$F_{multi-plug} = \iint P(v, \varphi) \exp(-i\, \gamma\, \mathbf{m_1} \cdot \mathbf{v})\, dv\, d\varphi \text{ , and} \tag{4.3}$$

$$F_{multi-laminar} = \iint P(v, \varphi) \operatorname{sinc}(\gamma\, \mathbf{m_1} \cdot \mathbf{v}) \exp(-i\, \gamma\, \mathbf{m_1} \cdot \mathbf{v})\, dv\, d\varphi. \tag{4.4}$$

4.3.2 Special Multitube Systems

In the special case of plug flow inside identically oriented tubes with Gaussian-distributed v, a closed-form analytical solution exists for $F_{multi-plug}$. Suppose the vessels makes an angle θ with respect to the motion encoding gradient axis, and that

$$P(v) = \frac{1}{\sqrt{2\pi\sigma_v^2}} \exp\left(-(v - v_m)^2/2\sigma_v^2\right), \tag{4.5}$$

where v_m and σ_v are the mean and standard deviation of the flow speeds, respectively. Because capillaries are interconnected and are driven by the same overall arterio-venous pressure differential, σ_v is directly proportional to v_m. Consequently, by equating $\sigma_v = cv_m$, with c being some constant of proportionality, Eq. (4.3) leads directly to

$$F_{multi-plug} = \exp\left(-\frac{1}{2}\gamma^2\, m_1^2\, c^2 v_m^2 \cos^2(\theta)\right) \exp(-i\, \gamma\, m_1 v_m \cos(\theta)). \tag{4.6}$$

Moreover, without loss of generality, suppose Stejskal-Tanner gradient pulses of duration δ and separation Δ are used. Substituting the corresponding $m_1 = \delta\Delta g$, and taking the magnitude of the modulation factor, Eq. (4..6) reduces to

$$\|F_{multi-plug}\| = \exp\left(-\frac{1}{2}\gamma^2\, (\delta\, \Delta g)^2\, c^2 v_m^2 \cos^2(\theta)\right), \tag{4.7}$$

which bears the general form of the signal attenuation $\exp(-b\,D^*)$ used in classical IVIM theory. Since the gradient weighting factor b in this case is $b = \gamma^2 g^2 \delta^2 (\Delta - \frac{\delta}{3})$, the flow-mediated pseudo diffusion coefficient D^* is equal to

$$D^* = \frac{\Delta^2 c^2}{2\left(\Delta - \frac{\delta}{3}\right)} v_m^2 \cos^2 \theta. \tag{4.8}$$

Following the convention of DTI, and assuming the tubes of the special system are oriented along the x-axis while the motion sensitizing gradient has the directional unit vector $\hat{\mathbf{g}}$, D^* can be expressed as a product $\hat{\mathbf{g}}$ and a special tensor entity,

$$D^* = \hat{\mathbf{g}}^T \cdot \begin{bmatrix} D_{\parallel}^* & 0 & 0 \\ 0 & 0 & 0 \\ 0 & 0 & 0 \end{bmatrix} \cdot \hat{\mathbf{g}} = D_{\parallel}^* \cos^2 \theta, \tag{4.9}$$

with $D_{\parallel}^* = \Delta^2\, c^2 v_m^2 / 2(\Delta - \frac{\delta}{3})$. Except for the specific definition of $D_{\parallel}^*$, which depends on the timing of the gradient pulses, the form of Eq. (4.9) is expected to be valid for other encoding schemes, provided of course that they have nontrivial first moments.

4.3.3 Generalized Multitube Systems in Tissues

For generalized multitube systems with either heterogeneous tube orientations, non-Gaussian speed distribution or laminar flow, a close-form solution for $F_{multi-plug}$ or $F_{multi-laminar}$ is more difficult to obtain, but its behavior can be studied via numerical analysis. To illustrate, consider plug and laminar flow under the extreme conditions when (i) the tubes have identical orientation as the encoding gradient but the speeds originate from Gaussian-distributed capillary diameters and variable input flow rates resulting in different v_m distributions, and (ii) vary the tube orientation φ in 2D (quasi Gaussian) with respect to the gradient encoding direction to simulate different flow anisotropies, while keeping the velocity distribution fixed. Results of the numerical

simulations are shown in Fig. 4.1 and Table 4.1, with the specific details of the approach

and more thorough investigations of configurations and effects of noise provided below

in the Methods section. Figure 4.1a corresponds to the special case discussed above

where the analytical solution for $F_{multi-plug}$ is available and serves as validation of the

numerical approach. By comparing Fig. 4.1b to 4.1a, and 4.1d to 4.1c, it is clear that, like

varying flow, different degrees of anisotropy results in different rates of MR signal

attenuations. By comparing Fig. 4.1c to 4.1a, and 4.1d to 4.1b, it is also clear that

laminar flow generally yields faster signal attenuation than plug flow for the same

networks of tubes, as predicted by the sinc term in Eq. (4.4). Moreover, as seen in Figs.

4.1c and 4.1d, the undulations normally associated with the sinc function are largely

smoothened out by having v_m, φ, and implicitly θ as random variables. Table 4.1 lists

the σ_v and D^* obtained for the flow conditions shown in Figs. 4.1a and 4.1c, and verifies

the expected linear and quadratic dependence of σ_v and D^*, respectively, on v_m. The

dependence D^* on v_m is not exactly quadratic due to the fact the flow speed distribution

is not perfectly Gaussian. Overall, this indicates that flow in a multi-tube system under a

wide variety of configurations likely results in signal attenuation that can be reasonably

approximated as an exponentially decaying function in the forms of Eqs. [4.7] and [4.8],

especially for low b-values. Since in the generalized system flow is no longer constrained

to the same orientation and along the x-axis, supposing flow yields exponentially

decaying functions with pseudo diffusion coefficients D_1^*, D_2^* and D_3^* along the tissue's

local principal axes in descending order of the dispersion rate, Eq. (4.9) can be extended

to,
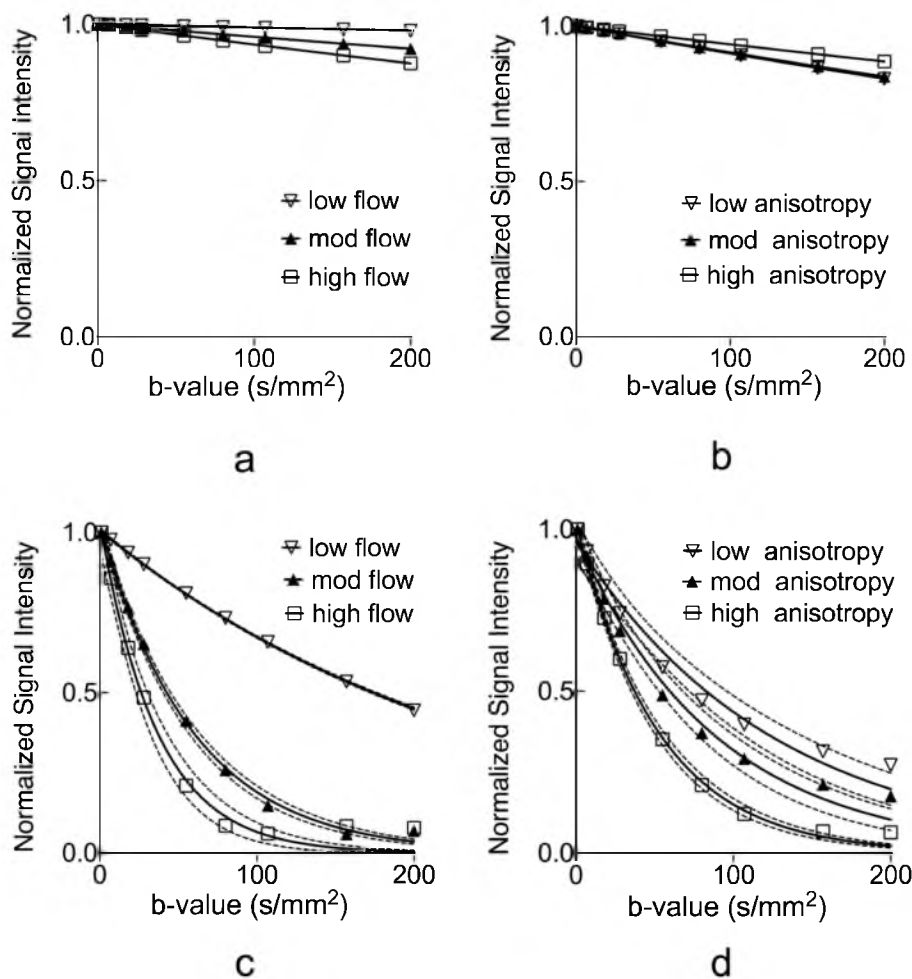
Figure 4.1. Numerical simulations of flow-induced MR signal attenuation. Panels correspond to (a) plug flow of varying speeds in tubes that have identical and same orientation as the encoding gradient. The low, moderate and high flow settings correspond to mean speeds (v_m) of 0.32 ± 0.13, 0.64 ± 0.25, and 0.86 ± 0.34 mm/s, respectively, obtained from Gaussian-distributed capillary radii at different flow rates. (b) plug flow of the same speed distribution as the "high flow" case above in tubes whose orientations have varying degree of anisotropy of quasi Gaussian-distributed capillary orientations with standard deviations of 52° (low anisotropy), 44° (mod anisotropy), and 28° (high anisotropy), respectively. Panels (c) and (d) are results obtained for laminar flow of the same volumetric flow rate under the same configurations as in (a) and (b), respectively. The solid lines denote nonlinear least-squares single exponential fits of the noiseless data points, and the dotted lines denote the 95% confidence interval of the fits.

Table 4.1. Quantified microcirculation parameters (mean velocity v_m and SD σ_v) in perfectly aligned tubes subjected to various input flow rates and the resulting single exponential fitted D^* for both plug and laminar flow cases.

v_m (mm/s)	σ_v (mm/s)	D^* Plug Flow (x10⁻³ mm²/s)	D^* Laminar Flow (x10⁻³ mm²/s)
0.32	0.13	0.16	4.51
0.64	0.25	0.61	18.05
0.86	0.34	1.07	31.48

$$D^* = \hat{\mathbf{g}}^T \cdot \mathbf{R}^T \cdot \begin{bmatrix} D_1^* & 0 & 0 \\ 0 & D_2^* & 0 \\ 0 & 0 & D_3^* \end{bmatrix} \cdot \mathbf{R} \cdot \hat{\mathbf{g}}, \tag{4.10}$$

where $\mathbf{R}$ is the orthonormal rotation matrix for transforming the laboratory frame of reference onto the tissue's local coordinates. A generalized pseudo diffusion tensor can then be defined as

$$\mathbf{D}^* = \mathbf{R}^T \cdot \begin{bmatrix} D_1^* & 0 & 0 \\ 0 & D_2^* & 0 \\ 0 & 0 & D_3^* \end{bmatrix} \cdot \mathbf{R}, \tag{4.11}$$

such that the microcirculation-mediated signal attenuation factor $F_{multi-tube}$ for both plug and laminar flow conveniently follows the form

$$\|F_{multi-tube}\| = \exp(-b\hat{\mathbf{g}}^T \cdot \mathbf{D}^* \cdot \hat{\mathbf{g}}). \tag{4.12}$$

4.4 Methods

4.4.1 Flow in Organized Tissues

Because the capillary network occupies only 3–25% of the tissue volume [20]–[23], a realistic tissue model needs to account for both vascular and nonvascular constituents. In the classical IVIM model [5], the diffusion signal in perfused tissues consists of nonexchanging extravascular and intravascular signals, denoted by the subscripts "tissue" and "blood", respectively, is given as

$$S(b)/S_0 = (1-f)\exp(-b\,D_{tissue}) + f\exp(-b\,D_{blood})\,F(b,v), \qquad (4.13)$$

where f is the vascular volume fraction (i.e., VF), S_0 is the reference nonweighted signal, D is the intrinsic apparent diffusion coefficients of the compartment, and F is the flow-mediated attenuation factor. In organized tissues, D_{tissue} is anisotropic, and can be related to the diffusion tensor of the tissue $\mathbf{D}_{tissue}$ according to well-established relationship $D_{tissue} = \hat{\mathbf{g}}^T \cdot \mathbf{D}_{tissue} \cdot \hat{\mathbf{g}}$. Incorporating the arguments from preceding paragraphs for the vascular compartment, Eq. (4.13) can then be modified for describing diffusion and flow in organized tissues according to,

$$S(b,\hat{\mathbf{g}})/S_0 = (1-f)\exp(-b\hat{\mathbf{g}}^T \cdot \mathbf{D}_{tissue} \cdot \hat{\mathbf{g}}) + f\exp\left(-b\hat{\mathbf{g}}^T \cdot \mathbf{D}^*_{app} \cdot \hat{\mathbf{g}}\right), \qquad (4.14)$$

where the intrinsic blood and flow induced pseudo diffusivities are combined into an apparent pseudo diffusion tensor $\mathbf{D}^*_{app} = D_{blood}\mathbf{I} + \mathbf{D}^*$, with $\mathbf{I}$ being the identity matrix. Eq. (4.14) provides the basis to model the diffusion signal in perfused organized tissues as a function of both encoding factor b and gradient direction $\hat{\mathbf{g}}$, and to interpret it as having two distinct diffusion tensor components, one associated with each extravascular and vascular compartments. In principle, Eq. (4.14) allows the tissue and the microcirculation compartments to have different orientations through the specifications

of $\mathbf{D}_{tissue}$ and $\mathbf{D}^*_{app}$, albeit whether such tissue exists in reality requires further validation with independent histological measurements of vessel orientations.

4.4.2 Realistic Tissue Model

Whereas previous studies [6], [14], [24] modeled the capillary network simply as a collection of straight tubes with identical radius, length and interior flow, a more realistic model that allowed flexible specifications of the capillary geometries and flow conditions while ensuring conservations of mass and momentum was used in the present work. The realistic network was constructed by first defining a voxel volume and placing in it nodes that represented bifurcations or confluences of capillary segments. Neighboring nodes were connected by capillary segments, which were randomly assigned a Gaussian-distributed diameter of 5 ± 1 μm (mean $\pm$ SD) with uniform length of 200 μm [20]. The volumetric flow rate in the k-th capillary segment $\dot{Q}_k$ was related to the capillary radius r_k and length l_k by means of Darcy's law (conservation of momentum) $\dot{Q}_k = \Delta p_k / R_k$, where Δp_k was the pressure differential at two ends of the capillary, and $R_k = 8\eta l_k / \pi r_k^4$ was the hydraulic resistance of a Newtonian fluid with viscosity $\eta = 3.5 \times 10^{-3} \, Pa \cdot s$. Conservation of mass for incompressible fluid was achieved by enforcing $\sum \dot{Q}_k = 0$ at each node. The mean flow speed in each capillary was calculated via $v_k = \dot{Q}_k / \pi r_k^2$. In the above manner, capillary networks with various orientation and flow distribution function $P(v, \varphi)$ were empirically configured by adjusting Δp_k (via $\dot{Q}$) and placements of the nodes.

4.4.3 MR Signal Simulation

Numerical experiments to examine the effects of varying each capillary flow speed and degree of orientation anisotropy to the MR signal were conducted using Matlab (Version R2014a, Mathworks, Natick, MA). To investigate flow speed, the same perfectly aligned network was subject to different input flows to achieve v_m of speeds 0.32 ± 0.13 (low), 0.64 ± 0.25 (moderate), and 0.86 ± 0.34 mm/s (high). Behaviors of the vascular signal attenuation for $\theta = 0°$ are shown in Fig. 4.1c. For varying the degree of anisotropy, v_m of 0.86 ± 0.34 mm/s was used in networks having quasi-Gaussian distributed φ with standard deviations of $52°$ (low), $44°$ (moderate), and $28°$ (high anisotropy). The vascular signal attenuation for $\theta = 0°$ are shown in Fig. 4.1d. For all networks, the direction of the mean capillary orientation was taken to be the x-axis.

For each capillary configuration described above, Eq. (4.4), which applied to laminar flow found in perfused isolated hearts, was used along with the given $P(v, \varphi)$ to generate the flow-induced signal attenuation factor $F_{mutli-laminar}$. Relative absolute encoding angle θ ranged from $0°$ (i.e., oriented parallel to the x-axis) to $90°$ (y-axis) in $10°$ increments, with rectangular gradient pulses with δ of 5 ms, Δ of 15 ms, and g ranging from 0 to 200 mT/m in 13 exponentially spaced steps. Subsequently, using $\mathbf{D}_{tissue}$ eigenvalues of 1.5, 1.0, and 1.0 x 10^{-3} mm^2/s, f of 15% [25], and D_{blood} of 3.0 x 10^{-3} mm^2/s, signal intensities $S(b, \hat{g})$ were synthesized according to

$$S(b, \hat{g})/S_0 = (1 - f) \exp(-b\hat{g}^T \cdot \mathbf{D}_{tissue} \cdot \hat{g}) + f \exp(-bD_{blood}) \| F_{mutli-laminar} \|.$$

$$(4.15)$$

Gaussian noise was added to achieve signal-to-noise ratio (SNR) of 100, similar to that found in the experimental study. For each encoding direction and level, the

capillary network and corresponding MR signal were generated 50 times then averaged to mimic the behaviors of as many neighboring and similar voxels in an ROI that contained minor structural variations.

4.4.4 Data Analysis

The resulting averaged MR signal for each capillary configuration and relative encoding angle θ, as a function of the b value, was analyzed using to the "two-step" parameter estimation approach commonly employed in IVIM studies [26]. First, nonlinear least-squares single-exponential fit was performed on signal intensities obtained for b values greater than 200 s/mm^2 to estimate the scalar D_{tissue}. The choice of the minimum b > 200 was taken similar to a previous study in the heart [13], and the implication of this choice on the measured IVIM parameters will be revisited in the discussion section below. Subsequently, with D_{tissue} fixed, a two-parameter fit was performed on signal intensities over the full range of b values using Eq. (4.14) to yield f and D_{app}^*. The parameters were repeatedly estimated 7 times (each with newly generated capillary networks and signals) to represent results obtained from different subjects, averaged and plotted as functions of $|\theta|$, along with results obtained without adding image noise to serve as basis for reference.

4.4.5 Isolated Heart Preparation

All animal procedures were approved by the University of Utah Institutional Animal Care and Use Committee. Retired breeder male guinea pigs (n = 7, 900 ± 100 g, mean ± SEM) were anesthetized using pentobarbital sodium (30 mg/kg, i.p.) and their hearts were rapidly excised. Using a MRI-compatible Langendorff apparatus as

described previously [15], the heart was immediately perfused retrogradely via the aorta with Tyrode's solution consisting of (in mM) 1.25 $CaCl_2$, 140 NaCl, 4.6 KCl, 5.5 dextrose, 0.7 $MgCl_2$, and 10 HEPES at 7.40 pH and oxygenated with 100% O_2. Myocardial contraction was partially inhibited by an electromechanical uncoupler, 2,3-butanedione monoxime (7.5 mM). Bovine serum albumin (0.4% wt/wt) was added to the perfusate to minimize interstitial edema [27].

A raised, pump-fed (Masterflex C/L, Fisher Scientific, Barrington, IL, USA) reservoir was used both as a means to trap air bubbles and to adjust the aortic perfusion pressure, which was continuously recorded via a pressure transducer (SPR882 Pressure Probe, AD Instruments, Colorado Springs, CO, USA) placed in the perfusion line immediately upstream of the aorta. MR imaging experiments were conducted at two perfusion settings: (a) normal (physiologic) perfusion, with flow and pressure set at 20 ml/min and 47 ± 4 mmHg (mean ± SEM, n=7), respectively, and (b) low perfusion, with pump turned off and pressure of 20 ± 4 mmHg. (Perfusion did not completely stop when the pump was turned off due to residual perfusate and hydrostatic pressure remaining in the perfusion line.) The perfused heart was completely immersed along with a saline-filled sealed tube used as reference standard in a chamber inside the imaging RF coil. Temperature inside the chamber was maintained via the warm inflow perfusion line at 36.0 ± 0.2 °C during normal flow, but dropped to 33.6 ± 0.3 °C when flow was stopped. To reduce bulk motion artifacts, the heart was arrested with 20 mM potassium in the Tyrode solution (described above) immediately before imaging at each flow rate. Before changing the flow setting, the heart was perfused normally with Tyrode's solution and allowed to beat for ~10 min to ascertain its viability.

4.4.6 MRI Acquisition

MRI experiments were conducted using a custom-built loop-gap RF resonator interfaced to a Bruker Biospec 7T scanner (Bruker Biospin, Ettlingen, Germany). For each flow setting, 3.0 mm-thick, 38×30 mm^2 FOV cardiac short-axis images at the center of the heart at identical slice location were obtained, including (a) a FLASH scan (92 ms TR, 6 ms TE, 30° flip angle, 256×256 matrix size) for anatomical visualization, (b) spin-echo flow-sensitive inversion recovery (FAIR) scan with single-shot echo planar imaging (EPI) readout (10 s TR, 35 ms TE, 128×100 matrix size), and alternating slice-selective and nonselective inversion preparation and 22 inversion times ranging from 30 ms to 10 s, for ASL quantification of flow, and (c) interleaved four-shot spin-echo diffusion-weighted EPI scans (2 s TR, 25 ms TE, 164×128 matrix size) encoded in each slice-selection and readout directions with 13 b-values (nominally 1, 7, 18, 28, 55, 80, 107, 157, 200, 310, 513, 766, and 1020 s/mm^2). Total scan time for the FLASH, FAIR and diffusion-weighted (DW) scans was approximately 20 min at each flow setting.

4.4.7 Data Analysis

For each scanned heart, the left ventricular (LV) circumferential fiber region, readily identified as the ring-shaped hyperintense area in heavily weighted diffusion-weighted images encoded in the cardiac long axis (or slice-selection axis), was manually delineated, and divided into 4 ROIs by binning the pixels according to the absolute angle the fiber orientation made with respect to the image horizontal (readout) axis, yielding nominal $|\theta|$ of 0°, 30°, 60°, and 90°.

For each flow setting, D_{tissue}, f and D_{app}^* were estimated using the ROI-averaged diffusion-weighted signal intensities encoded in the readout direction obtained

via the two-step IVIM analysis described above. To account for the tissue temperature difference, D_{tissue} of the myocardium was normalized using the mean apparent diffusion coefficient obtained for the saline phantom. Normalization of D^*_{app} was not required since it reflected mostly pressure-driven flow and not thermal Brownian motion. For each flow setting, IVIM parameter as a function of $|\theta|$ was compared via one-way repeated measures ANOVA (GraphPad Prism 5.0a, GraphPad Software Inc., La Jolla, CA). In the Bonferroni-corrected *post hoc* tests, since the approximate capillary orientation was already known, hence, to reduce the number of comparison, only values observed at $|\theta|$ = 30°, 60°, and 90° were compared to that at $|\theta|$ = 0° for a total of 3 tests. Significance for all statistical tests was set at overall P < 0.05. Finally, myocardial "blood" flow (MBF) maps were generated as described previously [60] using slice-selective (T_1^{ss}) and nonselective (T_1^{ns}) longitudinal relaxation times estimated from pixel-by-pixel nonlinear least-squares fitting of the corresponding FAIR intensities via

$$MBF = \lambda \, (T_1^{ns}/T_1^{ss} - 1)/T_1^{blood}, \qquad (4.16)$$

where 0.9 ml/g was used for the myocardial blood-tissue partition coefficient λ, and the T_1^{ns} obtained for the fluid in the ventricular cavity was taken as T_1^{blood}. MBF was averaged over the entire LV area. As independent validation of the MBF measurement, the MBF was correlated to the aortic input pressure, which is proportional to the myocardial blood flow assuming the myocardial capillary bed resistance is approximately constant [20], [28]. Subsequently, ASL-based MBF measurements were used to obtain scatter plots with each of the above measured IVIM parameters D^*_{app}, f, and D_{tissue}. To quantify the relationships, the plot of D^* was fitted to a quadratic (indicated in Eq. (4.8)), whereas other parameters (VF and tissue ADC) were each empirically fitted to a line.

4.5 Results

Figure 4.2 shows the plots obtained in the numerical experiments for D^*_{app}, f, and

D_{tissue} in the same capillary networks as functions of the relative encoding angle θ for

different flow speeds. Overall, D^*_{app} and D_{tissue} exhibit the expected half-cosine behavior

from the square of directional cosine. With respect to the flow speed, the amplitude of

D^*_{app} is clearly nonlinear, whereas that of D_{tissue} appears constant.

The values for D^*_{app} at $|\theta| = 0°$ were 9.3, 21.4 and 35.6 x 10^{-3} mm^2/s for low,

moderate, and high flows, respectively, which are consistent with D^* reported in Table

4.1 when accounting for D_{blood}. Moreover, compared to the theoretical value of 15%,

the volume fraction f is both underestimated and θ-dependent, with markedly larger

underestimation associated with either smaller D^*_{app} or larger θ. Because the underlying

capillary network configuration and flow conditions in Table 4.1 and Fig. 4.2 are
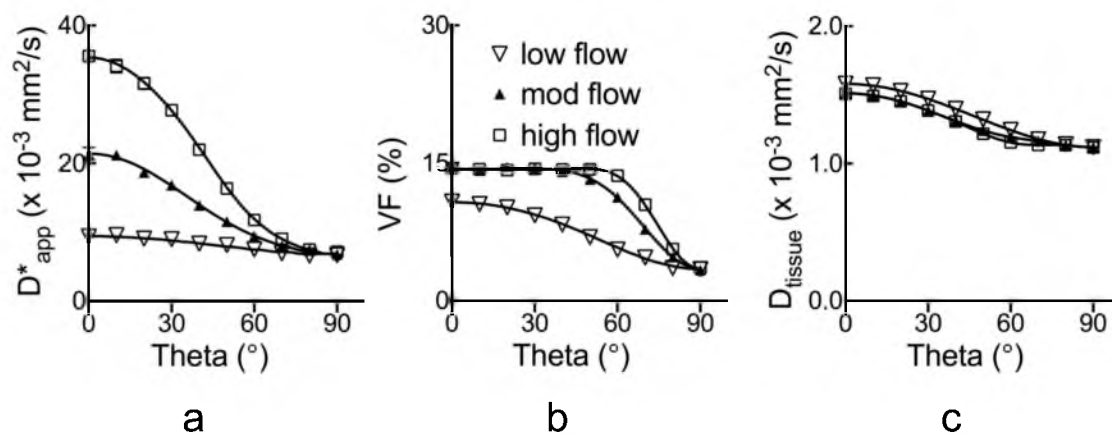
Figure 4.2. Anisotropy of tissue IVIM parameters in numerical analysis of laminar flow in the same perfectly aligned capillary network as a function of encoding angle θ. The low, moderate and high flow settings correspond to mean speeds (v_m) of 0.32 ± 0.13, 0.64 ± 0.25, and 0.86 ± 0.34 mm/s, respectively, obtained from Gaussian-distributed capillary radii at different flow rates. Behaviors of the vascular signal attenuation for $\theta = 0°$ are shown in Fig. 1c. Solid lines represent results obtained in the noiseless simulation

identical, and that only the latter contains tissue compartmental modeling and two-stage parameter fitting, these discrepancies more likely reflect systematic limitations of the compartmental mixing and fitting techniques than the flow modeling. Figure 4.3 shows the graphs of D^*_{app}, f, and D_{tissue} similarly obtained for capillary networks of different degrees of anisotropy but identical flow distribution. In general, D^*_{app} and D_{tissue} follow the same wavy orientation-dependent behaviors as observed in Fig. 4.2, and f also appears slightly underestimated. Considering that D^*_{app} should be isotropic in a network of completely randomly oriented capillaries, not surprisingly, the amplitude of D^*_{app} variation across θ diminishes when the degree of anisotropy or alignment decreases, which manifests as decreasing D^*_{app} for smaller $|\theta|$ and the opposite at larger $|\theta|$. This behavior is consistent with the flow-induced signals seen in Fig. 4.1d, where $|\theta| = 0°$.
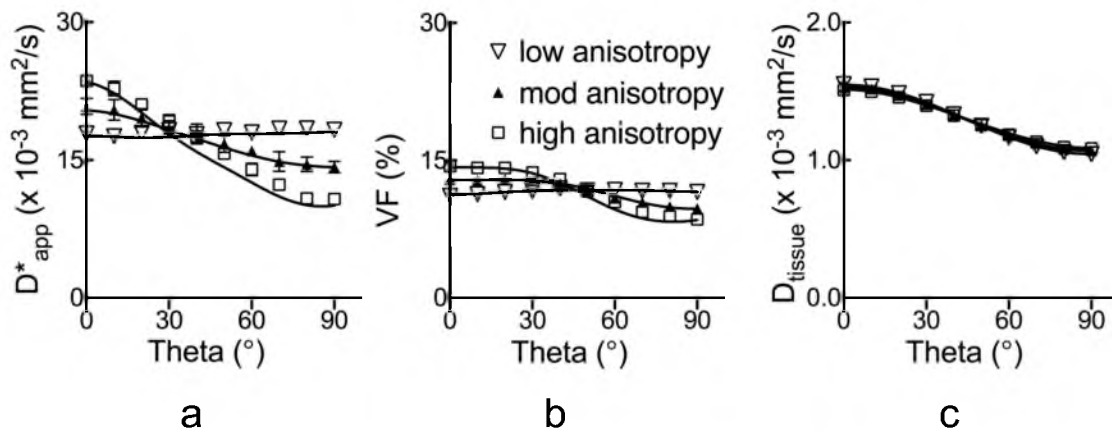
Figure 4.3. Orientation dependence of tissue IVIM parameters in numerical analysis of same laminar flow distribution ($v_m = 0.86 \pm 0.34$ mm/s) in capillary networks of varying degrees of anisotropy. The low, moderate and high anisotropy settings correspond to quasi Gaussian-distributed capillary orientations with standard deviations of 52°, 44° and 28°, respectively. Behaviors of the vascular signal attenuation for θ=0° are shown in Fig. 4.1d. Solid lines represent results obtained in the noiseless simulation.

Representative MR images and signal decay curves obtained from the perfused isolated heart experiments appear in Figs. 4.4 and 4.5, respectively. Figure 4.4 includes a FLASH image revealing the general morphology, and heavily diffusion-weighted images sensitized in each readout and slice directions. Figure 4.5 shows that all signals observed in parallel and perpendicular directions to the fibers, and at normal and low flow, exhibit nonmonoexponential behavior as functions of the encoding b-value. However, departure from nonmonoexponential behavior is greatest for signal encoded in the parallel direction at normal flow, which is suggestive of not only a large presence of the flow-mediated component, but also its anisotropy.
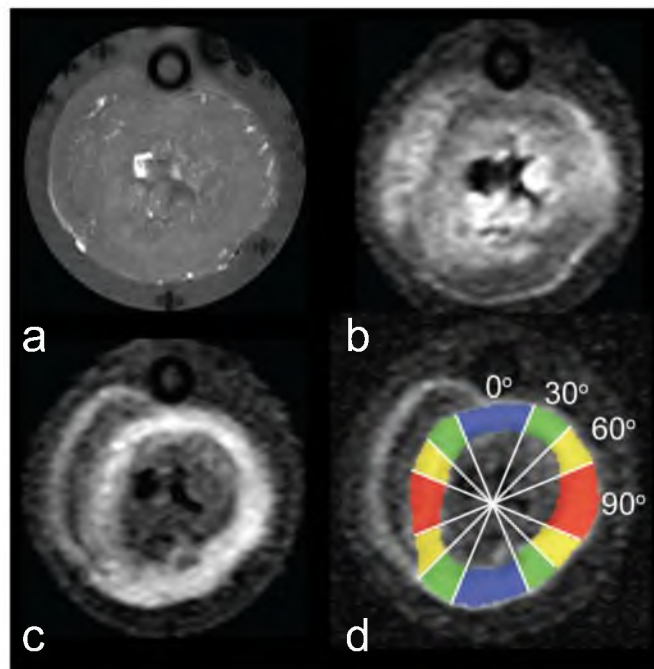
Figure 4.4. MRI of a representative isolated perfused heart. Images were obtained from a FLASH scan showing the gross morphology (a), and diffusion-weighted scans encoded in each of readout (horizontal) axis (b) and slice (in-out of page) direction (c). The latter is used to delineate the left ventricular circumferential fiber region (d) and bin the pixels into 4 approximately equal-size regions-of-interest according to the circumferential location and the relative absolute angle the fibers made with respect to the readout (horizontal) gradient direction.
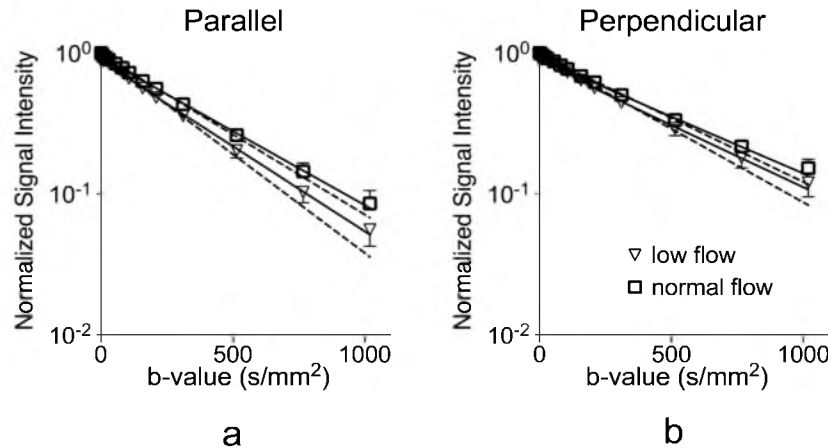
Figure 4.5. Experimental diffusion-weighted signal intensities in a representative isolated heart. Normalized signal intensities over the selected ROIs (mean ± SD) measured for diffusion encoded parallel (a) and perpendicular (b) to the left ventricular circumferential fiber direction are plotted on a semi-log scale. Inverted triangles and open squares correspond to low and normal flow settings, respectively. Solid and dotted lines represent IVIM (two-compartment) and mono-exponential fits, respectively, of the data points.

Figure 4.6 displays the graphs of D^*_{app}, f, and D_{tissue} as functions of discretized $|\theta|$ observed at normal and low flow in the perfused myocardium. Compared to the value at $|\theta| = 0°$, the experimental D^*_{app} is significantly reduced for the two highest angles at normal flow, whereas no significant change is seen for all $|\theta|$ at low flow.

The volume fraction f remains unchanged for different $|\theta|$, and is uniformly higher in normal flow than low flow, in agreement with the theory and that the blood volume is known to change proportionally to myocardial perfusion [66]. In contrast, D_{tissue} appears largely unchanged between the two flow settings and is significantly reduced for the two higher encoding angles at both flow settings, consistent with its extravascular origin and the well-known anisotropy of the myocardial microstructure in the DTI literature [13].

Overall, within the noise of the experimental data, these observations are
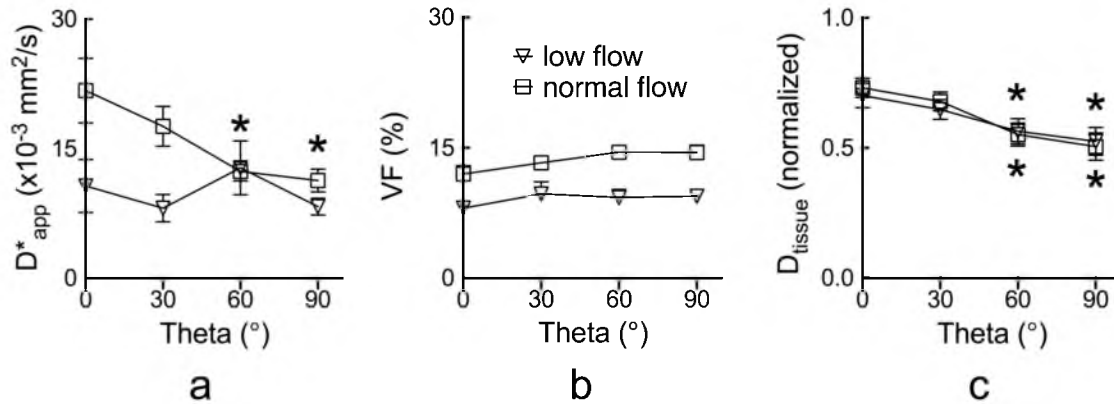
Figure 4.6. Anisotropy of experimentally observed IVIM parameters in isolated perfused hearts. The group averaged parameters (mean ± SEM, n = 7) are plotted as a function of the nominal relative encoding angle obtained as illustrated in Fig. 4.4d. Entries with asterisks (*) are significantly different from values observed at $|\theta| = 0°$ for each flow setting according to one-way repeated-measures ANOVA, which include D_{app} under normal flow at $|\theta|$ of 60° and 90°, and D_{tissue} under both normal and low flow at $|\theta|$ of 60° and 90°.

qualitatively consistent with the simulated results obtained for different flow speeds shown in Fig. 4.2, and are in very good agreement with the key predictions of the proposed theory. Representative T_1 and MBF maps associated with the ASL experiment obtained at low and normal flow are shown in Fig. 4.7. Consistent with the perfusion states, the average MBF obtained from all hearts decreased from 85 ± 7 at normal flow to 5 ± 3 ml/min/100g (mean ± SEM, n = 7, P < 0.01) when the pump was turned off. Figure 4.8 shows a good correlation between MBF measurements and aortic pressure (Pearson r = 0.78, P < 0.01), which suggests that, despite their relative noisiness, the ASL quantities are a reasonable first-order approximation of the underlying blood flow.

The scatter plots between MBF and each D_{app}^*, f and D_{tissue} for different encoding angles $|\theta|$ are shown in Fig. 4.9. Due to the experimental noise, modest coefficients of determination were found for D_{app}^* and f.
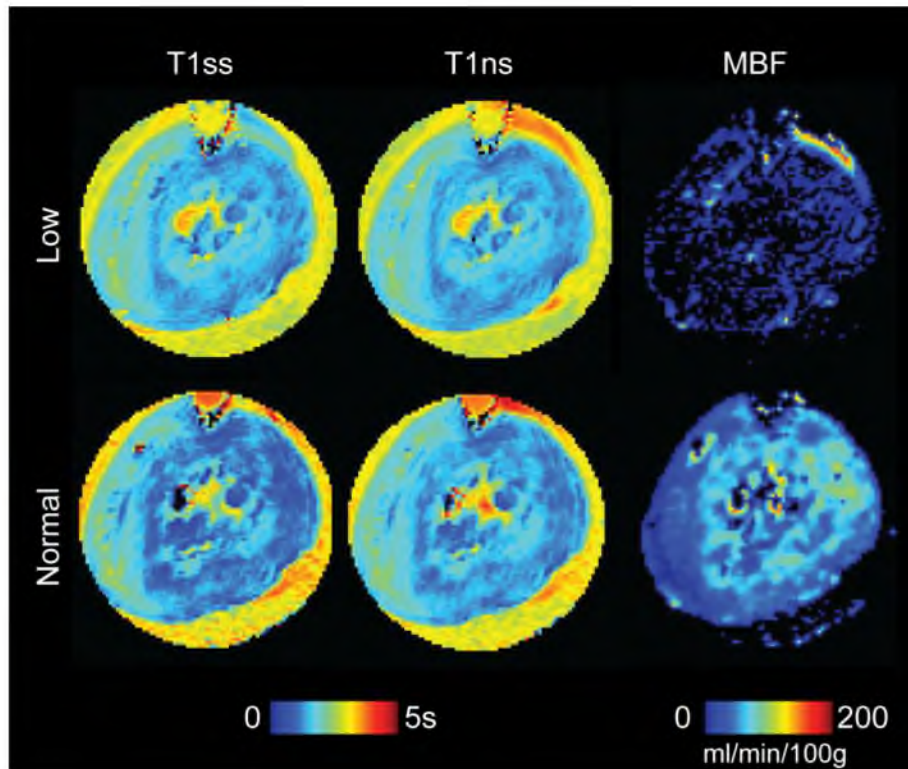
Figure 4.7. Arterial spin labeling MRI of a representative isolated heart. Slice-selective and nonselective FAIR images are used to obtain the falsecolor-coded longitudinal relaxation T_1^{ss} and T_1^{ns} maps, respectively, and subsequently the myocardial blood flow (MBF) map, for both normal and low flow settings.
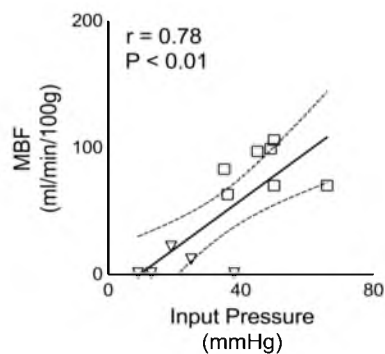
Figure 4.8. Scatter plot between ASL-based myocardial blood flow (MBF) measurements in a ROI spanning whole heart slice (mean ± SEM) versus (aortic) input pressure in each heart. Open squares correspond to normal flow rate while inverted triangles correspond to low flow setting. Linear regression solid line and 95% confidence bands (dotted lines) are overlaid over the data points. Pearson correlation coefficient (r) is reported, along with the P value in top left corner, shows strong correlation between mean ASL-based MBF measurements and the recorded aortic pressures. Note that the SEM error bars are too small to be seen.
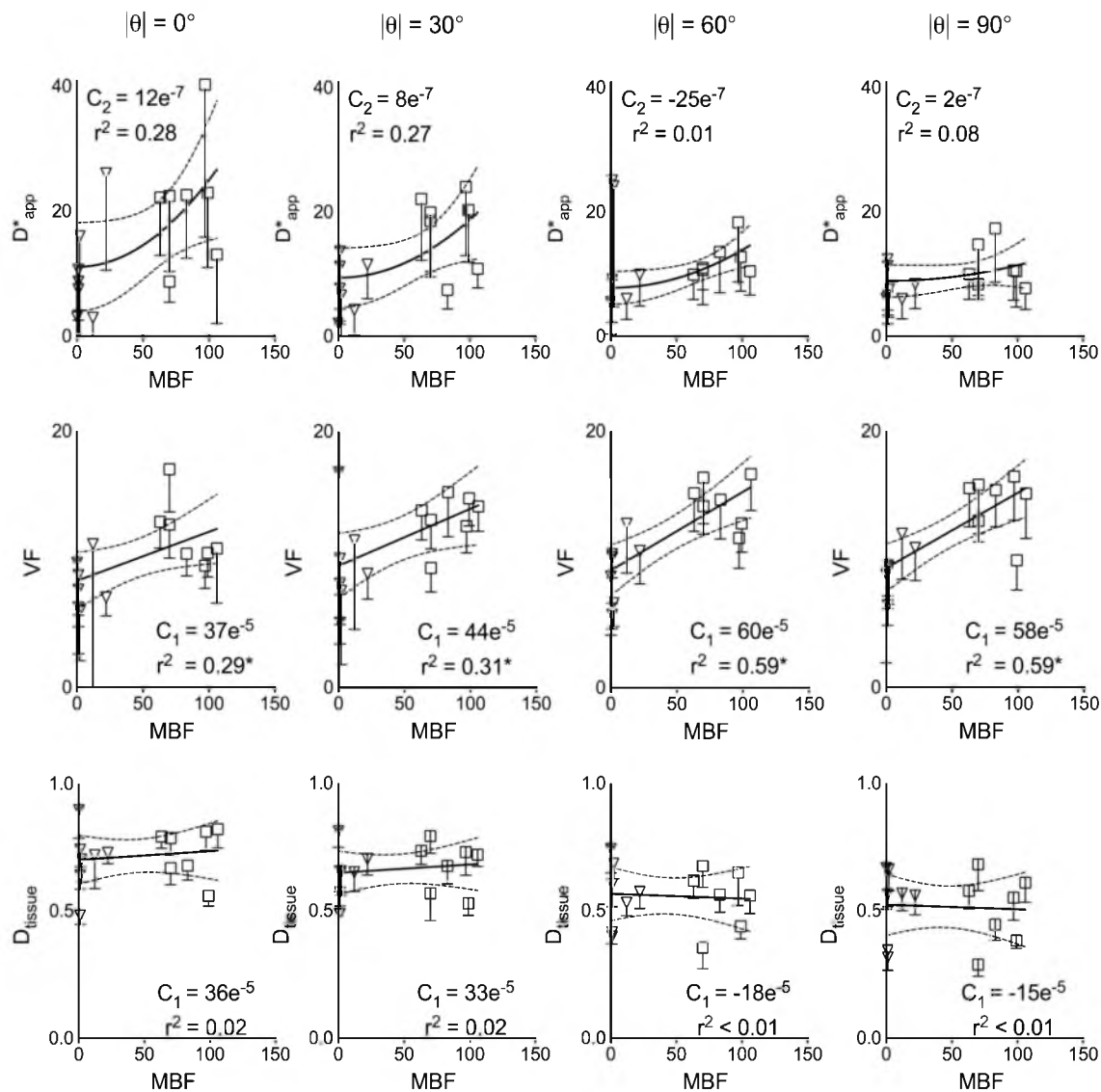
Figure 4.9. IVIM parameters graphed as functions of ASL-derived MBF for different encoding angles. Measurements obtained at both low (inverted triangles) and normal (open squares) flow setting are combined in the scatter plots. The D^*_{app} and the other parameters are fitted to a quadratic and straight (solid) line respectively, with the order of the polynomial indicated in the subscripts of the C coefficients. Error bars obtained from IVIM fitting are shown with each data point, and the 95% confidence interval dotted bands of the regression fit are also displayed. The coefficient of determination r^2 is reported under each coefficient (with asterisks in 2nd row denote $P < 0.05$ for linear regression). Units of MBF is ml/min/100g, $D^*_{app} \times 10^{-3}\ mm^2/s$, D_{tissue} normalized units, and VF is % of total volume.

Nevertheless, the predicted decrease in the concavity of D^*_{app} as $|\theta|$ increases is apparent. There also appears a trend of increasing slope of f as $|\theta|$ increases, which agrees with the underestimation of the parameter seen in Fig. 4.2. Lastly, as expected, no obvious trend or significant dependence on MBF was found for D_{tissue}, which demonstrates the relative reliability of the two-stage fitting technique for capturing microstructural information of the extravascular compartment in the perfused myocardium.

4.6 Discussion

The current work presents a theoretical framework based on a combination of familiar IVIM and DTI formulations as stated in Eq. (4.14) to describe the anisotropy of microcirculation-induced diffusion signal. Like in IVIM, the signal is modeled as one that comprises separable parts from each vascular and nonvascular compartment. And similar to DTI, contribution of each compartment is described by an apparent diffusivity equal to the linear algebraic product between the motion-encoding unit vector and the appropriate tensor entity associated with the direction of the local microstructure or microvasculature. Results of both simulation and empirical experiments (e.g., Figs. 4.2 and 4.6, respectively) confirmed the dependence of the flow-mediated signal on the relative encoding angle and speed of flow. The simulations (Fig. 4.3) also verified the dependence of the signal on the degree of anisotropy or alignment of the microvasculature.

Overall, the behaviors of the microcirculation-induced signal observed numerically and experimentally are in very good agreement with predictions of the proposed theoretical framework. The orientation-dependent flow effect on IVIM has been

previously observed in the heart and skeletal muscle at physiologic conditions [13], [14]. The main discrepancy between the current work and previous study of the perfused myocardium [13] or formulation of partially coherent system [14] exists in the interpretation of the microcirculation-induced signal attenuation factor (i.e., $\|F_{multi-tube}\|$). Previously, the attenuation factor was interpreted as part of the vascular fraction, giving it an apparent anisotropic behavior. In the present study, the dependence of the attenuation factor on the encoding gradient strength (i.e., b-value) and the empirical exponential nature of the attenuation were combined into D^*. Consequently, it became possible to express D^* as a function of the gradient encoding direction, leaving the vascular volume fraction constant. The authors believe that both approaches are equally valid, except that by adopting the familiar DTI formalism, the current framework provides a more intuitive and convenient alternative for describing the anisotropy of the microcirculation-induced signal. However, since the experimental validation experiment tested end points of normal flow range (i.e., "physiologic" and "oligemia'"), and that the observed changes in D^*_{app} were smaller than those observed in ASL at different flow conditions, further investigation is needed to explain the apparent mismatch between the 2 techniques.

Nonetheless, the anisotropic behavior of flow-mediated signal is expected to have profound implications for *in vivo* DTI at least in the myocardium, which is increasingly used thanks to recent technical advances [30]–[32]. Because the myocardial microvasculature and myofibers are aligned [10], flow is expected to have little or no impact on the observed DTI directionality (e.g., myocardial fiber direction). However, since D^* is most pronounced in the direction of flow and fibers, and that conventional

DTI is tantamount to fitting the apparent diffusivity that includes flow effects in each encoding direction to a single exponential decay, the flow-induced signal will contribute to an artificially inflated first eigenvalue of the diffusion tensor in the perfused myocardium, which in turn yield an overestimated fractional anisotropy (FA). The latter may be of particularly concern since it can mask the small FA reduction that is often linked to myocardial pathology, including fiber disarray [33] and fibrosis [34]. To mitigate the adverse impact, as essentially done in the two-stage fitting approach, relatively large diffusion-weighting b-values can be employed to take advantage of the faster decay of the flow-induced signal [35]. Since higher b-values are often associated with heightened bulk motion sensitivity, a more practical alternative may be to employ encoding schemes such as bipolar gradient pulses that have zero first moments [31], [36] or compensated higher order motion [32].

As seen in the simulation results, a potential practical limitation of the proposed theoretical framework exists in either or a combination of the two-compartment signal modeling and the two-stage parameter fitting approach used. In the latter, residual flow-induced signal at higher b-values is interpreted as part of the tissue signal. Although the additional contribution yields only a small overestimation of D_{tissue} due to the relatively large size of the tissue compartment, the overestimated diffusivity has an amplified effect and leads to an underestimation of the vascular volume fraction accompanied by overestimation of the flow-related D_{app}^* observed in Fig. 4.2 and 4.3. Further, using the ASL-MBF measurements at normal flow (85 ml/min/100g) yields extrapolated v_m of 0.35 mm/s (for a voxel of 0.3 mm x 0.3 mm x 3 mm containing parallel capillaries with 12% volume fraction as shown in Fig. 4.6b at $|\theta| = 0°$), which seems underestimated

compared to the values reported in Table 4.1 at moderate flow. This likely suggests that the experimental VF was overestimated for not accounting the relaxation times differences between the intravascular and tissue compartments [37]. The degree in which these concerns apply to the analysis of experimental data depends on the appropriateness of the two-compartment mixing approximation for modeling the signal empirically observed in organized tissues, and whether a better approach for the multi-parameter fitting can be found. Because of the above reasons, caution is warranted in interpreting at least the scalar quantitative characterization of the anisotropy of flow-induced diffusion signal.

In conclusion, a theoretical framework utilizing conventional IVIM and DTI formulations to describe the anisotropy of microcirculation-mediated diffusion signal was presented. The theory predicted that the pseudo diffusivity measured using conventional IVIM approach can be described as the linear algebraic product between the encoding directional unit vector and an appropriate tensor entity, similar to DTI. In doing so, the anisotropy of the signal is manifested in the apparent rates of diffusion, and not in the vascular volume fraction. Within the limits of the noise and the employed signal modeling and fitting techniques, the proposed theory was validated via both numerical simulations and empirical observations in perfused isolated heart experiments. These findings suggest that the presented theory can provide a convenient alternative to characterize diffusion and microcirculation in organized tissues, which has timely and significant implications for *in vivo* cardiac DTI.

4.7 References

1.   Stejskal EO, Tanner JE. Spin diffusion measurements: spin echoes in the presence of a time-dependent field gradient. J Chem Phys. 1965;42(1):288.

2.   Stejskal EO. Use of Spin Echoes in a Pulsed Magnetic-Field Gradient to Study Anisotropic, Restricted Diffusion and Flow. J Chem Phys. 1965;43(10).

3.   Moseley ME, Cohen Y, Mintorovitch J, Chileuitt L, Shimizu H, Kucharczyk J, et al. Early detection of regional cerebral ischemia in cats: comparison of diffusion- and T2-weighted MRI and spectroscopy. Magn Reson Med. 1990 May;14(2):330–46.

4.   Basser PJ, Mattiello J, LeBihan D. MR diffusion tensor spectroscopy and imaging. Biophys J. 1994 Jan;66(1):259–67.

5.   Le Bihan D, Breton E, Lallemand D, Grenier P, Cabani E, Jeantet L. MR imaging of intravoxel incoherent motions: application to diffusion and perfusion in neurologic disorders. Radiology. 1986;161:401–7.

6.   Le Bihan D, Breton E, Lallemand D, Aubin M-L, Vignaud J, Laval-Jeantet M. Separation of diffusion and perfusion in intra voxel incoherent motion MR imaging. Radiology. 1988;168(2):497–505.

7.   Kärger J. NMR self-diffusion studies in heterogeneous systems. Adv Colloid Interface Sci. 1985 Aug;23(0):129–48.

8.   Niendorf T, Dijkhuizen RM, Norris DG, van Lookeren Campagne M, Nicolay K. Biexponential diffusion attenuation in various states of brain tissue: implications for diffusion-weighted imaging. Magn Reson Med. 1996 Dec;36(6):847–57.

9.   Hsu EW, Buckley DL, Bui JD, Blackband SJ, Forder JR. Two-component diffusion tensor MRI of isolated perfused hearts. Magn Reson Med. 2001 Jun;45(6):1039–45.

10.   Poole D, Mathieu-Costello O. Analysis of capillary and subendocardium geometry in rat subepicardium. Am J Physiol Hear Circ Physiol. 1990;259:204–10.

11.   Vignaud A, Rodriguez I, Ennis DB, DeSilva R, Kellman P, Taylor J, et al. Detection of myocardial capillary orientation with intravascular iron-oxide nanoparticles in spin-echo MRI. Magn Reson Med. 2006 Apr;55(4):725–30.

12.   Hsu EW, Buckley DL, Bui JD, Blackband SJ, Forder JR. Two-component diffusion tensor MRI of isolated perfused hearts. Magn Reson Med. 2001 Jun;45(6):1039–45.

13.   Kaneko N, Matsuda R, Toda M, Shimamoto K. Three-dimensional reconstruction

of the human capillary network and the intramyocardial micronecrosis. Am J Physiol Heart Circ Physiol. 2011 Mar;300(3):H754–61.

14.   Callot V, Bennett E, Decking UKM, Balaban RS, Wen H. *In vivo* study of microcirculation in canine myocardium using the IVIM method. Magn Reson Med. 2003 Sep;50(3):531–40.

15.   Karampinos DC, King KF, Sutton BP, Georgiadis JG. Intravoxel partially coherent motion technique: characterization of the anisotropy of skeletal muscle microvasculature. J Magn Reson Imaging. 2010 Apr;31(4):942–53.

16.   Poelzing S, Veeraraghavan R. Heterogeneous ventricular chamber response to hypokalemia and inward rectifier potassium channel blockade underlies bifurcated T wave in guinea pig. Am J Physiol Heart Circ Physiol. 2007 Jun;292(6):H3043–51.

17.   Fidler F, Wacker C, Dueren C, Weigel M, Jakob P, Bauer W, et al. Myocardial Perfusion Measurements by Spin-Labeling Under Different Vasodynamic States. J Cardiovasc Magn Reson. 2004 Apr 5;6(2):509–16.

18.   Callaghan PT, Codd SL, Seymour JD. Spatial coherence phenomena arising from translational spin motion in gradient spin echo experiments. Concepts Magn Reson. 1999;11(4):181–202.

19.   Codd S, Manz B, Seymour J, Callaghan P. Taylor dispersion and molecular displacements in Poiseuille flow. Phys Rev E. 1999 Oct;60(4):R3491–4.

20.   Ahn CB. The effects of random directional distributed flow in nuclear magnetic resonance imaging. Med Phys. 1987;14(1):43.

21.   Levick JR. An Introduction to Cardiovascular Physiology. Third. Koster J, editor. London, UK: Arnold; 2001.

22.   Leenders KL, Perani D, Lammertsma AA, Heather JD, Buckingham P, Healy MJ, et al. Cerebral blood flow, blood volume and oxygen utilization. Normal values and effect of age. Brain. ENGLAND; 1990 Feb 1;113((Pt 1)):27–47.

23.   Toyota E, Fujimoto K, Ogasawara Y, Kajita T, Shigeto F, Matsumoto T, et al. Dynamic changes in three-dimensional architecture and vascular volume of transmural coronary microvasculature between diastolic- and systolic-arrested rat hearts. Circ Res. 2002;105:621–6.

24.   Luciani A, Vignaud A, Cavet M, Van Nhieu J, Mallat A, Ruel L, et al. Liver Cirrhosis: Intravoxel Incoherent Motion MR Imaging — Pilot Study. Radiology. 2008;249(3):891–9.

25.   Wetscherek A, Stieltjes B, Laun FB. Flow-compensated intravoxel incoherent motion diffusion imaging. Magn Reson Med. 2014 Aug 12.

26.   Delattre BMA, Viallon M, Wei ÞH, Zhu YM, Feiweier T, Pai VM, et al. *In vivo* Cardiac Diffusion-Weighted Magnetic Resonance Imaging Quantification of Normal Perfusion and Diffusion Coefficients With. Invest Radiol. 2012;47(11):662–70.

27.   Federau C, Meuli R, O'Brien K, Maeder P, Hagmann P. Perfusion measurement in brain gliomas with intravoxel incoherent motion MRI. AJNR. 2014 Feb;35(2):256–62.

28.   Arbel ER, Prabhu R, Ramesh V, Pick R, Glick G. A perfused canine right bundle branch-septal model for electrophysiological studies. Am J Physiol Hear Circ Physiol. 1979;236:H379–84.

29.   Heusch G. Heart rate in the pathophysiology of coronary blood flow and myocardial ischaemia: benefit from selective bradycardic agents. Br J Pharmacol. 2008 Apr;153(8):1589–601.

30.   Hsu EW, Muzikant AL, Matulevicius SA, Penland RC, Henriquez CS. Magnetic resonance myocardial fiber-orientation mapping with direct histological correlation. Am J Physiol Hear Circ Physiol. 1998 May;274(5 Pt 2):H1627–34.

31.   Nielles-Vallespin S, Mekkaoui C, Gatehouse P, Reese TG, Keegan J, Ferreira PF, et al. *In vivo* diffusion tensor MRI of the human heart: Reproducibility of breath-hold and navigator-based approaches. Magn Reson Med. 2012 Sep 21;70(2):454–65.

32.   Gamper U, Boesiger P, Kozerke S. Diffusion imaging of the *in vivo* heart using spin echoes-considerations on bulk motion sensitivity. Magn Reson Med. 2007 Feb;57(2):331–7.

33.   Welsh C, Di Bella E, Hsu E. Higher-Order Motion-Compensation for *In vivo* Cardiac Diffusion Tensor Imaging in Rats. IEEE Trans Med Imaging. 2015 Mar.

34.   Chen J, Song S-K, Liu W, McLean M, Allen JS, Tan J, et al. Remodeling of cardiac fiber structure after infarction in rats quantified with diffusion tensor MRI. Am J Physiol Heart Circ Physiol. 2003 Sep;285(3):H946–54.

35.   Abdullah OM, Drakos SG, Diakos N a., Wever-Pinzon O, Kfoury AG, Stehlik J, et al. Characterization of diffuse fibrosis in the failing human heart via diffusion tensor imaging and quantitative histological validation. NMR Biomed. 2014 Sep 9;27(11):1378–86.

36.   Scott AD, Ferreira PF a. DC, Nielles-Vallespin S, Gatehouse P, McGill L-A, Kilner P, et al. Optimal diffusion weighting for *in vivo* cardiac diffusion tensor imaging. Magn Reson Med. 2014 Aug 22.

37.   Dou J, Reese TG, Tseng W-YI, Wedeen VJ. Cardiac diffusion MRI without motion effects. Magn Reson Med. 2002 Jul;48(1):105–14.

38.   Lemke A, Laun FB, Simon D, Stieltjes B, Schad LR. An *in vivo* verification of

the intravoxel incoherent motion effect in diffusion-weighted imaging of the abdomen. Magn Reson Med. 2010 Dec;64(6):1580–5.

CHAPTER 5

DIFFUSION TENSOR IMAGING AND HISTOLOGY

OF DEVELOPING HEARTS

5.1 Abstract

Diffusion tensor imaging (DTI) has emerged as a promising method for noninvasive quantification of myocardial microstructure. However, the origin and behavior of DTI measurements during myocardial remodeling, e.g., myocyte growth, remain poorly understood. In this work, conventional and bi-compartmental DTI in addition to three-dimensional histological correlation were performed in an animal model of myocardial development from third trimester to postnatal 5 months of age. Comparing the earliest time points in the third trimester to the postnatal 5-month group, the scalar transverse diffusivities preferentially increased in both left (LV) and right (RV) ventricles: secondary eigenvalues D_2 increased by 54% (LV) and 36% (RV), whereas tertiary eigenvalue D_3 increased by 85% (LV) and 67% (RV). The longitudinal diffusivity D_1 changes were small, which led to decreased fractional anisotropy (FA) by 41% (LV) and 33% (RV) between preterm and 5-month hearts. Histological analysis confirmed that myocardial development was associated with anisotropic myocyte growth (increased width 198% and length 128%) and decreased nucleus density (70%) between preterm and postnatal 5-month hearts. In few histological samples (N=9), strong

correlations were observed between DTI diffusivities and myocyte length (Pearson r=0.89, P<0.01 with longitudinal, r=0.99, P<0.001 with transverse diffusion), myocyte width (r=0.84, P<0.01 with longitudinal, r=0.98, P<0.001 with transverse diffusion), and nucleus density (r=-0.73, P<0.05 with longitudinal, r=-0.95, P<0.001 with transverse diffusion). FA also showed strong correlations with myocyte length (r=-0.95, P<0.001), width (r=-0.96, P<0.001), and nucleus density (r=0.98, P<0.001). Results suggest that transverse diffusivity reflects remodeling of myocyte density and size as predicted from the classical model of diffusion in porous media. Further, significant rearrangements of the primary and secondary DTI eigenvectors during development were also observed. Collectively, the findings demonstrate a potential role for DTI to monitor and quantify myocardial remodeling in developing hearts and cardiac disease.

5.2 Introduction

Preterm birth complications are the world-leading cause of death among children under 5 years of age [1]. Because the fetus' lungs need the final weeks of pregnancy to fully develop, a preterm infant may endure chronic lung disease. As a result, Bronchopulmonary Dysplasia (BPD) condition develops, which is histologically characterized by alveolar simplification and structurally by persistent musclarization of resistance arterioles. This structural disruption of the pulmonary vasculature in BPD leads to development of persistent pulmonary hypertension (PH) that is refractory to treatment. One of the long-term consequences of persistent PH in former preterm children is developing heart failure. Therefore, noninvasive imaging tools to characterize myocardial structural information in the course of heart development and PH are highly desirable.

MR diffusion tensor imaging (DTI) [2] has been used to noninvasively measure

anisotropic diffusion, and thus the magnitude and spatial orientation of microstructural organization of tissues. DTI has emerged as a preferred technique for noninvasive quantifications of myocardial structures. Although feasibility of *in vivo* cardiac DTI has long been demonstrated [3]–[5], recent advances in both gradient hardware and imaging technologies have made *in vivo* cardiac DTI more widely used [6]–[9]. The principal direction of diffusion anisotropy (i.e., the DTI first eigenvector) has been directly correlated to myocardial fiber orientation [10], and used to characterize myocardial fiber structure in human [3], small [11], and large animals [12]. DTI secondary and tertiary eigenvectors have been suggested to correlate with local myocardial sheets and sheet-normal directions, respectively [13], [14]. Recently, changes in the relative distributions of the secondary eigenvector from diastole to systole associated with hypertrophic cardiomyopathy, have been observed via *in vivo* imaging [15], but the extent to which they capture the underlying myocardial sheet structural remodeling remains unclear [16], [17].

While heterogeneity of microstructure is well established in cardiac and other tissues, the origin and behavior of observed DTI changes during cardiac development remain poorly understood. Specifically, it is unclear how changes in DTI parameters correlate with specific changes in myocardial tissue components such as increased myocyte size and density. Compartmental analysis has long been used to help interpret the MRI signal in tissues, especially the brain [18]–[22], with few studies reporting it in hearts [23], [24]. In MRI, a compartment is broadly defined as a moiety of spins that share the same attributes, which can be physical location (e.g., intracellular or extracellular), macromolecular interaction (bound or free water), or other means that give

rise to their distinct properties. To make analysis of DTI signals tractable, compartmental modeling often examines the models under extremes of exchange such as the slow and fast exchange limits [25]. In the mostly widely used slow exchange limit, the aggregate MR signal is the sum of signals of the constituents weighted by their compartment sizes.

The majority of compartmental modeling of the diffusion signal has been conducted in the brain. Stanisz [26] assigned separate diffusion compartments in the nervous system of the brain arising from restricted intra-axonal diffusion, hindered extracellular space water diffusion, and an isotropic compartment arising from glial cells. The simplest two compartment model is the the ball-and-stick model where diffusion signal is thought to originate from an extracellular (isotropic ball) and intracellular (anisotropic stick) compartments [27]. Subsequent models accounted for axon diameters and diameter distribution [21], [28], at the expense of drastically increasing the scan times needed to cover wide range of b-values and diffusion times. To allow translation of these models to clinical scanners, simplifying assumptions has been proposed, for example, zero diameter approximation [29]. Although promising, most of these models lacked direct histological validation, and their validity in characterizing brain disorders is yet to be seen. Nonetheless, these compartmental models provide promising frameworks to model cardiac microstructure, provided that rigorous validation with histology is provided.

The preterm ovine model [30] offers unique opportunities to study cardiac adaptations during normal development (e.g., myocyte growth) and in disease (e.g., pulmonary hypertension) [31]. Although costly and laborious, the fetal ovine model is frequently used in investigations of cardiovascular and lung diseases because it

recapitulates human conditions with fetuses of similar size to human as well as tolerating chronic instrumentation and experimental interventions [32], [33]. Growth of the perinatal heart is mainly characterized by myocyte hyperplasia and postnatally by myocyte growth [32], [34]–[36]. Ovine fetal cardiomyocytes are small in diameter and commonly mononucleated. During the course of the third trimester, myocytes become larger and often contain two or more nuclei per cell [37]. Fetal cardiomyocytes have fewer and less organized myofibrils with poorly developed sarcoplasmic reticulum and transverse tubular system when compared to adult cardiomyocytes [38]. Therefore, the fetal ovine model offers a unique validating model for DTI analysis. In this work we sought to (a) characterize normal myocardial development in preterm ovine hearts of different gestational ages and from full term lambs using DTI, and (b) provide insights on how the observed DTI changes correlate with tissue microstructure using bi-compartmental DTI and 3D confocal microscopy.

5.3 Methods

5.3.1 Preterm Lamb Model and Specimen Collection

Fetal lambs were delivered via cesarean section. Animals were heparinized and then given 3 ml KCl intravenously moments before euthanasia, followed by a lethal injection of concentrated pentobarbital solution. Then heart was excised and placed in 250-400 mL cold phosphate buffered saline (PBS) that has 10 mEq of KCl added. The heart was perfused through the coronary arteries, then placed in 4% buffered formalin and stored at 4 °C for at least 24 hours prior to imaging.

Five groups were studied and separated based on their gestational ages: (i) D120 (N=6) delivered at 115 ± 9 d (average$\pm$SD), (ii) D130 (N=8) delivered at 132 ± 3 d, (iii)

D140 (N=6) delivered at 142 $\pm$ 2 d, (iv) D150 term-born (N=6) delivered at 150 $\pm$ 0 d, and (v) 5m (N=8) term-born but sacrificed at 5 months of age (equivalent to a 6-year-old human).

5.3.2 MRI Acquisition and Analysis

MRI experiments were performed on a Bruker 7.0 T horizontal bore MRI scanner (Bruker Biospin Inc., Ettlingen, Germany) interfaced with a 12.0 cm-diameter actively shielded gradient insert capable of producing magnetic field gradients of up to 600 mT/m. Each heart specimen was placed in a sealed container filled with susceptibility matching fluid (Fomblin, Solvay Solexis, NJ, USA). Depending on the sample size, quadrature volume coils with different inner diameters (50, 72, or 85 mm) were used for signal transmission and reception such that the signal-to-noise ratio (SNR) of the nondiffusion weighted reference image (I_0) for different heart sizes was above 80 for the same scan time.

Conventional DTI acquisition was performed using a standard multislice diffusion-weighted spin echo sequence with the following imaging parameters: 1500/30 ms TR/TE, 64 x 64 matrix size with 0.7-1.5 mm in-plane resolution, 5 short-axis slices, with 2.0 mm thickness. Diffusion was encoded along a set of 12 optimized gradient directions [39], using a pair of trapezoidal gradient pulses of 0.25 ms rise time, 5.00 ms duration (δ), and 15.00 ms separation (Δ), equivalent to a nominal b-value of 1500 s/mm^2. The total scan time for each specimen was approximately 30 min.

Postprocessing computation was performed using custom-written scripts in MATLAB (Version R2015a, Mathworks, MA) as described previously [40][2], [40]. Briefly, diffusion tensors were estimated on a voxel-by-voxel basis from the diffusion-

weighted images and diagonalized to obtain the eigenvalues (D_1, D_2 and D_3, in sorted descending order and commonly referred to as primary, secondary, and tertiary diffusivities, respectively) and their associated eigenvectors. The primary eigenvalue at each voxel reflects the diffusion coefficient longitudinal to the fibers, whereas the secondary and tertiary eigenvalues represent the diffusion coefficient transverse to fibers in the direction of the sheet and sheet-normal, respectively. The diffusion tensor eigenvalues were then used to obtain the mean diffusivity (MD) and fractional anisotropy (FA), which represent the magnitude of diffusion and degree of anisotropy. Heart images were manually segmented using Amira (Visualization Science Group, Bordeaux, France) to obtain binary masks of the right (RV) and left ventricles (LV). The scalar DTI quantities (D_1, D_2, D_3, and FA) were averaged from regions-of-interest (ROIs) covering the whole segmented tissue area in each ventricle.

DTI orientation maps were obtained from the primary ($\hat{E}_1$) and secondary ($\hat{E}_2$) eigenvectors. A local coordinate system at each voxel was defined and constructed using a distribution of potentials, described by the Laplace Dirichlet method for structural definition [41], and calculated using FEBio software suite [42]. At each imaging voxel, the radial ($\hat{a}$) (endocardium towards epicardium), longitudinal ($\hat{l}$) (apex to base), and circumferential ($\hat{c} = \hat{a} \times \hat{l}$) directions were obtained. The helix angle (HA) is defined as the angle between the projection of $\hat{E}_1$ onto the tangent plane to the epicardium wall ($\hat{l} - \hat{c}$) and the direction of $\hat{c}$, ranging from -90° (pointing toward apex) to +90° (pointing toward base). The angle between the projection of $\hat{E}_2$ onto the radial plane ($\hat{l} - \hat{a}$) and the local $\hat{a}$ direction was termed the secondary eigenvector angle (E2A), which is assumed to follow the local sheet direction [13], [43], [44]. Positive E2A angles were inclined toward

the base and negative toward the apex

Voxel-wise ventricular averages of HA measurements were obtained from manually segmented LV and RV masks. Transmural rotation of HA for the whole ventricle was obtained by fitting a linear function to the normalized transmural scatter in each slice, and the slopes from five slices were averaged for each heart. Further, the HA zones were stratified into the left-handed fibers (LHF) ($-90 \leq HA < -30$), circumferential fibers (CF) ($-30 \leq HA \leq +30$), and right handed fibers (RHF) ($+30 < HA \leq +90$), as this stratification was previously shown to characterize cardiac disease [45]–[47]. Voxel-wise E2A values were averaged over the whole ventricles and stratified to positive, negative, and absolute measurements.

5.3.3 Bi-Compartmental DTI Analysis

To elucidate the source of the observed DTI measurements, bi-compartmental DTI experiments [24], consisting of 48 gradients directions and 12 b-values ranging from 100-5000 s/mm^2 were conducted in 5 hearts randomly selected from each D130 and 5m groups, respectively. To distinguish the hearts used for bi-compartmental analysis, we will term the subgroups as D130c and 5mc where "c" refers to compartmental analysis. Other imaging parameters were similar to conventional DTI acquisitions but scan time was approximately 9 hours per heart.

The signal intensity I_j in an encoding direction j was fitted to a slow-exchange bi-exponential model consisting of two diffusion tensors, arising from fast (D_f) and slow diffusion (D_f) behaviors [24]:

$$I_j = (1 - f)\, exp\!\left(-b g_j^T \cdot D_f \cdot g_j\right) + f\, exp\!\left(-b g_j^T \cdot D_s \cdot g_j\right), \qquad (5.1)$$

where f is the volume fraction of the slow compartment, and $\boldsymbol{g}_j$ is the diffusion-encoding unit vector. Nonlinear least square fitting routine of Eq. [5.1] containing 13 unknowns (six unique tensor elements for each component plus the fraction f) was implemented in MATLAB. Cholesky parameterization of the diffusion tensor [48] was used to ensure positive-definite tensor elements. Similar procedure to conventional DTI analysis was performed to obtain the scalar principal diffusivities and FA in the LV for each fast and slow compartment. Median filtering (width of 3 pixels) was applied to the parametric maps to remove isolated noisy voxels.

5.3.4 Confocal Microscopy

Transmural biopsies with a diameter of 5 mm were taken from the LV free wall in one of each randomly selected D130, D140, and 5m hearts. Biopsies were then put into a 30% sucrose solution for >4 hours to avoid tissue damage during the subsequent freezing process. Before cryosectioning, biopsies were embedded in optimal cutting temperature (OCT) compound (Sakura Finetek Europe B.V., Alphen aan den Rijn, Netherlands). Sections parallel to the epicardial surface of 80 μm thickness were cut at -24°C using a cryotome (CM 1950, Leica AG, Wetzlar, Germany). Slices from the subepicardium, mid-wall, and subendocardium were obtained from each biopsy. After cryosectioning, OCT remnants were removed by rinsing the tissue slices three times with PBS, containing in mM: 137 NaCl, 2.7 KCl, 10 Na_2HPO_4, and 1.8 KH_2PO_4. Extracellular space constituents (including myocyte borders) were labeled using CF488A-conjugated wheat germ agglutinin (WGA, 29022, Biotium, Hayward, CA, USA) applied at a concentration of 40 $\mu g/mL$ in PBS for at least 6 hours. WGA is an established marker for glycoconjugates in the extracellular matrix that binds to cell membranes, collagen

strands, and vessel walls [49]–[51]. Additionally, nuclei were stained with 1μM 6-diamidino-2-phenylindole (DAPI, D3571, Life Technologies). All sections were mounted in Fluoromount-G (#17984-25, Electron Microscopy Science, Hatfield, PA, USA) on a glass slide and scanned using a Leica SP8 confocal microscope with a 40x oil immersion lens (numerical aperture 1.4). Two types of scans were performed in each slide, including (i) 2D tile scans with a pixel size of 0.2 μm x 0.2 μm spanning 1000 μm x 1000 μm FOV, and (ii) 3D scans with a voxel size of 0.2 μm x 0.2 μm x 0.2 μm covering a volume of approximately 205 μm x 205 μm x 50 μm. DAPI was excited with a 405nm laser, and WGA-CF488 with a 488nm laser. To minimize depth-dependent intensity attenuation, linearly increasing laser powers were used as described recently [52].

Quantitative analysis of cell size and nucleus density from DAPI and WGA volumes were performed in MATLAB. Nucleus density was calculated by a series of morphological analyses including applying (i) intensity-based threshold (mode + 2 SD) to segment the DAPI signal, (ii) median filtering with a circular kernel of 3 pixels, (iii) erosion then dilation operations to remove small pixels while maintaining the size of nuclei, and (iv) connected-component analysis to detect individual nuclei. Nucleus density (ND, units /mm^2) was obtained by dividing the number of detected nuclei by the overall tissue area.

Estimates of myocyte size (length and width) were obtained from the 3D confocal images (fused WGA and DAPI) by manually measuring the average length and width of ten randomly selected myocytes (each myocytes was measured in 3-5 different locations then averaged). Only myocytes with clear and defined borders in the 3D stacks were evaluated.

5.3.5. Statistical Analysis

Statistical analysis was performed using GraphPad Prism (Graph-Pad Prism 5.0a, GraphPad Software Inc., La Jolla, CA). Variables were reported as mean and standard error of the mean (SEM). The DTI parameters measured in the current study, including the scalar and vectorial information, were compared as a function of gestation timeframe via analysis of variance (ANOVA). In the Bonferroni-corrected post hoc tests, corrected $p<0.05$ was considered statistically significant. For bi-compartment DTI analysis, unpaired t-test was used to compare the D130c to 5mc groups, with $p<0.05$ considered statistically significant. Pearson correlation and linear regression analyses were used to quantify the association between DTI scalar parameters and myocardial microstructural measurements.

5.4 Results

5.4.1 Conventional DTI Analysis

Figures 5.1 and 5.2 show representative gross pictures of maturing lamb hearts obtained using identical fixation procedure and the averaged DTI scalar parameters, respectively. The preterm hearts increased in size only moderately, whereas the term heart looks markedly larger than the preterm hearts, likely reflecting widespread myocyte hypertrophy during the postnatal period. DTI parametric FA and MD maps show that developing hearts become less anisotropic and less restrictive to water diffusion. The appearance of HA and E2A maps is consistent with previous DTI studies [15], [53], [54].

Tables 5.1 and 5.2 summarize the group-averaged changes of the DTI scalar in the left and right ventricles. Comparing the youngest preterm group D120 to the term 5m,
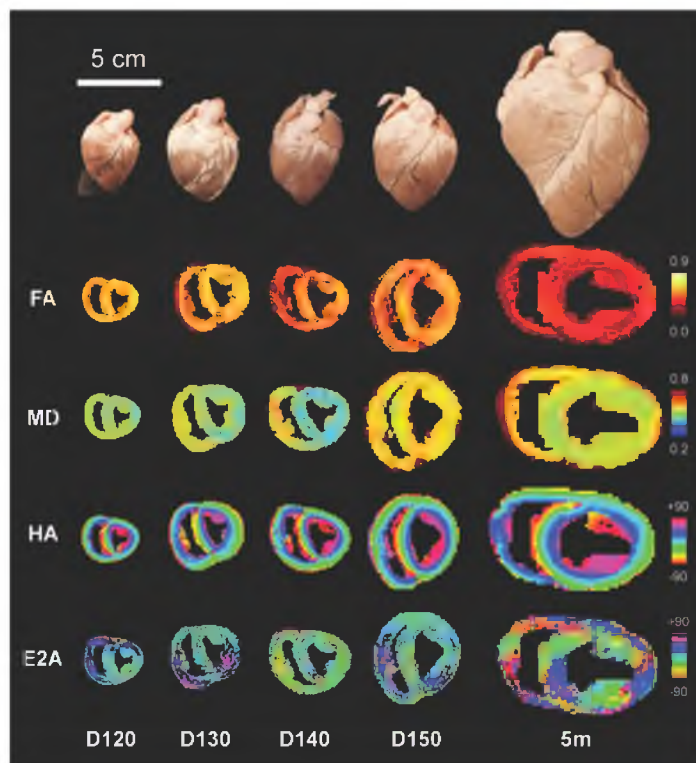
Figure 5.1. From top to lower row, representative gross pictures and DTI maps of developing lamb hearts including scalar fractional anisotropy (FA), mean diffusivity (MD), fiber helix angle (HA) and E2A (obtained from the secondary eigenvector). Preterm hearts at 120 (D120), 130 (D130), 140 days (D140) post gestation, and term 150 (D150) and 5-month (5m)-old hearts are shown. Units of MD ($x10^{-3}$ mm^2/s), and HA and E2A (degrees).
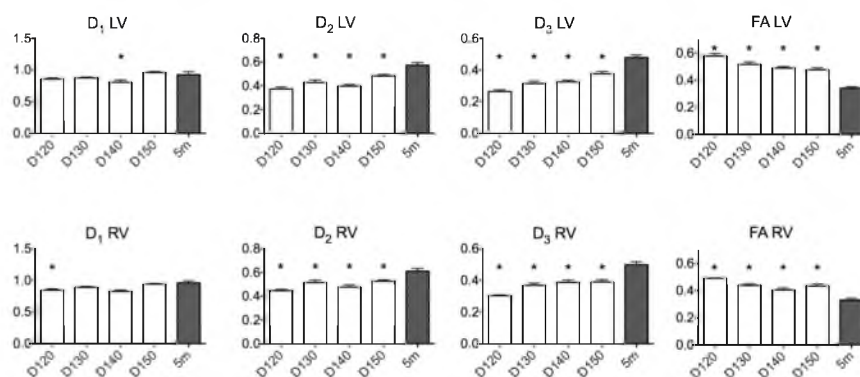
Figure 5.2. Groups averaged DTI scalar measurements (mean±SEM) taken from regions of interest in the left (LV, top row) and right ventricles (RV, bottom row). Asterisks (*) denote Bonferroni corrected P<0.05 compared to 5-months group. Primary (D_1), secondary (D_2), tertiary (D_3), and fractional anisotropy (FA) are shown. Units of diffusivities ($x10^{-3}$ mm^2/s).

Table 5.1. Left ventricular group-averaged (mean±SEM) DTI principal diffusivities (in ranked order), slope of helix angle (HA) from linear regression, mean HA, and mean E2A (absolute, positive, and negative) obtained from developing hearts at preterm ages of 120 (D120), 130 (D130), 140 (D140), full term (D150), and term at 5 months of age. Units for diffusivities ($\times 10^{-3}$ mm^2/s), whereas HA and E2A (°). Asterisks (*) denote Bonferroni corrected $P<0.05$ compared to 5-months group.

Parameter	D120 (N=6)	D130 (N=8)	D140 (N=7)	D150 (N=6)	5m (N=8)
D_1	0.86±0.02	0.87±0.01	0.80±0.04*	0.96±0.01	0.92±0.05
D_2	0.37±0.02*	0.43±0.02*	0.40±0.01*	0.48±0.01*	0.57±0.02
D_3	0.26±0.01*	0.32±0.02*	0.28±0.04*	0.38±0.01*	0.48±0.02
FA	0.58±0.02*	0.52±0.02*	0.49±0.01*	0.48±0.01*	0.34±0.01
Slope HA	104±18	119±8	117±9	119±4	113±4
Mean HA	0.4±4.9	-8.4±3.3	-3.9±1.8	-8.1±2.3	-6.7±1.2
RHF%	30±1	29±2	28±1	28±2	28±1
LHF%	18±1*	18±1*	19±1*	12±1	10±1
CF%	53±2*	53±1*	53±1*	59±2	62±1
Abs E2A	21±1*	23±2*	27±2	21±2*	30±3
Pos E2A	21±1	21±2*	26±2	21±2*	29±3
Neg E2A	-20±2*	-22±2	-27±2	-21±2*	-30±3

the scalar transverse diffusivities preferentially increased in both LV and RV: D_2 increased by 54% (LV) and 36% (RV), whereas D_3 increased by 85% (LV) and 67% (RV). The increased longitudinal diffusivity D_1 was not statistically significant for most cases, except for D140 vs. 5m in LV, D120 vs. 5m and D140 vs. 5m in RV, where the average increase was 15%. Collectively, the changes in transverse diffusivities resulted in decreased FA by 41% (LV) and 33% (RV) from D120 to 5m. The directional DTI parameters shown in Fig. 5.3 were consistent with previous cardiac DTI studies [11], [15], [45], [54], [55]. Compared to D120, HA distribution in LV of 5m significantly shifted toward circumferential orientation (17% increase) at the expense of significant reduction of LHF (by 44%) (Table 5.1), while the HA slope decreased by 28% in the RV.

Table 5.2. Right ventricular group-averaged (mean±SEM) DTI principal diffusivities (in ranked order), slope of helix angle (HA) from linear regression, mean HA, and mean E2A (absolute, positive, and negative) obtained from developing hearts at preterm ages of 120 (D120), 130 (D130), 140-days gestation (D140), full term (D150), and term at 5 months of age. Units for diffusivities ($x10^{-3}$ mm^2/s), whereas HA and E2A (°). Asterisks (*) denote Bonferroni corrected P<0.05 compared to 5-months group.

| Parameter	D120 (N=6)	D130 (N=8)	D140 (N=7)	D150 (N=6)	5m (N=8)
D_1	0.84±0.02*	0.89±0.01	0.82±0.02*	0.94±0.01	0.96±0.03
D_2	0.45±0.01*	0.52±0.02*	0.48±0.02*	0.53±0.01*	0.61±0.02
D_3	0.30±0.01*	0.37±0.01*	0.39±0.01*	0.39±0.02*	0.50±0.02
FA	0.49±0.00*	0.44±0.01*	0.40±0.01*	0.43±0.02*	0.33±0.01
Slope HA	82±6*	75±7*	76±3*	75±5*	59±9
Mean HA	3.9±2.0	6.1±2.1	7.5±3.0	3.8±2.2	11.4±2.5
RHF%	18±1	22±1	21±2	16±1	20±2
LHF%	12±3	8±1	10±1	8±2	8±2
CF%	70±3	70±1	70±2	76±2	72±4
Abs E2A	25±3*	33±2*	34±1*	30±2*	48±3
Pos E2A	25±3*	32±2*	33±2*	28±3*	46±4
Neg E2A	-21±3*	-28±3*	-35±1*	-28±3*	-49±3
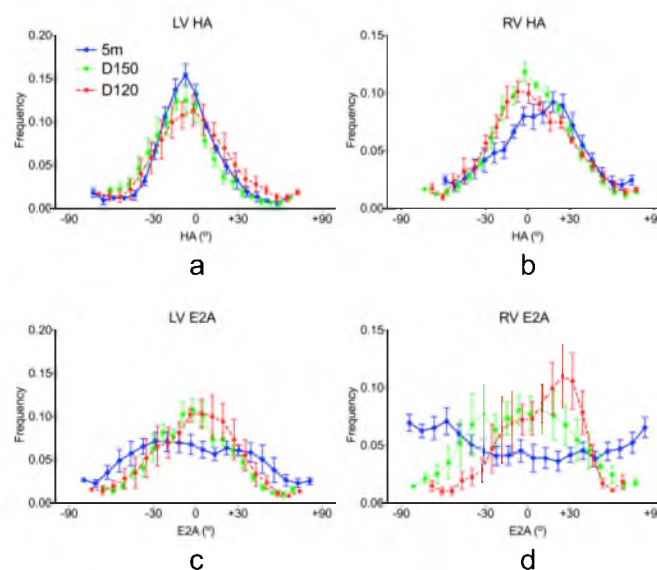
Figure 5.3. Group-averaged histograms of myocardial HA (a, b) and E2A (c, d) angles measured from 5 slices in each heart for the LV and RV, respectively. Lines and error-bars represent (mean±SEM) of the respective bin. For clarity of presentation, only the averaged histograms from 3 groups are shown for D120 (N=6), D150 (N=6), and 5m (N=8).

No significant changes in the absolute HA in both ventricles were found, although there was a trend of increasing mean HA in the RV at 5m (Fig. 5.3b and Table 5.2). The E2A histograms (Fig. 5.3c and d) symmetrically rearranged to a relatively more vertical alignment in 5m compared to F120. The absolute E2A increased by 50% and 92% during development in both the LV and RV, respectively, from D120 to 5m groups, with the changes equally driven by the negative and positive E2A components in both ventricles (Tables 5.1 and 5.2).

5.4.2 Compartmental DTI Analysis

To investigate the origin of the scalar DTI parameter changes during development, we applied compartmental DTI analysis to a preterm D130c and term 5mc hearts. Figure 5.4 shows signal decays longitudinal and transverse to myocytes (in the circumferential fibers region) encoded up to a b-value of 5000 s/mm^2 for preterm D130c and term 5mc hearts. Clearly, the signal decay from preterm and term hearts are more separated when diffusion encoding was applied transverse to myocytes (Fig. 5.4b)
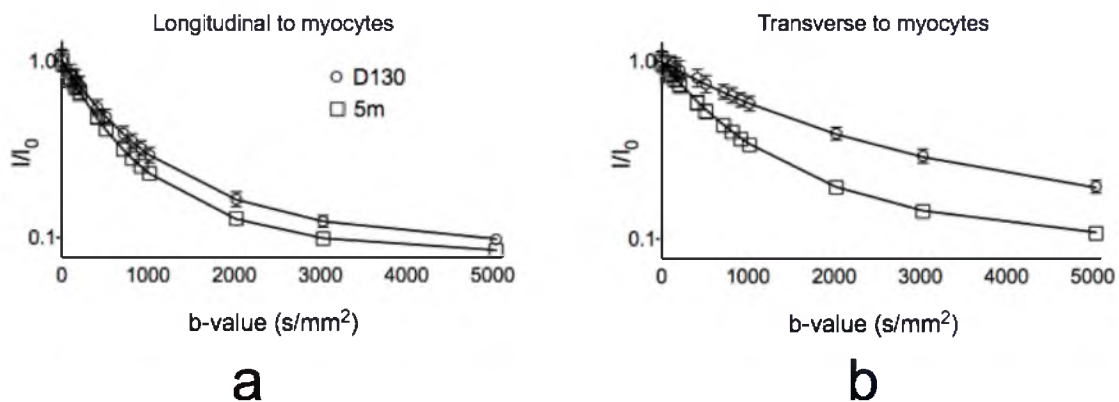

Figure 5.4. Normalized diffusion-induced signal attenuation in regions of interest taken from the circumferential fiber region of preterm 130-day (D130) and term 5-month (5m) hearts for b-value up to 5,000 s/mm^2. Bi-exponential fitting (solid line) is shown for 2 encoding directions (a) longitudinal, and (b) transverse to myocytes.

compared to the longitudinal (Fig. 5.4a) direction.

Figure 5.5 shows representative bi-compartment DTI scalar and orientation maps for both fast and slow compartments. Consistent with a previous bi-compartment cardiac DTI study [24], the slow FA map is globally higher than the fast FA, and both fast and slow FA decreased during development, which is also consistent with the conventional DTI findings (Fig. 5.1). The mean diffusivity maps also show slight increase at the 5mc compared to the preterm heart (Fig. 5.5). The helix angle maps were remarkably similar between fast and slow compartments, and show little difference between the different time points. Table 5.3 summarizes the group-averaged bi-compartmental DTI findings. As in classical DTI, there was a preferential increase in both fast and slow transverse diffusivities (D_2 and D_3), and insignificant change in the D_1 components, which resulted in decreased FA from D130c to 5mc. The volume fraction of the slow component decreased from 37% at D130c to 21% at 5mc.

5.4.3 Confocal Microscopy

Confocal microscopy images for representative heart specimens are shown in Fig. 5.6. DAPI (which stains cell nuclei) images revealed smaller nuclei and higher density in the preterm heart in Fig. 5.6a compared to the 5m group (Fig. 5.6b). Zoomed 3D confocal images (fused DAPI+WGA) in Fig. 5.6e-h clearly show increased myocyte size (black spaces) and reduced nuclei density (less blue stain) in the 5m compared to the preterm heart.

Table 5.4 summarizes the quantitative analysis from the 3 sections of each heart. Compared to preterm heart, the term 5m had decreased nuclei density (70%), whereas myocyte length and width increased by 119%, and 200%, respectively. Scatter plots

between conventional DTI analysis and confocal-based microstructural parameters are shown in Fig. 5.7. Despite the small sample size (N=9 samples), strong correlations were observed between DTI diffusivities and myocyte length (Pearson r=0.89, P<0.01 for longitudinal, r=0.99, P<0.001 for transverse diffusion), myocyte width (r=0.84, P<0.01 for longitudinal, r=0.98, P<0.001 for transverse diffusion), and nucleus density (r=-0.73, P<0.05 for longitudinal, r=-0.95, P<0.001 for transverse diffusion).

5.5 Discussion

The DTI scalar parameters revealed that maturing hearts after the third trimester become less anisotropic and less restrictive to water diffusion more clearly transverse to myofibers. DTI fiber orientation changes were detected in the left-handed and circumferential fiber fractions and helix angle slopes in the LV and RV, respectively. The secondary eigenvector-based E2A measurement was also sensitive to myocardial development in both ventricles. The scalar DTI changes were corroborated by confocal microscopy data, which showed that maturation after birth was characterized by anisotropic myocyte growth and reduced nucleus density per unit area consistent with previous reports in developing lamb hearts [32]. Despite the limited number of histological measurements, the observed strong correlations between DTI scalar parameters and myocyte size and nucleus density (Fig. 5.7) suggests that DTI is sensitive to microstructural adaptations of heart tissue, including to changes in myocyte size and density. Myocyte growth is likely to be the cause of the observed increases in D_2/D_3 (and reduction of FA).
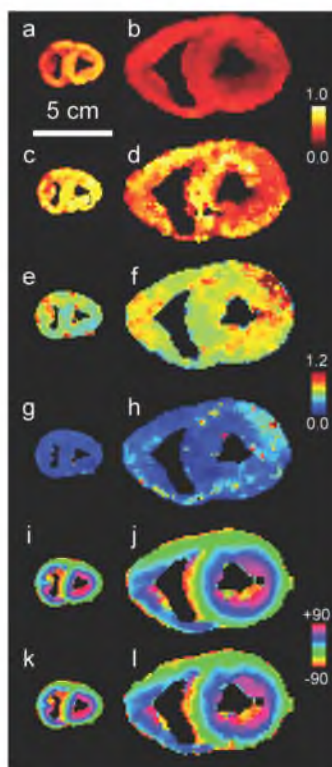
Figure 5.5. Representative maps obtained from bi-compartment DTI showing maps of fast (a, b) and slow (c, d) fractional anisotropy, fast (e, f) and slow (g, h) mean diffusivity (MD), and fast (i, j) and slow (k, l) helix angle (HA) maps from 130-days preterm and 5-month old hearts, respectively. Units of MD ($x10^{-3}$ mm^2/s), and HA (degrees).

Table 5.3. Group-averaged (mean±SEM) bi-compartment scalar DTI parameters from the left ventricles of preterm 130-days gestation (D130c) and from full term hearts at 5 months of age (5mc). The principal diffusivities in ranked order (D_1, D_2, and D_3), fractional anisotropy (FA), and the volume fraction (VF) percentages are reported for both fast and slow diffusion tensors. Asterisks (*) denote $P<0.05$; diffusivity units ($x10^{-3}$ mm^2/s).

Slow	D130c (N=5)	5mc (N=5)	Fast	D130c (N=5)	5mc (N=5)
D_1	0.38±0.03	0. 46±0.03	D_1	1.15±0.05	1.07±0.03
D_2	0.11±0.02*	0.20±0.02	D_2	0.50±0.04*	0.70±0.03
D_3	0.07±0.01*	0.12±0.02	D_3	0.35±0.03*	0.57±0.03
FA	0.72±0.02*	0.59±0.02	FA	0.57±0.03*	0.34±0.01
VF%	37±5*	21±2	VF%	63±5*	79±2
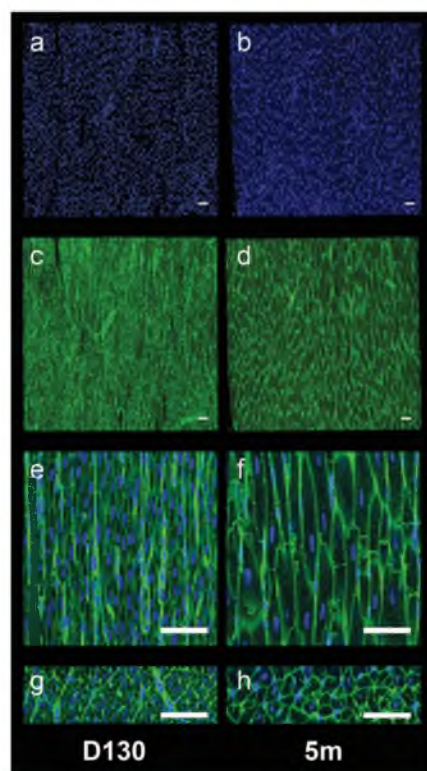
Figure 5.6. Confocal images from preterm 130-day (D130) and term 5-month (5m) hearts. Composite tile-scans for DAPI (a, b), WGA (c, d) are shown for 1 mm x 1 mm tissue area, in addition to zoomed longitudinal (e, f) and transverse (g, h) views (overlaid DAPI and WGA) taken from 3D acquisitions with an image resolution of 0.2 μm × 0.2 μm ×0.2 μm. Scale bar is 50 μm.

Table 5.4. Quantitative confocal microscopy measurements including nucleus density (ND), myocyte length, and width, obtained from randomly selected hearts at preterm 130 (D130), 140-days gestation (D140), and full term at 5-months of age (5m). In each heart, 3 transmural sections (subendocardium, mid-wall, and subepicardium) were analyzed and reported as mean±SEM.

	D130	D140	5m
	N=3 sections	N=3 sections	N=3 sections
ND (/mm^2)	6122±294	5164±403	1802±209
Myocyte Length (μm)	46±5	47±4	105±7
Myocyte Width (μm)	6±1	7±1	18±2
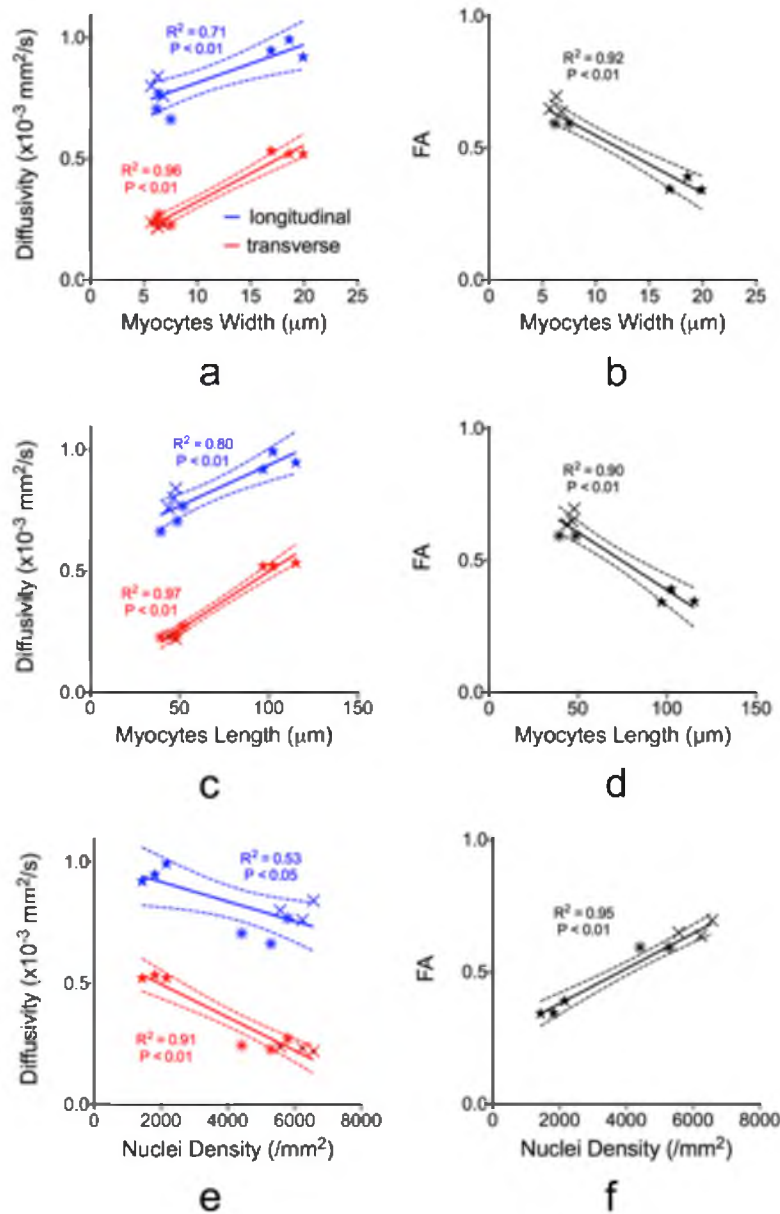
Figure 5.7. Scatter plots of DTI scalar longitudinal (D_1) and transverse diffusivities (average D_2 and D_3), and fractional anisotropy (FA) versus microstructural metrics of myocytes width (a,b), length (c,d), and nuclei density (e,f). Three transmural sections taken from the subendocardium, mid-wall, and subepicardium regions are shown for 3 different hearts with unique symbols: D136 (x), D140 (*), and 5 months (★). Linear regression (solid lines) and the 95% confidence interval (dashed lines) are shown in addition to the coefficient of determination (R^2) and its associated P value.

It has been shown that the effective transverse diffusion coefficient ($D_\perp$) in parallel cylindrical cells increases with decreased surface-to-volume ratio ($\frac{S}{V}$) and decreased tortuosity in the short and long diffusion-time limits, respectively [56]–[58]. For myocyte diameters ranging from 6 to 18 μm, and with the fixed diffusion time used in the current study $\simeq 13\ ms$, our DTI experiments were in the mid-range of the two limits. Nonetheless, a voxel containing a higher density of smaller cells as seen in the preterm heart will have higher surface-to-volume ratio and tortuosity, which in both limits will result in reduced apparent diffusion coefficient compared to a voxel with a smaller number but larger cells. This model also provides a plausible explanation why D_2/D_3 were larger in the RV compared to the LV in the prenatal ages, which is likely because myocytes in the fetal RV are larger than myocytes in the LV [32], [36].

For the sake of illustration, suppose that in the short time limit, a voxel contains packed (infinitely long) cylinders of equal radius (r) occupying a volume fraction (ϕ) and ignoring boundary relaxation, $D_\perp \propto D_0 \left[1 - c\sqrt{D_0 t}\,\frac{S}{V}\right]$, where D_0 is the intrinsic free diffusivity of the medium without restriction effects, $\frac{S}{V} = \frac{2}{r}$ for spins inside packed cylinders (or $\frac{2}{r}\frac{\phi}{1-\phi}$ for spins outside the cylinders), and c is a constant [56]–[58]. The model predicts that $D_\perp$ inside packed cylinders will increase by 55% when r increases from 6 to 18 μm (assuming longitudinal diffusivity $D_1 = D_0 = 1x10^{-3}\ mm^2/s$), which is a good first-order approximation to the observed ~30-80% increase in the experimental D_2 and D_3 for both LV and RV (Tables 5.1 and 5.2). However the packing model predicts that longitudinal diffusion parallel to the cylinder's main axis is independent of the diameters or packing density changes, which was not entirely true in this study. The small

observed changes in D_1 (~15%) between preterm and term hearts suggests that other mechanisms may play a role in the observed D_1 changes, such as imperfectly parallel myocytes, finite myocyte length, or reduced nucleus density. Bi-compartmental exchange models are often used as a tool to elucidate the observed changes in scalar DTI parameters. The analysis revealed that both slow and fast diffusivities increased in similar proportions (Table 5.3). Since the packing model described above can be extended to multicompartments [57], increased cell packing will result in reduced diffusivities in both compartments.,

The DTI orientation parameters also showed evidence of fiber realignment during heart development. Given the preserved LV HA slope during development, the observed decrease in LHF between term and preterm hearts could be related to myocyte growth. Similar reductions in the LHF have been observed in the "compensating" remote zone to infarct [45], [47], whereas the infarct zone conversely showed increased LHF [45], [59]. The realignment of the RV's HA slope could be related to pressure changes between term and preterm circulation as reported previously in RV pressure overload studies [60]. Finally, the observed realignment in E2A during development (Fig. 5.3c and d) may be related to ventricular growth, which is similar to reported differences between the diastolic state of healthy and hypertrophic hearts [15]. However, since it has been suggested that sheet structure forms after birth [61], the presence of sheets may not be the only factor affecting the organized appearance of E2A. Future studies will be conducted to directly correlate the DTI-based E2A measurements with sheet structures visualized via advanced 3D confocal microscopy staining and processing techniques [52], [62]. Previous DTI studies of developing fetal hearts that were performed in humans and

porcine [12], [63], [64] reported different trends. The human fetal studies reported progressively increasing FA and nearly no coherent fiber organization in fetal hearts taken in early points of the second trimester compared to term hearts [63], [64]. The porcine DTI study reported increasing FA in mid-gestation hearts then decreasing after birth with clearly detectable and coherent fiber organization in all preterm and term ages. In our study, the highly organized myocardial fiber orientation was detected as early as 100 days post gestation (early third trimester), albeit here we report progressively decreasing FA and increasing D_2/D_3 from the earliest time points in the 3rd trimester to the term-born and older hearts (Tables 5.1 and 5.2, and Fig. 5.1 and 5.2). Besides differences in species, DTI scan parameters and gestation age, the discrepancies can be explained by differences in specimen fixation procedures that could set the hearts at different states. DTI scalar and orientation parameters are known to depend on the cardiac state (systole vs. diastole) [43], [53], [65]. It is generally difficult, if not impossible, to controllably prepare human heart specimens in a consistent state, and the fetal preterm pig hearts in the previous study were not perfused with KCL, whereas the postnatal hearts were KCL perfused. In the study presented here, the cardiac arresting state (diastole) and the fixation procedure were identical in all hearts by using the same perfusion-fixation protocol as described in the methods.

In conclusion, our results indicate that tissue adaptation during normal development manifests in progressively increased DTI transverse diffusivities, decreased FA, distinctive fiber orientation changes in the ventricles, including changes in the secondary eigenvectors (which is presumably associated with sheets) during the third trimester and beyond. Bi-compartmental DTI analysis revealed that the changes are

mediated by similar diffusivity changes in the compartments. Additionally, our findings suggest that the behavior of the transverse diffusivities reflect myocyte density and size as predicted by a theoretical model of diffusion in porous media [56], [57]. Our results point to a potential role for DTI in detecting myocyte hypertrophy, for example in preterm hearts affected by persistent pulmonary hypertension, which is a common complication in preterm births [31], [33], [66].

5.6 References

[1]   L. Liu, S. Oza, D. Hogan, J. Perin, I. Rudan, J. E. Lawn, S. Cousens, C. Mathers, and R. E. Black, "Global, regional, and national causes of child mortality in 2000–13, with projections to inform post-2015 priorities: an updated systematic analysis," *Lancet*, vol. 385, no. 9966, pp. 430–440, Sep. 2014.

[2]   P. J. Basser, J. Mattiello, and D. LeBihan, "MR diffusion tensor spectroscopy and imaging," *Biophys. J.*, vol. 66, no. 1, pp. 259–67, Jan. 1994.

[3]   T. G. Reese, R. M. Weisskoff, R. N. Smith, B. R. Rosen, R. E. Dinsmore, and V. J. Wedeen, "Imaging myocardial fiber architecture *in vivo* with magnetic resonance," *Magn Reson Med*, vol. 34, no. 6, pp. 786–91, Dec. 1995.

[4]   W. I. Tseng, T. G. Reese, R. M. Weisskoff, and V. J. Wedeen, "Cardiac Diffusion Tensor MRI *In vivo* Without Strain Correction," *Magn. Reson. Med.*, vol. 42, pp. 393–403, 1999.

[5]   J. Dou, T. G. Reese, W.-Y. I. Tseng, and V. J. Wedeen, "Cardiac diffusion MRI without motion effects," *Magn Reson Med*, vol. 48, no. 1, pp. 105–14, Jul. 2002.

[6]   S. Nielles-Vallespin, C. Mekkaoui, P. Gatehouse, T. G. Reese, J. Keegan, P. F. Ferreira, S. Collins, P. Speier, T. Feiweier, R. de Silva, M. P. Jackowski, D. J. Pennell, D. E. Sosnovik, and D. Firmin, "*In vivo* diffusion tensor MRI of the human heart: Reproducibility of breath-hold and navigator-based approaches," *Magn Reson Med*, vol. 70, no. 2, pp. 454–465, Sep. 2012.

[7]   L.-A. McGill, T. F. Ismail, S. Nielles-Vallespin, P. Ferreira, A. D. Scott, M. Roughton, P. J. Kilner, S. Y. Ho, K. P. McCarthy, P. D. Gatehouse, R. de Silva, P. Speier, T. Feiweier, C. Mekkaoui, D. E. Sosnovik, S. K. Prasad, D. N. Firmin, and D. J. Pennell, "Reproducibility of *in vivo* diffusion tensor cardiovascular magnetic resonance in hypertrophic cardiomyopathy," *J. Cardiovasc. Magn. Reson.*, vol. 14, no. 1, p. 86, Dec. 2012.

[8]   C. T. Stoeck, A. Kalinowska, C. von Deuster, J. Harmer, R. W. Chan, M. Niemann, R. Manka, D. Atkinson, D. E. Sosnovik, C. Mekkaoui, and S. Kozerke, "Dual-phase cardiac diffusion tensor imaging with strain correction," *PLoS One*, vol. 9, no. 9, p. e107159, Jan. 2014.

[9]   C. Welsh, E. DiBella, and E. Hsu, "Higher-Order Motion-Compensation for *In vivo* Cardiac Diffusion Tensor Imaging in Rats," *IEEE Trans. Med. Imaging*, vol. 34, no. 9, pp. 1843–53, Mar. 2015.

[10]   E. W. Hsu, A. L. Muzikant, S. A. Matulevicius, R. C. Penland, and C. S. Henriquez, "Magnetic resonance myocardial fiber-orientation mapping with direct histological correlation," *Am J Physiol Hear. Circ Physiol*, vol. 274, no. 5 Pt 2, pp. H1627–34, May 1998.

[11]   Y. Jiang, K. Pandya, O. Smithies, and E. W. Hsu, "Three-dimensional diffusion tensor microscopy of fixed mouse hearts," *Magn Reson Med*, vol. 52, no. 3, pp. 453–60, Sep. 2004.

[12]   L. Zhang, J. Allen, L. Hu, S. D. Caruthers, S. a Wickline, and J. Chen, "Cardiomyocyte architectural plasticity in fetal, neonatal, and adult pig hearts delineated with diffusion tensor MRI," *Am. J. Physiol. Heart Circ. Physiol.*, vol. 304, no. 2, pp. H246–52, Jan. 2013.

[13]   W.-Y. I. Tseng, V. J. Wedeen, T. G. Reese, R. N. Smith, and E. F. Halpern, "Diffusion tensor MRI of myocardial fibers and sheets: correspondence with visible cut-face texture," *J. Magn. Reson. Imaging*, vol. 17, no. 1, pp. 31–42, Jan. 2003.

[14]   G. L. Kung, T. C. Nguyen, A. Itoh, S. Skare, N. B. Ingels, D. C. Miller, and D. B. Ennis, "The Presence of Two Local Myocardial Sheet Populations Confirmed by Diffusion Tensor MRI and Histological Validation," *J. Magn. Reson. Imaging*, vol. 34, pp. 1080–1091, 2011.

[15]   P. F. Ferreira, P. J. Kilner, L.-A. McGill, S. Nielles-Vallespin, A. D. Scott, S. Y. Ho, K. P. McCarthy, M. M. Haba, T. F. Ismail, P. D. Gatehouse, R. de Silva, A. R. Lyon, S. K. Prasad, D. N. Firmin, and D. J. Pennell, "*In vivo* cardiovascular magnetic resonance diffusion tensor imaging shows evidence of abnormal myocardial laminar orientations and mobility in hypertrophic cardiomyopathy," *J. Cardiovasc. Magn. Reson.*, vol. 16, p. 87, Jan. 2014.

[16]   L. Axel, V. J. Wedeen, and D. B. Ennis, "Probing dynamic myocardial microstructure with cardiac magnetic resonance diffusion tensor imaging," *JCMR*, pp. 1–7, 2014.

[17]   O. Bernus, A. Radjenovic, M. L. Trew, I. J. Legrice, G. B. Sands, D. R. Magee, B. H. Smaill, and S. H. Gilbert, "Comparison of diffusion tensor imaging by

cardiovascular magnetic resonance and gadolinium enhanced 3D image intensity approaches to investigation of structural anisotropy in explanted rat hearts," *JCMR*, vol. 17, no. 31, pp. 1–27, 2015.

[18] W. C. Cole, A. D. Leblanc, and S. G. Jhingran, "The origin of biexponential T2 relaxation in muscle water," *Magn. Reson. Med.*, vol. 29, no. 1, pp. 19–24, Jan. 1993.

[19] K. D. Harkins, A. N. Dula, and M. D. Does, "Effect of intercompartmental water exchange on the apparent myelin water fraction in multiexponential T2 measurements of rat spinal cord," *Magn. Reson. Med.*, vol. 67, no. 3, pp. 793–800, Mar. 2012.

[20] D. a. Yablonskiy and A. L. Sukstanskii, "Theoretical models of the diffusion weighted MR signal," *NMR Biomed.*, vol. 23, no. 7, pp. 661–681, 2010.

[21] Y. Assaf, R. Z. Freidlin, G. K. Rohde, and P. J. Basser, "New modeling and experimental framework to characterize hindered and restricted water diffusion in brain white matter," *Magn. Reson. Med.*, vol. 52, no. 5, pp. 965–78, Nov. 2004.

[22] D. C. Alexander, "A general framework for experiment design in diffusion MRI and its application in measuring direct tissue-microstructure features," *Magn Reson Med*, vol. 60, no. 2, pp. 439–48, Aug. 2008.

[23] J. R. Forder, J. D. Bui, D. L. Buckley, and S. J. Blackband, "MR imaging measurement of compartmental water diffusion in perfused heart slices," *Am J Physiol Hear. Circ Physiol.*, vol. 281, pp. H1280–H1285, 2001.

[24] E. W. Hsu, D. L. Buckley, J. D. Bui, S. J. Blackband, and J. R. Forder, "Two-component diffusion tensor MRI of isolated perfused hearts," *Magn. Reson. Med.*, vol. 45, no. 6, pp. 1039–45, Jun. 2001.

[25] T. Niendorf, R. M. Dijkhuizen, D. G. Norris, M. van Lookeren Campagne, and K. Nicolay, "Biexponential diffusion attenuation in various states of brain tissue: implications for diffusion-weighted imaging," *Magn. Reson. Med.*, vol. 36, no. 6, pp. 847–57, Dec. 1996.

[26] G. J. Stanisz, "Diffusion MR in Biological Systems: Tissue Compartments and Exchange," *Isr. J. Chem.*, vol. 43, no. 1–2, pp. 33–44, 2003.

[27] T. E. J. Behrens, M. W. Woolrich, M. Jenkinson, H. Johansen-Berg, R. G. Nunes, S. Clare, P. M. Matthews, J. M. Brady, and S. M. Smith, "Characterization and propagation of uncertainty in diffusion-weighted MR imaging," *Magn. Reson. Med.*, vol. 50, no. 5, pp. 1077–88, Nov. 2003.

[28] Y. Assaf and P. J. Basser, "Composite hindered and restricted model of diffusion (CHARMED) MR imaging of the human brain," *Neuroimage*, vol. 27, no. 1, pp.

48–58, Aug. 2005.

[29] U. Ferizi, T. Schneider, T. Witzel, L. L. Wald, H. Zhang, C. A. M. Wheeler-Kingshott, and D. C. Alexander, "White matter compartment models for *in vivo* diffusion MRI at 300mT/m," *Neuroimage*, vol. 118, pp. 468–483, 2015.

[30] K. Albertine, G. Jones, B. C. Starcher, J. F. Bohnsack, P. L. Davis, S.-C. Cho, D. P. Carlton, and R. D. Bland, "Chronic Lung Injury in Preterm Lambs," *Am. J. Respir. Crit. Care Med.*, vol. 159, no. 3, pp. 945–958, Mar. 1999.

[31] K. H. Albertine, "Utility of Large-Animal Models of BPD: Chronically Ventilated Preterm Lambs," *Am. J. Physiol. - Lung Cell. Mol. Physiol.*, vol. 308, no. 10, pp. L983–L1001, May 2015.

[32] S. S. Jonker, L. Zhang, S. Louey, G. D. Giraud, K. L. Thornburg, and J. J. Faber, "Myocyte enlargement, differentiation, and proliferation kinetics in the fetal sheep heart," *J. Appl. Physiol.*, vol. 102, no. 3, pp. 1130–42, Mar. 2007.

[33] K. H. Albertine, "Progress in understanding the pathogenesis of BPD using the baboon and sheep models," *Semin. Perinatol.*, vol. 37, no. 2, pp. 60–68, 2013.

[34] D. Sedmera and R. P. Thompson, "Myocyte proliferation in the developing heart," *Dev. Dyn.*, vol. 240, no. 6, pp. 1322–34, Jun. 2011.

[35] D. Wulfsohn, J. R. Nyengaard, and Y. Tang, "Postnatal growth of cardiomyocytes in the left ventricle of the rat," *Anat. Rec. A. Discov. Mol. Cell. Evol. Biol.*, vol. 277, no. 1, pp. 236–47, Mar. 2004.

[36] J. H. Burrell, A. M. Boyn, V. Kumarasamy, A. Hsieh, S. I. Head, and E. R. Lumbers, "Growth and maturation of cardiac myocytes in fetal sheep in the second half of gestation," *Anat. Rec. A. Discov. Mol. Cell. Evol. Biol.*, vol. 274, no. 2, pp. 952–61, Oct. 2003.

[37] A. J. Patterson and L. Zhang, "Hypoxia and fetal heart development," *Curr. Mol. Med.*, vol. 10, no. 7, pp. 653–66, Oct. 2010.

[38] J. A. Hoerter and G. Vassort, "Participation of the sarcolemma in the control of relaxation of the mammalian heart during perinatal development," *Adv. Myocardiol.*, vol. 3, pp. 373–80, Jan. 1982.

[39] N. G. Papadakis, D. Xing, C. L. Huang, L. D. Hall, and T. a Carpenter, "A comparative study of acquisition schemes for diffusion tensor imaging using MRI," *J. Magn. Reson.*, vol. 137, no. 1, pp. 67–82, Mar. 1999.

[40] O. M. Abdullah, S. G. Drakos, N. a. Diakos, O. Wever-Pinzon, A. G. Kfoury, J. Stehlik, C. H. Selzman, B. B. Reid, K. Brunisholz, D. R. Verma, C. Myrick, F. B.

Sachse, D. Y. Li, and E. W. Hsu, "Characterization of diffuse fibrosis in the failing human heart via diffusion tensor imaging and quantitative histological validation," *NMR Biomed.*, vol. 27, no. 11, pp. 1378–86, Sep. 2014.

[41]   J. D. Bayer, R. C. Blake, G. Plank, and N. a Trayanova, "A novel rule-based algorithm for assigning myocardial fiber orientation to computational heart models," *Ann. Biomed. Eng.*, vol. 40, no. 10, pp. 2243–54, Oct. 2012.

[42]   S. A. Maas, B. J. Ellis, G. A. Ateshian, and J. A. Weiss, "FEBio: finite elements for biomechanics," *J. Biomech. Eng.*, vol. 134, no. 1, p. 011005, Jan. 2012.

[43]   P. W. Hales, J. E. Schneider, R. a B. Burton, B. J. Wright, C. Bollensdorff, and P. Kohl, "Histo-anatomical structure of the living isolated rat heart in two contraction states assessed by diffusion tensor MRI," *Prog. Biophys. Mol. Biol.*, vol. 110, no. 2–3, pp. 319–30, 2012.

[44]   S. H. Gilbert, A. P. Benson, P. Li, and A. V Holden, "Regional localisation of left ventricular sheet structure: integration with current models of cardiac fibre, sheet and band structure," *Eur. J. Cardio-Thoracic Surg.*, vol. 32, no. 2, pp. 231–49, Aug. 2007.

[45]   M.-T. Wu, W.-Y. I. Tseng, M.-Y. M. Su, C.-P. Liu, K.-R. Chiou, V. J. Wedeen, T. G. Reese, and C.-F. Yang, "Diffusion tensor magnetic resonance imaging mapping the fiber architecture remodeling in human myocardium after infarction: correlation with viability and wall motion," *Circulation*, vol. 114, no. 10, pp. 1036–45, Sep. 2006.

[46]   M.-T. Wu, M.-Y. M. Su, Y.-L. Huang, K.-R. Chiou, P. Yang, H.-B. Pan, T. G. Reese, V. J. Wedeen, and W.-Y. I. Tseng, "Sequential changes of myocardial microstructure in patients postmyocardial infarction by diffusion-tensor cardiac MR: correlation with left ventricular structure and function," *Circ Cardiovasc Imaging*, vol. 2, no. 1, pp. 32–40, Jan. 2009.

[47]   C. Mekkaoui, S. Huang, H. H. Chen, G. Dai, T. G. Reese, W. J. Kostis, A. Thiagalingam, P. Maurovich-Horvat, J. N. Ruskin, U. Hoffmann, M. P. Jackowski, and D. E. Sosnovik, "Fiber architecture in remodeled myocardium revealed with a quantitative diffusion CMR tractography framework and histological validation," *J Cardiovasc Magn Reson.*, vol. 14, no. 1, p. 70, 2012.

[48]   C. G. Koay, L.-C. Chang, J. D. Carew, C. Pierpaoli, and P. J. Basser, "A unifying theoretical and algorithmic framework for least squares methods of estimation in diffusion tensor imaging," *J. Magn. Reson.*, vol. 182, no. 1, pp. 115–25, Sep. 2006.

[49]   V. P. Bhavanandan and A. W. Katlic, "The interaction of wheat germ agglutinin with sialoglycoproteins. The role of sialic acid," *J. Biol. Chem.*, vol. 254, no. 10, pp. 4000–8, May 1979.

[50] K.-O. Soederstroem, "Lectin binding to collagen strands in histologic tissue sections," *Histochem. Cell Biol*, vol. 87, no. 6, pp. 557–560, 1987.

[51] B. C. Schwab, G. Seemann, R. a Lasher, N. S. Torres, E. M. Wulfers, M. Arp, E. D. Carruth, J. H. B. Bridge, and F. B. Sachse, "Quantitative analysis of cardiac tissue including fibroblasts using three-dimensional confocal microscopy and image reconstruction: towards a basis for electrophysiological modeling," *IEEE Trans. Med. Imaging*, vol. 32, no. 5, pp. 862–72, May 2013.

[52] T. Seidel, J.-C. J.-C. Edelmann, and F. B. Sachse, "Analyzing Remodeling of Cardiac Tissue : A Comprehensive Approach Based on Confocal Microscopy and 3D Reconstructions," *Ann. Biomed. Eng.*, vol. in press, Sep. 2015.

[53] J. Chen, W. Liu, H. Zhang, L. Lacy, X. Yang, S.-K. Song, S. a Wickline, and X. Yu, "Regional ventricular wall thickening reflects changes in cardiac fiber and sheet structure during contraction: quantification with diffusion tensor MRI," *Am J Physiol Hear. Circ Physiol*, vol. 289, no. 5, pp. H1898–907, Nov. 2005.

[54] Y.-J. Cheng, D. Lang, S. D. Caruthers, I. R. Efimov, J. Chen, and S. a Wickline, "Focal but reversible diastolic sheet dysfunction reflects regional calcium mishandling in dystrophic mdx mouse hearts," *Am. J. Physiol. Heart Circ. Physiol.*, vol. 303, no. 5, pp. H559–68, Sep. 2012.

[55] L. J. Healy, Y. Jiang, and E. W. Hsu, "Quantitative comparison of myocardial fiber structure between mice, rabbit, and sheep using diffusion tensor cardiovascular magnetic resonance," *J. Cardiovasc. Magn. Reson.*, vol. 13, no. 1, p. 74, Jan. 2011.

[56] P. P. Mitra, P. N. Sen, L. M. Schwartz, and P. Le Doussal, "Diffusion propagator as a probe of the structure of porous media," *Phys. Rev. Lett.*, vol. 68, no. 24, pp. 3555–3558, 1992.

[57] L. L. Latour, K. Svoboda, P. P. Mitra, and C. H. Sotak, "Time-dependent diffusion of water in a biological model system," *Proc. Natl. Acad. Sci. U. S. A.*, vol. 91, no. 4, pp. 1229–33, Feb. 1994.

[58] E. Fieremans, Y. De Deene, S. Delputte, M. S. Ozdemir, Y. D'Asseler, J. Vlassenbroeck, K. Deblaere, E. Achten, and I. Lemahieu, "Simulation and experimental verification of the diffusion in an anisotropic fiber phantom," *J. Magn. Reson.*, vol. 190, no. 2, pp. 189–99, Feb. 2008.

[59] E. X. Wu, Y. Wu, J. M. Nicholls, J. Wang, S. Liao, S. Zhu, C.-P. Lau, and H.-F. Tse, "MR diffusion tensor imaging study of postinfarct myocardium structural remodeling in a porcine model," *Magn Reson Med*, vol. 58, no. 4, pp. 687–95, Oct. 2007.

[60] M. R. Hill, M. A. Simon, D. Valdez-Jasso, W. Zhang, H. C. Champion, and M. S. Sacks, "Structural and mechanical adaptations of right ventricle free wall myocardium to pressure overload," *Ann. Biomed. Eng.*, vol. 42, no. 12, pp. 2451–65, Dec. 2014.

[61] J. Chen, L. Zhang, H. Zhang, G. M. Lanza, and S. A. Wickline, "Postnatal Formation of Myocardial Laminar-Sheet Architecture in New Born Pig Hearts," in *Proc American Heart Association*, 2012, vol. 126, no. 21 Supplement.

[62] T. Seidel, T. Draebing, G. Seeman, and F. B. Sachse, "A Semi-automatic Approach for Segmentation of Three-Dimensional Microscopic Image Stacks," *LNCS*, vol. 7945, pp. 300–307, 2013.

[63] C. Mekkaoui, P. Porayette, M. P. Jackowski, W. J. Kostis, G. Dai, S. Sanders, and D. E. Sosnovik, "Diffusion MRI tractography of the developing human fetal heart," *PLoS One*, vol. 8, no. 8, p. e72795, Jan. 2013.

[64] E. Pervolaraki, R. A. Anderson, A. P. Benson, B. Hayes-Gill, A. V Holden, B. J. R. Moore, M. N. Paley, and H. Zhang, "Antenatal architecture and activity of the human heart," *Interface Focus*, vol. 3, no. 2, p. 20120065, Apr. 2013.

[65] M. Lohezic, I. Teh, C. Bollensdorff, R. Peyronnet, P. W. Hales, V. Grau, P. Kohl, and J. E. Schneider, "Interrogation of living myocardium in multiple static deformation states with diffusion tensor and diffusion spectrum imaging," *Prog. Biophys. Mol. Biol.*, vol. 115, 2014.

[66] K. H. Albertine, "Brain Injury in Chronically Ventilated Preterm Neonates: Collateral Damage Related to Ventilation Strategy," *Clin Perinatol*, vol. 39, no. 3, pp. 727–740, 2012.

CHAPTER 6

CONCLUDING REMARKS

6.1 Abstract

This thesis presented an approach to model and predict the origin and behavior of DTI during cardiac remodeling and physiological perturbation. Compartmental modeling is extensively used to model the brain microstructure, for example, to probe neurite size and density [1]–[4]. However, the utility of compartmental exchange models was not rigorously examined in the heart, which is very different in its architecture and physiology from the brain. The efforts presented in this thesis was focused on characterizing and modeling clinically relevant metrics on the DTI signal, including diffuse fibrosis, blood flow (aka perfusion), and myocyte size and density.

The data presented in Chapter 3 provided the first evidence for the ability of DTI to characterize diffuse fibrosis in patients with heart failure due to idiopathic cardiomyopathy, which is both a novel and timely contribution given the increased interest and effort to bring DTI to the clinical setting [5]–[9]. We further demonstrated that the effect of collagen can be modeled as an isotropic compartment being added to the "normal" tissue. Further, since DTI does not require the injection of exogenous contrast agent, DTI can be used to characterize diffuse fibrosis in patients with heart and renal failures.

The second study in Chapter 4 investigated the effect of organized capillary flow on the observed DTI signal. Since fixed tissues do not contain any moving blood, and the beating heart can complicate quantification of blood flow due to the beating motion via the so-called strain memory effects [10], here we used arrested and perfused hearts where blood flow can be tuned to physiological levels without motion complications. Indeed, we were able to document the orientation dependence of the diffusion signal with varying microvascular flow. In addition to the presented novel theory that predicted the orientation dependence of the pseudo diffusivity, we also showed that the vascular fraction is a strictly scalar quantity that only depends on the overall volume of moving blood (and not the encoding direction). An important implication of this study on current *in vivo* DTI practices is that without accounting for blood flow, conventional DTI analysis will result in overestimated principal diffusivity and also fractional anisotropy. We suggested that perfusion effects could be mitigated by either (a) employing a bicompartment model to explicitly fit the pseudo diffusivity and volume fraction at the expense of increasing scan time, (b) using higher b-values for the reference (i.e., B0) image [11], or (c) using higher order gradient moment nulling to remove the contribution of the constant velocity [12] or higher order terms [13].

The third and last study utilized a unique and clinically relevant preterm sheep model to study cardiac development using DTI. The DTI findings were further supported using high-b values characterization in selected hearts, in addition to 3D confocal microscopy as direct evidence of the underlying microstructural changes. This study found that during myocyte growth, their surface-to-volume ratio and tortuosity decrease, which causes the transverse DTI scalar diffusivities (D_2 and D_3) to increase while

virtually leaving the principal diffusivity (D1) unchanged (causing FA to decrease). Back-of-the-envelope calculations based on our confocal data suggest that existing theory that described diffusion in porous media [14], [15] provides a plausible first-order-approximation to model and predict the effects of increased myocyte diameter and density on the DTI signal.

Collectively, the presented studies provided strong evidence for the utility of cardiac DTI in providing important and clinically-relevant information to characterize (a) diffuse fibrosis, (b) capillary blood flow speeds and orientations, and (d) myocyte size and density.

6.2 Future Directions

Preterm birth complications are the world-leading cause of death among children under 5 years of age [16]. Preterm birth is also a leading cause of long-term persistent pulmonary hypertension and/or neurological disabilities in survivors of preterm birth. Some organ systems, including the brain, lungs, and liver need the final weeks of pregnancy to fully develop. Therefore, many infants show signs of respiratory distress due to lung immaturity, which often necessitates the use of invasive mechanical ventilation (IMV) with oxygen-rich gas for survival. Prolonged IMV can result in bronchopulmonary dysplasia (BPD) [17].

The original description of BPD was of a more extreme lung disease that reflected the extreme measures to keep preterm infants alive in the presurfactant era [17]. Advances in treatment options, such as antenatal steroids, postnatal surfactant, and gentler ventilator strategies, improved survival of infants born at extremely low gestational age [18]. Prolonged IMV of preterm infants today leads to "new" BPD, which

is manifest as arrest of alveolar formation and pulmonary vascular growth, which are called alveolar simplification [19].

Normal alveolar formation entails thinning of the lung's parenchyma and increasing surface area of alveoli and the underlying capillaries. However, in mechanically ventilated preterm infants, pulmonary vascular growth and maturation are disrupted structurally and functionally. Structurally, the resistance arterioles have persistent muscularization and reduced growth of alveolar capillaries such that pulmonary vascular surface area is reduced. Functionally, these vessels also have reduced nitric oxide signaling pathway and become tachyphylactic to exogenously inhaled nitric oxide. These structural and functional changes are associated with development of pulmonary hypertension. Later in life, right ventricular hypertrophy occurs, leading to persistent pulmonary hypertension [20].

The pathogenesis of persistent pulmonary hypertension is not known. No treatment is available, save for heart transplantation. Furthermore, standardized criteria are lacking for determining which preterm infants are at risk for developing pulmonary hypertension. It is well established that restricted flow through the pulmonary arterial circulation results in increased pulmonary vascular resistance, which forces the right side of the heart to adapt (e.g., via myocyte hypertrophy) and ultimately to failure. The transition from "compensated" or adaptive myocardial hypertrophy to decompensated hypertrophic heart failure is the topic of intense focus in recent years [21], [22]. Hypertrophic heart failure (HF) has been associated with deleterious microstructural alterations such as myocytes hypertrophy, development of diffuse fibrosis [23], [24], and microvascular changes including reduced capillary density and coronary flow reserve

[25], [26]. However, microstructural remodeling in the myocardium is not always accompanied by the same microvascular response, or vice versa. For example, while adaptive hypertrophy associated with normal growth is accompanied by expansion of the microvasculature [27], signaling pathways have been identified and their down-regulation was implicated in impaired angiogenesis that led to decompensated hypertrophy [21], [22], [27], [28], highlighting the role of microcirculation in the transition from adaptive hypertrophy to heart failure. Collectively, these findings suggest that myocardial microstructure and microcirculation offer complementary and more complete information on the heart's state of health, and underscore the need for a tool that can be used to assess them noninvasively (i.e., in live patients).

One of the challenges to uncovering the pathogenic mechanisms that lead to PH and associated heart failure is having large-animal, physiological models that replicate BPD in preterm infants. Only two models were developed, one in the 1980s and the other in the 1990s, with only one model continuing to this day. The two models are the preterm baboon model, developed by Dr. Coalson and colleagues [29], and the preterm lamb model of Dr. Albertine and coworkers [30]–[34]. The preterm baboon program closed more than a decade ago, leaving Dr. Albertine's model as the only large-animal, physiological tool to test hypotheses about the pathogenesis of BPD and its lifelong consequences in the heart and other organs.

Preterm lambs develop pulmonary hypertension over weeks of continuous IMV support. Former preterm lambs have structural and functional manifestations of persistent PH and right ventricular hypertrophy. Moreover, the preterm lamb models in Albertine's lab are physiological, meaning that continuous and/or repeated measures are routinely

made of pulmonary and systemic blood pressure, cardiac imaging, pulmonary function testing, and terminally, the heart is evaluated structurally, biochemically, and molecularly. Preterm lambs receive respiratory support for 3d, 6d, or 21d, and former preterm lambs (supported for 3d or 6d) live for 2 and 5 months corrected postnatal age (equivalent to 1-2 and ~6 years corrected postnatal age, respectively, in humans). My long-term plan is to test my innovative cardiac imaging approaches with Dr. Albertine's lamb models to identify and quantify cardiac manifestations of preterm birth and respiratory support, and to test treatment regimens that are intended to reduce persistent pulmonary hypertension later in life

The presented studies in this thesis set the stage for future grant proposals aiming to characterize both myocardial microstructure and microcirculation in PH in a heart that is transitioning from compensated hypertrophy to decompensated failure. Equation [4.14] highlights the potential role of compartmental exchange diffusion MRI to characterize both cardiac microstructure (via $\mathbf{D}_{tissue}$) as well as microcirculation speed (via $\mathbf{D}_{app}^*$) and capillary volume fraction (f). In principal, compensated hypertrophy is expected to result in simultaneous increases in both the transverse scalar diffusivities of $\mathbf{D}_{tissue}$, vascular volume fraction (f), and possibly the principal component of $\mathbf{D}_{app}^*$ as a result of higher capillary fraction in each imaging voxel. On the other hand, decompensated HF is expected to only result in increases in scalar quantities of $\mathbf{D}_{tissue}$ with a concomitant decrease in both vascular volume fraction and scalar components of $\mathbf{D}_{app}^*$ (especially the principal eigenvector). If proven true, compartmental DTI will be the only available noninvasive single imaging tool to date that can differentiate compensated from decompensated hypertrophy. Therefore, future effort should focus on performing further

validations of bi-compartment DTI against direct structural measurements such as advanced 3D confocal microscopy [35], and ultimately translating the proposed techniques to the live beating heart. Specifically, the immediate goals for the next round of grant proposal(s) should achieve the following Aims:

Aim 1: To quantify architecture of former preterm lamb hearts that were mechanically ventilated at birth using histology and 3-dimensional confocal microscopy, and directly link the observations to compartmental DTI simulations with experimental validation. Three-dimensional reconstruction of cardiomyocytes, extracellular space volume, collagen, capillaries, and fibroblast will be obtained with appropriate staining and advanced processing techniques [27], [35] in selected regions from the right and left ventricles of each heart. Then compartmental DTI signal simulations will be performed to determine optimal acquisition strategies to capture the key structures affected by PH (e.g., myocyte size, capillary fraction) and appropriately determine the imaging parameters (gradient directions, gradient magnitudes, and diffusion times) in future DTI acquisitions.

Aim 2: To develop highly acquisition-time-efficient means of compartmental diffusion tensor MRI. Diffusion tensor-based compartmental analysis will require a high number of scans that vary in both the magnitude and direction of diffusion encoding. To make such experiments practically feasible, sparse sampling of the multidimensional data in conjunction with constrained-reconstruction can be applied to the compartmental signal model, and test the validity of the approach on perfused, arrested isolated sheep hearts.

Aim 3: To develop and apply compartmental diffusion tensor imaging to *in vivo*

MRI of normal sheep hearts. Cardiac diffusion MRI on live animals faces additional challenges arising from bulk motion of the beating heart even in gated acquisitions. But combing sparse sampling and compartmental DTI model-based reconstruction techniques with diffusion MRI can be made sensitive to both tissue microstructure and microcirculation, but not bulk motion. The combined methodology can be used to image former preterm lamb hearts in a clinical scanner across the cardiac cycle to study the dependence of MRI measurements of microstructure and microcirculation on normal physiology.

Aim 4: To characterize microstructural and microcirculation remodeling in mechanically ventilated former preterm hearts suffering from pulmonary hypertension. The practical applicability of the proposed Aims above will be demonstrated for studying the effects of pulmonary hypertension in the former preterm and age-matched term-born lamb hearts by longitudinally characterizing changes in myocardial microstructure and microcirculation.

6.3 References

[1]   Y. Assaf, R. Z. Freidlin, G. K. Rohde, and P. J. Basser, "New modeling and experimental framework to characterize hindered and restricted water diffusion in brain white matter," *Magn. Reson. Med.*, vol. 52, no. 5, pp. 965–78, Nov. 2004.

[2]   Y. Assaf and P. J. Basser, "Composite hindered and restricted model of diffusion (CHARMED) MR imaging of the human brain," *Neuroimage*, vol. 27, no. 1, pp. 48–58, Aug. 2005.

[3]   D. C. Alexander, "A general framework for experiment design in diffusion MRI and its application in measuring direct tissue-microstructure features," *Magn Reson Med*, vol. 60, no. 2, pp. 439–48, Aug. 2008.

[4]   P. N. Sen and P. J. Basser, "A model for diffusion in white matter in the brain," *Biophys. J.*, vol. 89, no. 5, pp. 2927–38, Nov. 2005.

[5]   S. Nielles-Vallespin, C. Mekkaoui, P. Gatehouse, T. G. Reese, J. Keegan, P. F. Ferreira, S. Collins, P. Speier, T. Feiweier, R. de Silva, M. P. Jackowski, D. J. Pennell, D. E. Sosnovik, and D. Firmin, "*In vivo* diffusion tensor MRI of the human heart: Reproducibility of breath-hold and navigator-based approaches," *Magn Reson Med*, vol. 70, no. 2, pp. 454–465, Sep. 2012.

[6]   G. J. Strijkers, A. Bouts, W. M. Blankesteijn, T. H. J. M. Peeters, A. Vilanova, M. C. van Prooijen, H. M. H. F. Sanders, E. Heijman, and K. Nicolay, "Diffusion tensor imaging of left ventricular remodeling in response to myocardial infarction in the mouse," *NMR Biomed.*, vol. 22, no. 2, pp. 182–90, Feb. 2009.

[7]   Y. Wu and E. X. Wu, "MR investigation of the coupling between myocardial fiber architecture and cardiac contraction," *Conf Proc. IEEE Eng. Med. Biol. Soc.*, vol. 2009, pp. 4395–8, Jan. 2009.

[8]   C. T. Stoeck, A. Kalinowska, C. von Deuster, J. Harmer, R. W. Chan, M. Niemann, R. Manka, D. Atkinson, D. E. Sosnovik, C. Mekkaoui, and S. Kozerke, "Dual-phase cardiac diffusion tensor imaging with strain correction," *PLoS One*, vol. 9, no. 9, p. e107159, Jan. 2014.

[9]   D. E. Sosnovik, C. Mekkaoui, S. Huang, H. H. Chen, G. Dai, C. T. Stoeck, S. Ngoy, J. Guan, R. Wang, W. J. Kostis, M. P. Jackowski, V. J. Wedeen, S. Kozerke, and R. Liao, "Microstructural Impact of Ischemia and Bone Marrow-Derived Cell Therapy Revealed with Diffusion Tensor MRI Tractography of the Heart *In vivo*," *Circulation*, vol. 129, no. 17, pp. 1731–1741, Mar. 2014.

[10]   T. Reese, V. Wedeen, and R. Weisskoff, "Measuring Diffusion in the Presence of Material Strain," *J. Magn. Reson.*, vol. 112, no. 3, pp. 253–8, Sep. 1996.

[11]   O. Abdullah, A. D. Gomez, S. Merchant, O. Stedham, M. Heidinger, S. Poelzing, and E. Hsu, "Effects of Perfusion on Cardiac MR Diffusion Measurements," in *Proceedings of the 21st Annual Meeting of ISMRM*, 2012, vol. 34, no. 2.

[12]   U. Gamper, P. Boesiger, and S. Kozerke, "Diffusion imaging of the *in vivo* heart using spin echoes-considerations on bulk motion sensitivity," *Magn Reson Med*, vol. 57, no. 2, pp. 331–7, Feb. 2007.

[13]   C. Welsh, E. DiBella, and E. Hsu, "Higher-Order Motion-Compensation for *In vivo* Cardiac Diffusion Tensor Imaging in Rats," *IEEE Trans. Med. Imaging*, vol. 34, no. 9, pp. 1843–53, Mar. 2015.

[14]   P. P. Mitra, P. N. Sen, L. M. Schwartz, and P. Le Doussal, "Diffusion propagator as a probe of the structure of porous media," *Phys. Rev. Lett.*, vol. 68, no. 24, pp. 3555–3558, 1992.

[15]   L. L. Latour, K. Svoboda, P. P. Mitra, and C. H. Sotak, "Time-dependent diffusion

of water in a biological model system," *Proc. Natl. Acad. Sci. U. S. A.*, vol. 91, no. 4, pp. 1229–33, Feb. 1994.

[16] L. Liu, S. Oza, D. Hogan, J. Perin, I. Rudan, J. E. Lawn, S. Cousens, C. Mathers, and R. E. Black, "Global, regional, and national causes of child mortality in 2000–13, with projections to inform post-2015 priorities: an updated systematic analysis," *Lancet*, vol. 385, no. 9966, pp. 430–440, Sep. 2014.

[17] W. H. Northway, R. C. Rosan, and D. Y. Porter, "Pulmonary disease following respirator therapy of hyaline-membrane disease. Bronchopulmonary dysplasia," *N. Engl. J. Med.*, vol. 276, no. 7, pp. 357–68, Feb. 1967.

[18] C. D. Baker, S. H. Abman, and P. M. Mourani, "Pulmonary Hypertension in Preterm Infants with Bronchopulmonary Dysplasia," *Pediatr. Allergy. Immunol. Pulmonol.*, vol. 27, no. 1, pp. 8–16, Mar. 2014.

[19] A. J. Jobe, "The New BPD: An Arrest of Lung Development," *Pediatr. Res.*, vol. 46, no. 6, pp. 641–641, Dec. 1999.

[20] R. Bhat, A. A. Salas, C. Foster, W. A. Carlo, and N. Ambalavanan, "Prospective analysis of pulmonary hypertension in extremely low birth weight infants," *Pediatrics*, vol. 129, no. 3, pp. e682–9, Mar. 2012.

[21] R. Humar, L. Zimmerli, and E. Battegay, "Angiogenesis and hypertension: an update," *J. Hum. Hypertens.*, vol. 23, no. 12, pp. 773–782, 2009.

[22] T. Oka, H. Akazawa, A. T. Naito, and I. Komuro, "Angiogenesis and cardiac hypertrophy: maintenance of cardiac function and causative roles in heart failure," *Circ. Res.*, vol. 114, no. 3, pp. 565–71, Jan. 2014.

[23] D. L. Mann and M. R. Bristow, "Mechanisms and models in heart failure: the biomechanical model and beyond," *Circulation*, vol. 111, no. 21, pp. 2837–49, May 2005.

[24] S. G. Drakos, A. G. Kfoury, J. Stehlik, C. H. Selzman, B. B. Reid, J. V Terrovitis, J. N. Nanas, and D. Y. Li, "Bridge to recovery: understanding the disconnect between clinical and biological outcomes," *Circulation*, vol. 126, no. 2, pp. 230–41, Jul. 2012.

[25] E. P. Tsagalou, M. Anastasiou-Nana, E. Agapitos, A. Gika, S. G. Drakos, J. V Terrovitis, A. Ntalianis, and J. N. Nanas, "Depressed coronary flow reserve is associated with decreased myocardial capillary density in patients with heart failure due to idiopathic dilated cardiomyopathy," *J. Am. Coll. Cardiol.*, vol. 52, no. 17, pp. 1391–8, Oct. 2008.

[26] S. F. Mohammed, S. Hussain, S. a. Mirzoyev, W. D. Edwards, J. J. Maleszewski,

and M. M. Redfield, "Coronary Microvascular Rarefaction and Myocardial Fibrosis in Heart Failure With Preserved Ejection Fraction," *Circulation*, vol. 131, no. 6, pp. 550–559, 2015.

[27]   I. Shiojima, K. Sato, and W. Kenneth, "Disruption of Coordinated Tissue Growth and Angiogenesis in the Heart Contributes to the Progression from Adaptive Hypertrophy to Heart Failure," *J. Card. Fail.*, vol. 11, no. 9, p. S278, 2005.

[28]   B. I. Levy, G. Ambrosio, a R. Pries, and H. a Struijker-Boudier, "Microcirculation in hypertension: a new target for treatment?," *Circulation*, vol. 104, no. 6, pp. 735–740, 2001.

[29]   J. J. Coalson, T. J. Kuehl, M. B. Escobedo, J. L. Hilliard, F. Smith, K. Meredith, D. M. Null, W. Walsh, D. Johnson, and J. L. Robotham, "A baboon model of bronchopulmonary dysplasia. II. Pathologic features," *Exp. Mol. Pathol.*, vol. 37, no. 3, pp. 335–50, Dec. 1982.

[30]   K. Albertine, G. Jones, B. C. Starcher, J. F. Bohnsack, P. L. Davis, S.-C. Cho, D. P. Carlton, and R. D. Bland, "Chronic Lung Injury in Preterm Lambs," *Am. J. Respir. Crit. Care Med.*, vol. 159, no. 3, pp. 945–958, Mar. 1999.

[31]   V. K. Rehan, J. Fong, R. Lee, R. Sakurai, Z.-M. Wang, M. J. Dahl, R. H. Lane, K. H. Albertine, and J. S. Torday, "Mechanism of reduced lung injury by high-frequency nasal ventilation in a preterm lamb model of neonatal chronic lung disease," *Pediatr. Res.*, vol. 70, no. 5, pp. 462–6, Dec. 2011.

[32]   K. H. Albertine, "Brain Injury in Chronically Ventilated Preterm Neonates: Collateral Damage Related to Ventilation Strategy," *Clin Perinatol*, vol. 39, no. 3, pp. 727–740, 2012.

[33]   K. H. Albertine, "Progress in understanding the pathogenesis of BPD using the baboon and sheep models," *Semin. Perinatol.*, vol. 37, no. 2, pp. 60–68, 2013.

[34]   K. H. Albertine, "Utility of Large-Animal Models of BPD: Chronically Ventilated Preterm Lambs," *Am. J. Physiol. - Lung Cell. Mol. Physiol.*, vol. 308, no. 10, pp. L983–L1001, May 2015.

[35]   T. Seidel, J.-C. J.-C. Edelmann, and F. B. Sachse, "Analyzing Remodeling of Cardiac Tissue : A Comprehensive Approach Based on Confocal Microscopy and 3D Reconstructions," *Ann. Biomed. Eng.*, vol. in press, Sep. 2015.